DEPARTMENT OF PHYSICS
UNIVERSITY OF JYVÄSKYLÄ
RESEARCH REPORT No. 13/2016

OPTICAL PROPERTIES OF CONDUCTIVE CARBON-BASED NANOMATERIALS

BY
TOMMI ISONIEMI

Academic Dissertation
for the Degree of
Doctor of Philosophy

To be presented, by permission of the
Faculty of Mathematics and Science
of the University of Jyväskylä,
for public examination in Auditorium FYS1 of the
University of Jyväskylä on December 7, 2016
at 12 o'clock noon

Jyväskylä, Finland
December 2016

Preface

The work reviewed in this thesis has been carried out during the years 2010-2016 at the Department of Physics at the University of Jyväskylä.

First of all I would like to thank my supervisor, Dr. Jussi Toppari, for all the help and guidance he has given during my time in the group. I wish to also thank my co-supervisor, Dr. Andreas Johansson, for support and advice especially concerning carbon nanotubes and graphene, and Prof. Henrik Kunttu for part of the funding as well as for help particularly in the field of scanning near-field optical microscopy.

I am grateful for Dr. Marcus Rinkiö, Dr. Tommi Hakala and Prof. Päivi Törmä for their guidance during my MSc studies and at the beginning of this thesis work. Dr. Sampo Tuukkanen, Dr. David C. Cameron and Dr. Janne Simonen have also directly contributed to the work. I extend my gratitude to all the past and present members of the Molecular Electronics and Plasmonics group, to co-workers at the Nanoscience Center, to office staff at the Physics Department, to laboratory engineers for their assistance in technical issues and to my family for support.

Financial support from the National Doctoral Programme in Nanoscience, Academy of Finland and the Vilho, Yrjö and Kalle Väisälä Foundation are gratefully acknowledged.

Jyväskylä, October 2016

Tommi Isoniemi

Abstract

Isoniemi, Tommi
Optical properties of conductive carbon-based nanomaterials
Jyväskylä: University of Jyväskylä, 2016, 102 p.
(Research report/Department of Physics, University of Jyväskylä,
ISSN 0075-465X; 13/2016)
ISBN 978-951-39-6805-2 (paper copy)
ISBN 978-951-39-6806-9 (PDF)
diss.

The interaction of light with carbon nanomaterials is the main focus of this thesis. I explore several nanostructured systems involving different allotropes of carbon, and characterize them both electrically, if applicable, and optically. Special attention is paid to search for plasmon-like excitations on the systems, or utilizing surface plasmons on characterization.

The first objective is to achieve control of carbon nanotube (CNT) conductivity with surface plasmon polaritons (SPPs), which resulted in the first CNT field-effect transistor (FET) that can be gated definitively with SPPs. The second objective is the investigation of optical properties of various thin carbon-based molecular networks. Recently developed methods allow separation of different types of CNTs. Inspired by that, films consisting of only metallic-type single-walled (SW)CNTs were studied, which led to the discovery of a dispersive collective optical resonance in these thin films. With similar methods, conductive polymer films were also measured.

To pursue the first goal, a FET was fabricated using a semiconducting-type SWCNT and a thin silver film as a backgate, on which SPPs were excited close to the CNT via the Kretschmann total internal reflection (TIR) configuration. As a result, the CNT FET could be gated at a low optical excitation power using SPPs, which most likely trigger desorption on the device, alter the Schottky barriers on CNT contacts and modulate the current. A scanning near-field optical microscope was also used to measure the local photosensitivity of the CNT FETs.

Thin films of chirality-selected SWCNTs were measured with optical spectroscopy in TIR conditions, and a new collective excitation was discovered in metallic-type SWCNTs. This dispersive phenomenon appeared only with a polarization not able to excite regular SPPs, and was linked to the excitonic transitions of the tubes. It shared features with SPPs such as the dependence on both the film thickness

and the properties of the surrounding medium. Transparent conductive polymer films, some with graphene flakes, were also characterized, and their optical properties evaluated with TIR spectroscopy. No plasmonic or other peculiar resonances were detected, but the study led to a method to evaluate the optical anisotropy in thin polymer films. Using this method, it was possible to measure thick and uneven films, that are unsuitable for ellipsometry.

Keywords carbon nanotubes, optoelectronics, spectroscopy, plasmonics, conductive polymers, graphene

Author's address Tommi Isoniemi
Department of Physics
University of Jyväskylä
Finland

Supervisor Docent Jussi Toppari
Department of Physics
University of Jyväskylä
Finland

Co-supervisor Dr. Andreas Johansson
Department of Physics
University of Jyväskylä
Finland

Reviewers Professor Albert Nasibulin
Center for Photonics and Quantum Materials
Skolkovo Institute of Science and Technology
Russia

Associate Professor Tapio Niemi
Optoelectronics Research Centre
Tampere University of Technology
Finland

Opponent Professor Yuri Svirko
Institute of Photonics
University of Eastern Finland
Finland

Tiivistelmä (Abstract in Finnish)

Grafiittisen hiilen muodostamien nanorakenteiden, hiilinanoputkien ja grafeenin, vuorovaikutus valon kanssa on tämän väitöskirjan pääaihe. Grafeeni on yksittäinen hiilen muodostama atomikerros grafiitista, ja tällainen kerros itseensä kiertyneenä muodostaa hiilinanoputken, joka voi olla sähköisiltä ominaisuuksiltaan metallinen tai puolijohtava kiertymissuunnasta riippuen. Valo ei voi kulkea metalleissa, mutta metallin johtavuuselektronien liike voi kytkeytyä valon kanssa tietyissä tilanteissa, jolloin muodostuu metallin pinnalla kulkeva viritystila, pintaplasmonipolaritoni.

Tutkimuksen ensimmäisenä tavoitteena oli hallita hiilinanoputkien johtavuutta näillä plasmoneilla. Tätä varten valmistettiin ensimmäinen varsinainen pintaplasmonipolaritonihiilinanoputkikanavatransistori. Kanavatransistoriin käytettiin ohutta hopeakalvoa, jonka pinnalla plasmonit pystyivät kulkemaan ja jota käytettiin transistorin hilaelektrodina. Plasmonit muodostettiin prisman avulla kokonaisheijastusmenetelmällä. Kanavana oli puolijohtava yksiseinäinen hiilinanoputki kytkettynä palladiumelektrodeihin. Hiilinanoputkitransistorin virtaa pystyttiin ensi kertaa säätelemään plasmonien avulla käyttäen hyväksi transistorin pinnalla tapahtuvaa kemiallista vuorovaikutusta. Vastaavien transistorien valoherkkyyttä tutkittiin myös optisella lähikenttämikroskoopilla.

Toisena painoalueena oli tutkia sähköä johtavien hiilen muodostamien nanorakenteiden optisia ominaisuuksia. Kiraalisuuden mukaan valittujen hiilinanoputkien muodostamia kalvoja mitattiin optisella spektroskopialla, ja metallistyyppisistä hiilinanoputkikalvoista löydettiin kokonaisheijastusoloissa aiemmin tuntematon kulmariippuva optinen resonanssi. Tämä viritystila ei ole tyypillinen metallissa esiintyvä plasmonipolaritoni, koska sen virityspolarisaatio on vastakkainen. Resonanssi on kuitenkin riippuvainen kalvon paksuudesta sekä kalvon päällä olevasta materiaalista, mitkä viittaavat pinnalla tapahtuvaan kollektiiviseen viritykseen.

Vastaavaa menetelmää käytettiin ohuiden polymeerikalvojen optisen anisotrooppisuuden arvioimiseen. Tutkittavana (optisten ja sähköisten ominaisuuksien sekä rakenteen suhteen) oli johtavia, läpinäkyviä polymeerejä (PEDOT:PSS), joista osassa oli johtavuuden parantamiseksi lisättyjä grafeenilastuja. Kokonaisheijastusmenetelmällä voitiin mitata paksuja ja epätasaisia kalvoja, joista on vaikea saada tietoja perinteisellä ellipsometrialla.

List of Publications

The main results of this thesis have been reported in the following articles:

A.I ISONIEMI, T., JOHANSSON, A., HAKALA, T.K., RINKIÖ, M., TÖRMÄ, P., TOPPARI, J.J. AND KUNTTU, H., *Surface plasmon effects in carbon nanotube field effect transistors*. Applied Physics Letters **99** (2011) 031105.

A.II ISONIEMI, T., JOHANSSON, A., TOPPARI, J.J. AND KUNTTU, H., *Collective optical resonances in networks of metallic carbon nanotubes*. Carbon **63** (2013) 581–585.

A.III ISONIEMI, T., TUUKKANEN, S.T., CAMERON, D.C., SIMONEN, J. AND TOPPARI, J.J., *Measuring optical anisotropy in poly(3,4-ethylene dioxythiophene):poly(styrene sulfonate) films with added graphene*. Organic Electronics **25** (2015) 317–323.

Author's contribution

In article A.I the author wrote the publication, fabricated all of the samples, did almost all of the measurements and carried out most of the data analysis.

In A.II the author's contribution consisted of writing the paper, most of the data analysis and all of the experimental work except Raman measurements.

For A.III the author carried out half of sample fabrication, most of the measurements, most of the data analysis and was the main contributor in writing the publication.

Other work to which the author has contributed:

B.I HYNNINEN, V., VUORI, L., HANNULA, M., TAPIO, K., LAHTONEN, K., ISONIEMI, T., LEHTONEN, E., HIRSIMÄKI, M., TOPPARI, J.J., VALDEN, M. AND HYTÖNEN, V.P., *Improved antifouling properties and selective biofunctionalization of stainless steel by employing heterobifunctional silane-polyethylene glycol overlayers and avidin-biotin technology*. Scientific Reports **6** (2016) 29324.

List of Abbreviations

AFM	atomic force microscope
ALD	atomic layer deposition
CNT	carbon nanotube
CVD	chemical vapor deposition
DCE	(1,2)-dichloroethane
DGU	density gradient ultracentrifugation
DOC	sodium deoxycholate
EBL	electron beam lithography
EM	electromagnetic
FET	field effect transistor
FTIR	Fourier transform infrared spectroscopy
IR	infrared
MW	multi-walled
PEDOT	poly(3,4-ethylene dioxythiophene)
PMMA	poly(methyl methacrylate)
PSS	poly(styrene sulfonate)
RIE	reactive ion etching
RBM	radial breathing mode
SC	sodium cholate
SEM	scanning electron microscope
SERS	surface enhanced Raman spectroscopy
SNOM	scanning near-field optical microscope
SPM	scanning probe microscopy
SPP	surface plasmon polariton
SW	single-walled
TIR	total internal reflection
UV	ultraviolet

Contents

Introduction

This thesis concentrates on the interaction of conductive carbon-based materials with far-field light and surface plasmon polaritons, electron oscillations hybridized with a photon and localized on a conducting surface. A brief historical overview on these topics is given in this introduction.

Carbon is a versatile material even if only its allotropes are considered, not to mention its complex chemistry with a multitude of compounds. Elemental carbon has long been known to have different allotropes, including crystalline graphite and diamond, and additionally amorphous carbon. In the past few decades, new graphitic carbon allotropes with promising applications have been discovered.

Research concerning the simplest system of graphitic carbon, a single two-dimensional layer, can be considered to have began in 1947, when the band structure of a sp^2-bonded hexagonal carbon lattice was theoretically evaluated by Wallace [140]. Systematic isolation of these layers was achieved not until 2004 [102], when Novoselov and Geim separated single layers, named graphene, by repeatedly peeling graphite crystals with scotch tape.

More complex structures are possible when the edges of a single layer are connected to themselves. In 1985, Kroto et al. [77] published a report detailing mass spectroscopy of laser-vaporized carbon. A significant peak corresponding to stable clusters with 60 carbon atoms was seen when cluster-cluster interactions were maximized by cooling the graphite plasma in helium. For this spherical football-like cluster, the name buckminsterfullerene was proposed. This later led to the name for the whole family of such graphitic clusters, the fullerenes. Predictions of stable carbon clusters with a graphite plane rolled up to close itself had surfaced years earlier [107], but with little notice.

Elongated versions of fullerenes, carbon nanotubes (CNTs), had also not only been predicted but also produced and characterized years before interest in them took off [95]. Hollow carbon filaments with about 50 nm diameter were observed with transmission electron microscopy already in 1952 [112], and smaller filaments, most likely thick multi-walled (MW) CNTs, were identified in the 1970s [105]. In 1991 Iijima reported tubules growing from a graphite electrode in arc-discharge evaporation of carbon [62]. Research in a wider scale took off in 1993 [16], when single-walled (SW) CNTs were systematically synthesized with the arc-discharge method in combination with cobalt. Unlike fullerenes, that have few possibilities

for applications, carbon nanotubes have already been used commercially e.g. in mechanical composites, as conductive additives, in filters and as binders in lithium ion batteries [26].

Electromagnetic radiation, including visible light, exists as an oscillation of electric and magnetic fields, and it can travel without a medium or in dielectrics. On metal surfaces with almost free conduction electrons that can screen this radiation, far-field light is generally reflected. On the surface of a metal, however, there can exist a kind of slow light, which is an interplay of electron oscillations and an associated evanescent field [72].

These surface plasmon polaritons (SPPs) have been known for over a century, concerning both the propagation of radio waves on a surface of a conductor evaluated by Sommerfeld in 1899 [87] and as anomalies present in reflections of visible light on metallic gratings found by Wood in 1902 [113]. The theory that adequately explained these results was developed by Fano decades later [37]. Plasmons also started to be investigated using direct excitation by electrons at this time. Prism coupling was invented in the 1960s by Kretschmann [76] as a method to excite SPPs on smooth metal films.

Localized surface plasmons are essentially the same phenomenon on metal nanoparticles as SPPs on metal films. They have been unknowingly utilized since Roman times, and had their theory developed by Mie at the turn of the last century. The plasmon resonance, changing in wavelength as a function of particle size in metal colloids, was explained as an optically excitable oscillation of free conduction electrons in a metal particle [92].

The first applications for SPPs appeared in the 1970s, when Fleischmann, van Duyne and others began to study optical scattering from molecules attached on a silver surface. It was discovered that an enhancement in optical signal up to six orders of magnitude was possible, and this effect has later been put to use in surface enhanced Raman spectroscopy (SERS) [54]. A connected application, near-field optical microscopy utilizing a subwavelength feature to image below the diffraction limit, is useful for detecting SPPs. In the microwave region, this was experimentally realized in 1972, and for the optical range in 1984 by a group at IBM [103].

Interest in surface plasmons was renewed in late 1990s, when it was realized that SPP modes in metal nanostructures can be used to localize light signals far beyond the diffraction limit. Waveguides made of nanowires or nanoholes could be used to guide the plasmons [130], and sharp points would localize excitation [101]. It was also experimentally demonstrated that subwavelength hole arrays in metal films let more light through them at specific resonant frequencies than expected [32], which is useful for color filters. After these findings, the field concerning surface plasmons began to be referred to as plasmonics [48]. Recent additions for applications concerning plasmonics include near-field imaging and lithography, SPP-based sensors and spectroscopy, plasmonic antennas, metamaterials as well as signal pro-

cessing with active plasmonic components [87].

Polymers, long-chained hydrocarbons, are usually not good conductors as such. Intrinsically conducting polymers are a notable exception to this, having mobile charge carriers due to a combination of a conjugated backbone, charge transfer in ionic systems and additional dopants.

Generally, the basis of polymer science was founded in the 1920s, when the concept of macromolecules was developed by Staudinger [56], even though synthetic polymers, including plastics, had been in industrial production since the 19th century. Semiconducting organic compounds were developed in the 1950s, including charge transfer complex salts. The first conducting polyheterocycles, polypyrroles, were recognised as such in the early 1960s [33]. The fundamental breakthrough in highly conducting polymers was the 1977 discovery of the effect of halogen doping in polyacetylene [22], which exhibited metallic-like conductivity mostly due to charge transfer and polarons [56]. Until the 1980s, all highly conducting polymers were unstable in regard to their conductivity in the presence of oxygen and water, and had therefore little practical use. The discovery of stable, even water processable, polythiophenes made commercial applications possible. Transparent films of such materials are also available [33].

Initially, the main objective for this dissertation was to investigate the interaction of surface plasmons with carbon nanotube electronics, specifically the possibility to control the current in transistors with SPPs. After measuring chirality-controlled SWCNT films for their optical properties, the scope was expanded to include research on the unexpected optical resonances seen in such metallic-type films, which were also searched for in films of conductive polymers.

The background information for the experimental work in this dissertation is arranged in Part I. In Chapter 1 I describe relevant structural and electrical properties of carbon-based nanomaterials. Chapter 2 contains a review of their optical properties, including an overview of surface plasmons. A brief review on the synthesis of the relevant materials is included in Chapter 3. The experiments conducted by the author for this dissertation are described in Part II, arranged in the same order as corresponding included publications. Chapter 4 describes the gating of carbon nanotube devices with SPPs, both in the Kretschmann configuration (A.I) and with a scanning near-field optical microscope (SNOM). In Chapter 5 thin films of CNTs are measured in a total internal reflection configuration to probe their collective resonances (A.II), and Chapter 6 has similar measurements with conductive polymers (A.III). The findings are summarized in Chapter 7.

Part I

Properties of carbon-based nanomaterials

Chapter 1

Structure and electrical properties

A carbon atom has four valence electrons with which it can form chemical bonds. This leads to many possibilities for bonding, and is the enabling property for complex organic chemistry. In addition, carbon can bond with itself in several ways, which leads to a wealth of different allotropes.

When a carbon atom is bonded to four other carbons (via sp^3 hybridization), it results in the very hard and thermally conductive diamond structure. Diamond has a large band gap of 5 eV, which makes it a good insulator. Electrons also cannot be excited from the valence band to the conduction band optically, which results in a translucent appearance.

Graphitic materials on the other hand have a planar sp^2-hybridization, where one carbon atom is bound to three other carbons. In these materials the band gap is small or nonexistent. These structures include graphite, graphene, carbon nanotubes (CNTs) and fullerenes.

Linear acetylenic carbon or carbyne, where a sp^1-hybridized carbon atom is bound to two others, is also possible. Strong chemical activity which leads to instability in ambient conditions limits the usefulness of this allotrope, but these chains can be produced and protected in CNTs. [123]

1.1 Graphene

A single layer of graphite, graphene, is formed of carbon atoms with sp^2 hybridization, resulting in a hexagonal sheet as depicted in Fig. 1.1. The layer has to be sufficiently isolated from its surroundings to be considered graphene, as several layers bound to each other with van der Waals forces form graphite. [45]

Out of the four orbitals in carbon, $2s$, $2p_x$, $2p_y$ and $2p_z$, the three first ones hybridize with each other to form covalent σ-bonds, which determine the mechanical and thermal properties of the sheet. The $2p_z$ orbital points out of the plane, and orbitals of neighboring atoms couple with each other to form delocalized π-bonds [34]. Interactions out of the plane are very weak, so thermal and electric conductivies are

over 1000 times higher in the plane than out of it. In terms of the electron band structure, occupied π orbitals form the valence band and unoccupied π^* orbitals the conduction band. [3]

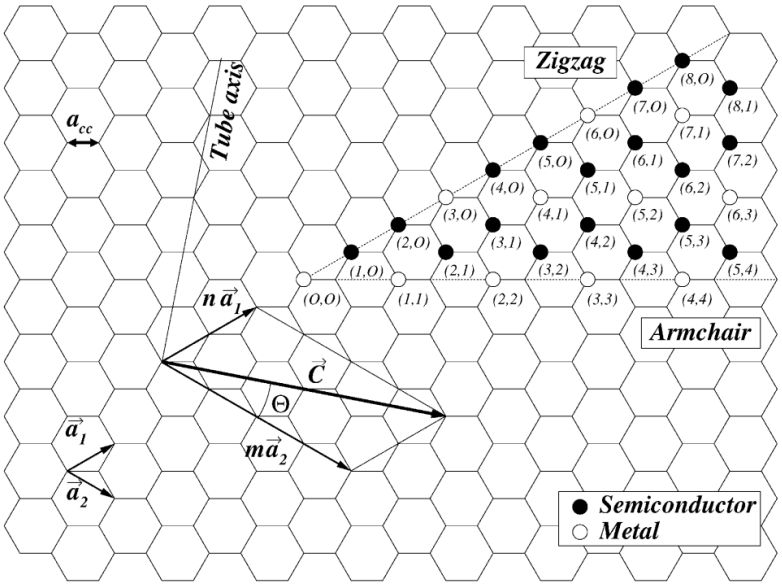

FIGURE 1.1 Hexagonal lattice of graphene with base vectors $\vec{a}_1$ and $\vec{a}_2$ used to define the chirality vector with integers n and m. With this vector, the orientations and widths of carbon nanotubes and graphene nanoribbons can be quantified. The vector defines the direction perpendicular to the SWCNT axis, and resulting tubes with (semi)metallic (white) or semiconducting (black) properties are marked. The chiral angle Θ is defined in relation to the zigzag vector. Adapted with permission of Elsevier from [15].

The electronic transport properties of graphene depend on the direction of propagation. The zig-zag direction parallel to the first vector $\vec{a}_1$ is metallic (but the zig-zag tube is not necessarily metallic), but the armchair direction ($\vec{a}_1 + \vec{a}_2$) is semiconducting, as defined in Figure 1.1. In graphene the conduction and valence bands meet at Dirac points as seen in Fig. 1.2, and therefore it is a zero-gap semiconductor for large areas, behaving as a metal. [17]

The first Brillouin zone represented in Fig. 1.2 is a primitive cell in reciprocal space (momentum space). The reciprocal lattice is the Fourier transform of the real-space lattice, and also is directly connected to the diffraction pattern produced by a crystal. The primitive cell for a repeating lattice is a minimum volume unit containing one lattice point that can be used to fill the lattice without gaps.

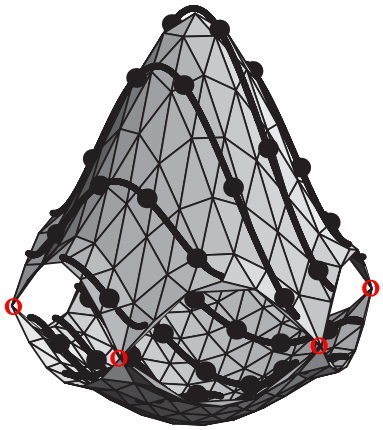

FIGURE 1.2 The constant energy surfaces (energy in the z axis) for the conduction and valence bands of a 2D graphene layer in the first Brillouin zone (in reciprocal space). The plot was calculated using the π-band nearest neighbor tight binding model. The bands touch in K points at the corners of the two-dimensional Brillouin zone, marked with red circles. The cutting lines for a (4, 2) nanotube energy band diagram are shown with dark solid curves, but translated to the first Brillouin zone of graphene. The tube (and similarly a graphene strip of the same orientation and width) can be seen to be semiconducting, as none of the cutting lines intersect the K points, resulting in a significant band gap. Adapted with permission of Elsevier from [28].

1.2 Carbon nanotubes

1.2.1 General properties

The edges of a sheet of graphene can be figuratively rolled up and attached to each other, forming more complex tubular or spherical structures. Relatively small and close to spherical carbon molecules structured in this way are called fullerenes, long cylindrical ones are carbon nanotubes. Carbon nanotubes can be single-walled (SWCNT) or multi-walled (MWCNT).

MWCNTs usually consist of concentric and coaxial SWCNTs of different diameters and chiralities, which are bound to each other with van der Waals forces. A scrolled up graphene sheet forming multiple layers is also a possible configuration. Because at least one of the concentric tubes is likely to be metallic or the scrolled-up sheet is wide enough, usually MWCNTs behave electrically as zero-gap metals. [15]

Because carbon nanotubes can be considered as wrapped up sheets of graphene, their properties are analogous to graphene strips of different widths and directions of the lattice. Thus, electrical transport properties in SWCNTs can be explained by considering transport along different directions in a graphene sheet.

The chirality of a SWCNT can be defined with a chiral vector, that can be defined with the unit vectors of the lattice $\vec{C} = n\vec{a}_1 + m\vec{a}_2$. Here the integers ($n$,$m$)

specify the nanotube structure, as $\vec{C}$ also defines the circumference of the nanotube as seen in Fig. 1.1. The diameter d of the SWCNT is therefore

$$d = \frac{C}{\pi} = \frac{a}{\pi}\sqrt{n^2 + nm + m^2}. \tag{1.1}$$

The distance a is the lattice constant of graphene, which is $\sqrt{3}$ times the distance between carbon atoms (1.42 Å).

Because of the direction dependence in the conductivity of graphene, the chirality of a nanotube has an effect on its conductivity. Because of their small diameter, the directions of conduction in the hexagonal lattice are quantized, and the direction of the tube axis determines the bandgap of the tube. It must be noted that the same names used for directions on a graphene sheet are also used to name nanotubes, where they define the circumference, and therefore an armchair tube (n=m) is metallic and has a 0 eV energy gap, while this direction in a graphene sheet is semiconducting. Additionally, semimetallic tubes (n-m divisible by 3) have a small energy gap. Both of these are marked as metals in Fig. 1.1. The remaining two thirds of possible SWCNTs are semiconducting. All these types can be grouped by the remainder mod$(2n + m, 3) = 0, 1, 2$ where the groups are metallic, type-I semiconducting and type-II semiconducting, respectively. The two types of semiconducting SWCNTs signify different branches that have differences in transition energies, relevant to optical properties as seen later in Fig. 2.2.

Additionally, SWCNTs have handedness. The zigzag ($m = 0$) and armchair tubes are achiral, but the others are either right-handed ($n > m$) or left-handed ($n < m$) [31]. The enantiomers are sometimes seen to be denoted as either + for right or - for left so that the chiral indices have always $n \geq m$, as is the convention also if enantiomers are not considered. These enantiomers have differences concerning the rotation of polarized light in them (circular dichroism), and chiral molecules can also have differing interactions with them. [20]

Carbon layers with *sp*^{2} hybridization are attracted to each other due to van der Waals forces, which in the case of flat sheets will result in graphite. These forces cause SWCNTs to easily bind to each other, forming bundles. In suspensions this can be partially prevented by using suitable solvents such as (1,2)-dichloroethane, tetrahydrofuran or ethanol. A more effective solution is to use surfactants, often aromatic in one end, which enables the suspension of CNTs in a polar solvent, such as water. SWCNTs will also generally stick to solid surfaces, making their removal difficult. [60]

1.2.2 Carbon nanotube field effect transistors

In transistors the current through a channel is controlled by another current (bipolar transistor) or a voltage (field-effect transistor, FET). In a FET a transverse electric

field affects the longitudinal motion of the charge carriers and the carriers are either holes or electrons, making it a unipolar device [68]. It has three terminals: the current in the channel between the drain and the source (I_{ds}) is controlled both by the applied voltage between these (V_{ds}) and an applied voltage at the gate electrode (V_g), which is separated from the channel with a dielectric. For simple circuits, the substrate (usually highly doped silicon) can be used as a backgate, but for individual control of several devices topgates are needed.

The metal-oxide-semiconductor field effect transistor (MOSFET) is the most common type of transistor currently in use. Their size for executing a certain function is smaller and fabrication requires fewer steps than bipolar junction transistors. Both types of transistors are based on doped semiconductors, usually silicon. *N*-type doped semiconductors have a larger electron than hole concentration as charge carriers, which means using a donor dopant with excess electrons (group-V element such as phosphorus for silicon). With a *n*-type channel, the energy barrier blocking current is in the conduction band so a positive applied gate voltage lowers the barrier and opens the channel. In contrast, *p*-type ones have holes as main charge carriers, using an acceptor dopant (group-III element such as boron for silicon). The barrier in this case is in the valence band, and conductivity is increased with a negative V_g. [68]

For scaling down the transistor size even further, using semiconducting SWCNTs as the channel is an option. The resulting CNT FET was first realized in 1998 [132]. These devices have typically been made on silicon and an oxide with metal contacts like conventional transistors, with the SWCNT taking the place of the intrinsic silicon channel. The cylindrical tube also in principle allows surrounding the channel with a gate, in addition to the more common backgate or topgate configurations. CNTs with metallic behavior (or graphene) can be also used as electrodes, and recently all-carbon CNT FETs have been demonstrated, where even the dielectric layer and substrate can be hydrocarbons (plastics) [2].

The CNT FET can have ballistic transport [64], if the only resistance present is quantum resistance. In this case no carrier scattering or energy dissipation would take place in the body of the CNT, and the on-current resistance would be determined by the number of conduction modes within the CNT. For a single metallic-type tube this would be $R = \frac{h}{4e^2} = 6.45$ kΩ [6]. In practical devices, this is limited by imperfections in both the tubes and the contacts. The driving electric field (to not excite the RBM) and the temperature also need to be low, but at room temperature channel lengths of less than 100 nm can be ballistic.

In practice, the properties of metal contacted CNT FETs are usually caused by Schottky barriers at CNT-metal contacts [58]. The different work functions of the materials at these interfaces lead to charge transfer and a dipole, producing energy barriers at both source and drain as seen in the insets of Fig. 1.3. If one of the barriers is much higher than the other, the behavior is unipolar, and the device shows *n*- or

p-type behavior depending on the work function difference between the metal and the CNT [21].

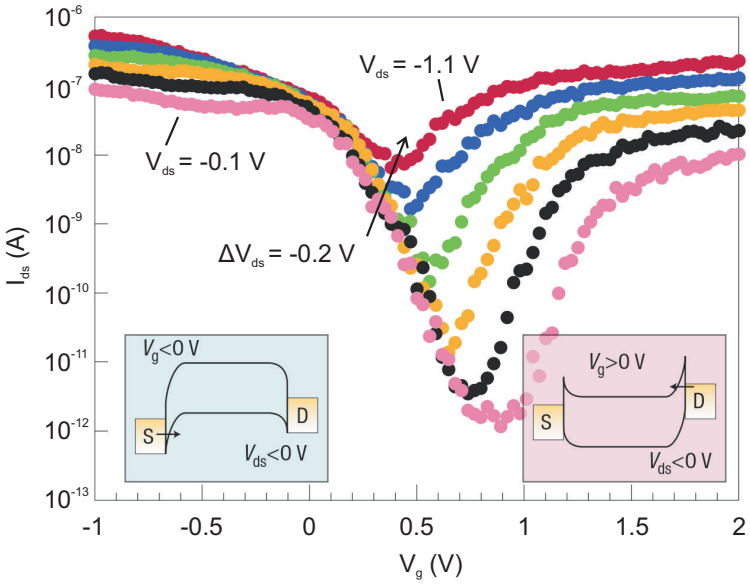

FIGURE 1.3 Drain-source current in an ambipolar FET with a single SWCNT, displaying *p*-type behavior at low V_g. The energy band structure is shown in the inset at lower left, which shows holes injected from the source (S) The behavior changes to *n*-type at high V_g, with electrons injected from the drain (D) (inset at lower right). Drain-source bias changed at steps of -0.2 V in curves from bottom to top. Adapted by permission from Macmillan Publishers Ltd: Nature Nanotechnology [6], copyright 2007.

For example, devices with palladium electrodes contacting the semiconducting SWCNT channel have a *p*-type behavior, where current increases with a negative gate voltage. Pd has a work function (5.2 eV) relatively close to the SWCNT (4.8 eV [83]), which results in a better *p*-type contact, since the valence band is close to the metal Fermi level. If the work function is low for the contact material (e.g. Al 4.1 eV and Ti 4.3 eV), electron transport is optimized and hole transport inhibited. Thus, the contact is more likely to be *n*-type and the channel is opened with a positive gate voltage. Typically transfer across the Schottky barrier is dominated by tunneling rather than thermally activated emission over the barrier, and the thickness of the barrier is critical [6].

Additionally, with an asymmetric CNT FET with different gate dielectric thicknesses close to drain and source (using either a back- or topgate) it is possible to switch between *n*- and *p*-type behavior by changing the sign of the drain-source voltage [57]. CNT FETs with thin gate oxides can also be ambipolar as in Fig. 1.3 so that both holes and electrons contribute to conduction, and the channel is opened at both negative or positive gate voltages [6].

In addition to these Schottky-barrier CNT FETs, it is possible to dope parts of the nanotube to form *p*- or *n*-type regions to make a drain and source, and leave

an intrinsic portion as the channel. When gate voltage is applied to these regions, the device operates more like a conventional FET. Such a configuration can also be equipped with a wrap-around gate on the tube, promoting tunneling effects with a very effective gate control [73]. SWCNTs doped so that they have internal p-n junctions can also be used as highly efficient photodiodes [43]. Reduced graphene oxide can also be used as an electrode material in a CNT FET, resulting in *p*-type behavior in ambient conditions [80].

The current in a CNT FET is usually dependent not only on the bias voltage V_{ds} and the gate voltage V_g, but also on previous V_g. The hysteresis is generally caused by trapped charge, but there is disagreement whether the relevant charge traps (mobile or immobile), located in the gate dielectric, are caused by defects in the CNT or are connected to water molecules adhered to the dielectric [115]. The dielectric layer of the CNT FET in any case plays a major role in hysteresis.

The modulation of current through a semiconductor requires either an excitation of charge carriers over the band gap or the modification of the band itself. The former can be accomplished with heat or light, and the latter most commonly by applying an electric field, but also with chemical doping, mechanical strain or magnetic field.

Changes in CNT conductivity can be produced by photon excitation, which produces electron-hole pairs that are separated by the applied field. In CNT FETs the Schottky barriers at CNT-metal contacts and defect sites in the CNTs have internal fields that also separate electron-hole pairs [6]. Alternatively, a photovoltage can be generated in the open-circuit configuration. In both cases the active sites can be imaged with a laser-scanning microscope [41] or a SNOM (Section 4.2).

Surface plasmon polaritons (SPPs) can have similar effects on the CNT FET as far-field optical excitation, but because the SPP is highly localized on the interface, the amount of power needed is much lower if the active area is in the range of the SPP. Gating by SPPs complicates the design of the CNT FET in relation to far-field optical excitation. This is because a plasmonic metal is needed in close proximity (less than 100 nm) of the CNT channel and especially the Schottky barriers due to the limited extent of the SPP. This is discussed further in Chapter 4.

In addition to effects related to the CNT and its contacts, light absorption in a semiconducting substrate can generate a photovoltage, which can have a larger effect than direct electron-hole generation in the CNT. In the case of an interface between silicon and silicon dioxide, this photovoltage in the backgate can be up to -160 mV for a 633 nm, 4 mW laser. This effect is visible even if the laser spot is at a large (mm scale) distance from the CNT. [89]

The electronic properties of CNTs can be modified with the addition of electron donors (e.g. alkali metals) or acceptors (e.g. halogens) with physical adsorption, encapsulation or intercalation in bundles. Additions with covalent bonding are also possible, such as substitutional doping and sidewall functionalization. [159]

Adsorption of chemicals can have a large effect on the conductivity of the CNT.

Chemical species that are weakly bound via van der Waals forces can be easily removed with relatively weak optical excitation [138]. Physisorbed oxygen in particular is present on CNT FETs when they are exposed to air, and it has a large effect on electronic properties [24]. The physisorption of O_2 molecules causes the CNT FET to have more holes as carriers (p-type), increasing the on-current of semiconducting nanotubes if the device was already p-type [93]. An n-type annealed CNT FET (Au electrodes) can be converted to p-type by oxygen exposure, as seen in Fig. 1.4a.

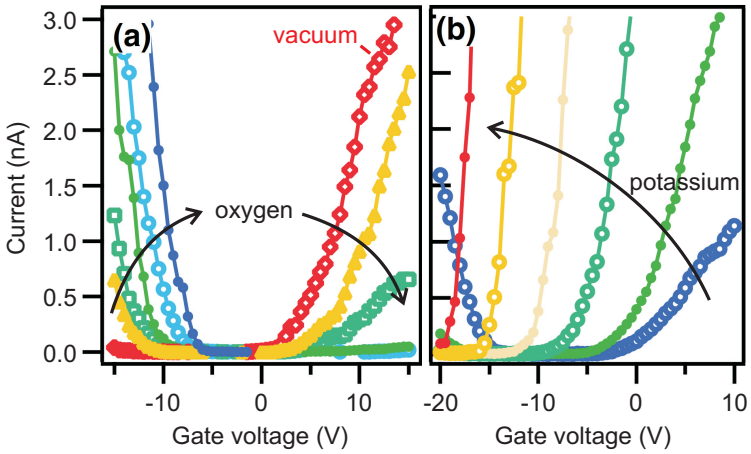

FIGURE 1.4 Drain-source currents measured in a FET made with 1.4 nm diameter SWCNTs deposited on gold electrodes with 120 nm SiO_2 on Si, V_{ds} = 0.5 V. [27] a) Effect of oxygen. The device is n-type after thermal annealing in vacuum (red), and the response changes gradually to p-type when oxygen exposure (2 min at a time) is gradually increased from left to right: $P = 10^{-4}$ Torr (orange), $P = 5 \times 10^{-4}$ Torr (turquoise), $P = 5 \times 10^{-3}$ Torr (green), $P = 10^{-1}$ Torr (light blue) and ambient (dark blue). b) Effect of potassium doping (e^- donor) on a similar CNT FET. The curves from right to left (blue, dark green, turquoise, yellow, orange, red) correspond to doping cycles with increasing deposited amounts of adsorbed potassium. Adapted figure with permission from [58]. Copyright 2002 by the American Physical Society.

Like O_2, NO_2 causes p-type behavior, while NH_3 is an electron donor, resulting in n-type behavior. Due to physisorption, CNT FETs can therefore be applied as gas sensors [18]. For these effects there can be two reasons: either the doping of the CNT itself or the modification of the Schottky barrier at the tube contact. Initially the first explanation was assumed, but later there have been specific experiments showing that the CNT-metal contacts specifically are sensitive to gases, for example by shielding only the contacts from gases [157] or comparing the electrical response to actual doping with alkali metals as seen in Fig. 1.4b [27]. Technically for adsorption of gases there is no doping involved, but a modification of the work function at the metal surface. [58]

The conductivity of a CNT is also scaled by changes in temperature, but the effective gate voltage is not changed [12]. This dependence can be relevant also when using optical excitation, since high-intensity light can also raise significantly the

temperature of the CNT FET. Freestanding CNTs are most affected by this, because contact with a substrate will in most cases conduct the heat effectively, equalizing the temperature of the device with its substrate.

1.3 Conductive polymers

1.3.1 General properties

Organic compounds are generally poor conductors, since normally the valence electrons of the carbon chain are bound in sp^3-hybridized covalent bonds (like in diamond) and have low mobility. However, if the polymer backbone has a continuous chain of sp^2-hybridized carbons, there are delocalized electrons (like in graphene or CNTs), which become mobile when these conjugated orbitals are partially emptied. This conjugated chain can also be considered to have alternating single and double bonds between carbon atoms. If the material has ionic components, a charge transfer complex can be formed, which facilitates conductivity between the components. Additional secondary dopants can also be used, which cause permanent doping in contrast to the ionic component (primary dopant). These factors combine to result in high charge mobility and a low band-gap for the polymer matrix, which is generally also an ionic liquid. [109]

Relative to other conductors, the main advantage of these conductive polymers is processability. As flexible materials, they can be used in applications with mechanical stress, and can be readily applied as a solution. In general, solution processing offers a cheaper alternative, since spin coating and inkjet or screen printing can be done in ambient conditions [137]. Fabricating thin films of metals or metal oxides conventionally requires vacuum technology with methods such as CVD, sputtering and vacuum evaporation. An emerging application of electroluminescent conducting polymers is in organic light-emitting diodes. However, commercially available displays use mostly small-molecule emitters, because polymer-based displays currently have durability issues, even though they have potentially lower manufacturing costs.

1.3.2 PEDOT:PSS polymer

Poly(3,4-ethylene dioxythiophene) (PEDOT) is the most used conducting polymer in commercial terms, with antistatic coatings as its main application. As itself, it has a poor solubility in water and a blue color. To counter the solubility problem of PEDOT, a polyelectrolyte complex can be formed in the right conditions. The polycation (+) PEDOT is mixed with a polyanion (-) to form a stable dispersion [33]. Poly(styrene sulfonate) (PSS) is the most common choice for a counterion. PSS is always used in excess and the PEDOT:PSS weight ratio in standard dispersions

ranges from 1:2.5 to 1:20. Aqueous solutions of this material can be used to produce films with good transparency in visible wavelengths. These are available as water-based low viscosity inks that can be used in inkjet printers, and as ink pastes suitable for screen printing.

The structure of a thin PEDOT:PSS film consists of PSS-rich regions laying parallel to the film, which results in a highly anisotropic electrical conductivity. In spin-coated films less than 100 nm thick at room temperature, the conductivity parallel to the film (10^{-3} S/cm) can be several hundred times higher than perpendicular to it (2×10^{-6} S/cm, these low conductivity values are without secondary dopants). [100]

The non-stoichiometric doping with PSS can be considered as primary doping, but secondary dopants can be added to greatly enhance the conductivity of PEDOT:PSS. Their inclusion is thought to alter the structure of the PEDOT network rather than actually doping it, and added conductivity is retained even after their removal. These include polyvalent alcohols, several organic solvents, surfactants and salts. Dimethyl sulfoxide in particular can increase conductivity by a factor of 800. With additives PEDOT:PSS can reach stable conductivities of hundreds of S/cm. [33]

In addition to secondary dopants, conductive nanostructures can be used to enhance the conductivity of the polymer further. Adding graphene as flakes can increase the conductivity of PEDOT:PSS. Alternatively the same can be done with plain PEDOT by using sulfonated graphene flakes as the anion. The PEDOT:PSS/-graphene composite can either be deposited directly, or via addition of EDOT monomer and subsequent polymerization in situ [152]. In a similar fashion, MWCNTs can be dispersed in PEDOT:PSS as a conductivity-enhancing component [153]. Single-walled CNTs can be used similarly, but for these tubes carboxylic acid functionalization is preferred to increase solubility and to decrease bundling [98]. PEDOT:PSS/-graphene ink is commercially available from Innophene, and it has been used as a transparent electrode material for piezoelectric touch sensors [139] and for stretchable electrodes [136].

Chapter 2

Optical properties

2.1 Absorption and reflectance

2.1.1 Graphene

Over the visible spectrum, freestanding graphene has a measured transmittance of 97.7 %. For graphene samples of a few layers, the absorbance can be estimated to be directly proportional to the number of layers, since the reflectance of graphene is very small (less than 0.1 % for a single layer). [88]

This result can also be derived by assuming that graphene has an optical sheet conductivity of $\sigma = e^2/(4\hbar)$, and using the Fresnel equations at the thin-film limit, resulting in an absorbance of $\pi\alpha \approx 2.3$ %. Here α is the fine-structure constant. [17] As a result, the absorption spectrum of pure graphene does not have any peaks at visible frequencies, but plasmons change the situation at higher energies (see Chapter 5).

2.1.2 Carbon nanotubes

The optical absorption of single-walled CNTs is dominated by the E_{nn} transitions that correspond to the energy differences between the van Hove singularities in the density of states (DOS) of the SWCNTs. The singularities have a high number of electronic states at a certain energy, corresponding to critical points of the Brillouin zone as shown in Fig. 2.1.

Initially the optical resonances were thought to result from band-to-band transitions. The band-to-band model, however, did not fit with experimental results in the case of the ratio between energies E_{22}/E_{11}. The discrepancy was explained by an excitonic model due to the one-dimensionality of the CNTs [141]. The excitons are produced mainly due to the previously mentioned transitions between the van Hove singularities. Further support for the excitonic model can be found in the photoconductivity spectra of SWCNTs, which have a sideband corresponding to simul-

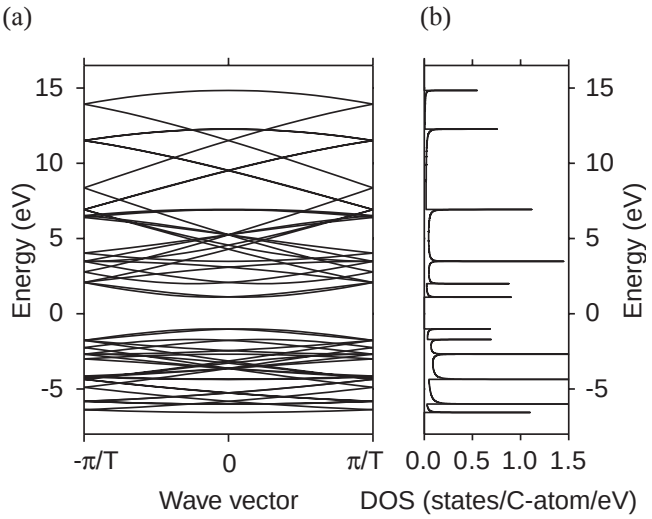

FIGURE 2.1 a) Electronic energy band diagram for the (4,2) nanotube obtained by zone-folding from the graphene layer calculation in Fig. 1.2. b) Density of electronic states for the band diagram shown in a). The (4,2) tube with a diameter of 0.4 nm is close to the limit of the smallest possible SWCNT [160], and would need to be inside another tube to be stable. Republished with permission of Elsevier from [28].

taneous excitation of the exciton and a C-C bond stretching phonon in addition to the main excitonic resonance [111].

The excitons are strongly correlated electron-hole pairs, and their excitation is dependent on the polarization of incoming light in relation to the nanotube axis. SWCNTs therefore have more optical absorption when the polarization is parallel to the tube axis, and similarly the relative intensities of the surface and bulk π plasmon peaks at 4-6 eV (Section 2.3.3) are polarization dependent [97]. Aligned carbon nanotube forests have a clearly anisotropic optical response in reflection, showing differences between *s*-polarized light (perpendicular to the tubes), which can be modelled as a mixture of graphite and air, and *p*-polarized reflection, which has been difficult to model. [84]

The E_{nn} transition energies are determined by the chiralities of the CNTs, and they can be plotted as a Kataura plot [70]. In different branches the periodic oscillations show the dependence of the transition energies on the (n,m) indices, overlapping the general dependence on tube diameter.

Semiconducting SWCNTs exhibit photoluminescence, meaning that when excited at a higher state (e.g. E^S_{22}, the superscript denotes a semiconducting tube here) they can re-emit part of the energy as a photon corresponding to a lower energy transition (e.g. E^S_{11}). Due to a lack of a band gap, metallic SWCNTs do not have this property. Using photoluminescence is the easiest way to identify semiconducting single chiralities, in practise scanning excitation with a light source through optical wavelengths and observing spectra at each step [154].

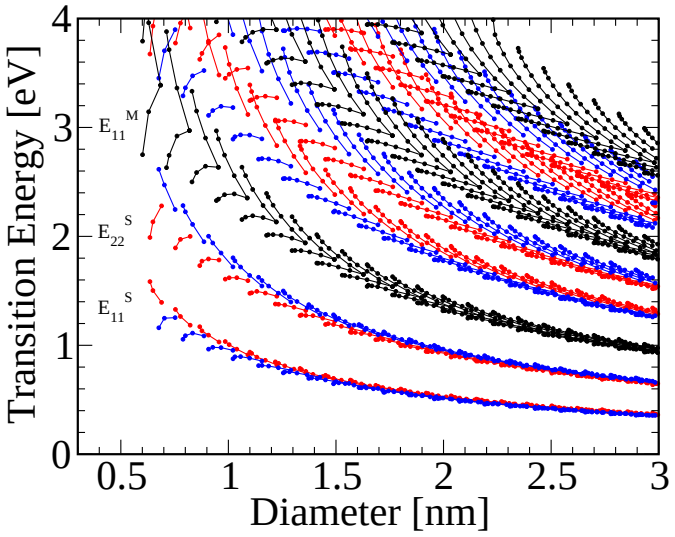

FIGURE 2.2 Excitonic transition energies of SWCNTs as a function of tube diameter, widely known as the Kataura plot. The plot is calculated with constant dielectric constant $\epsilon = 2.22$, not taking into account environmental effects. It includes all tubes in the diameter range 0.59 nm to 3.0 nm, in chiral indices from (7,1) to (31,4). The SWCNTs are grouped metallic (black), type-I semiconducting (red) and type-II semiconducting (blue). The exciton energies are plotted from E_{11}^S to E_{66}^S for semiconducting and E_{11}^M to E_{33}^M for metallic tubes. Data with permission from [104, 120].

2.1.3 Conductive polymers

General properties

Metallic properties in a material usually prevent optical transparency, since photons with frequencies lower than the plasma frequency are reflected, and metallic elements have this frequency in the UV range. The plasma frequency ω_p depends on the density of conduction electrons n_e as $\omega_p = \sqrt{4\pi n_e e^2/m^*}$, where e is the electron charge and m^* the effective mass of the electron in the solid. For metals $n_e \approx 10^{23}$ cm^{-3}, while for metallic polymers and some doped metal oxides $n_e \approx 3 \times 10^{21}$ cm^{-3}. This low density leads to a energy value of about 1 eV for the plasma frequency, which allows visible transparency in this regard. However, interband transitions lead to some optical absorption also in the visible range. [56]

Transparent electrodes made of such conductors have applications especially in flat panel displays and photovoltaics. Currently doped metal oxides are the materials of choice for these applications, with indium tin oxide being the most widely used one. These materials are brittle and relatively expensive, and for flexible displays or solar panels conducting polymers can be used. Currently the most prominent application for transparent conducting polymers is in antistatic coatings [33].

Optical anisotropy

In relation to experiments in Chapter 6 the concept of optical anisotropy is relevant, and thus it and the means of its measurement are briefly reviewed here. Most materials are optically isotropic, i.e., their refractive index is the same in all directions of propagation in the material. Optical anisotropy or birefringence can occur if a material has an asymmetric (but regular) structure over macroscopic distances (much longer than the wavelength of light). Crystals with asymmetric lattices are the most common examples of this phenomenon, and polymers under stress can exhibit the same behavior.

A common method for measuring the refractive index of a material is ellipsometry, which is based on the polarization change of light when it interacts with the measured material. The signal depends both on the properties of the material as well as its thickness. Ellipsometers using a laser with a single wavelength are primarily used for measuring thickness. Measurements by spectroscopic ellipsometers are done as a function of wavelength, and they can be used to calculate the dielectric function of a material across the measurement range. [106]

Standard ellipsometry assumes an isotropic material, where *s*- and *p*-polarized light are not converted to each other. However, if the sample is uniaxially anisotropic and the optical axis is perpendicular to the surface, standard ellipsometry is still sufficient. Generalized ellipsometry also accounts for arbitrarily anisotropic samples. [106]

Reflection anisotropy spectroscopy on the other hand can be considered as a development of spectroscopic ellipsometry, but it uses linearly polarized light at a nearly normal incidence. The reflectance difference between two orthogonal polarization directions is measured, which yields information about the optical anisotropy of the surface layer. Typically it has been used for studying the surfaces of metals, semiconductor crystals or liquid crystals and their growth based on their optical anisotropy. [145]

PEDOT:PSS

The optical absorption of the conductive polymer PEDOT:PSS is mainly contributed by PEDOT, and it depends heavily on the oxidation state of this conductive component. In the mostly oxidized form the absorption is higher in the red part of the visible spectrum, giving the transparent polymer a bluish appearance as seen in transmission spectra in Fig. 2.3. In the partly neutralized form (that can be obtained by inserting a negative voltage in the 1 V range) the polymer is in contrast strongly absorbing in the visible region [33]. The anisotropy caused by the plate-like PSS-rich regions in thin films extends to optical properties, and optical absorption is higher in the film plane than perpendicular to the surface.

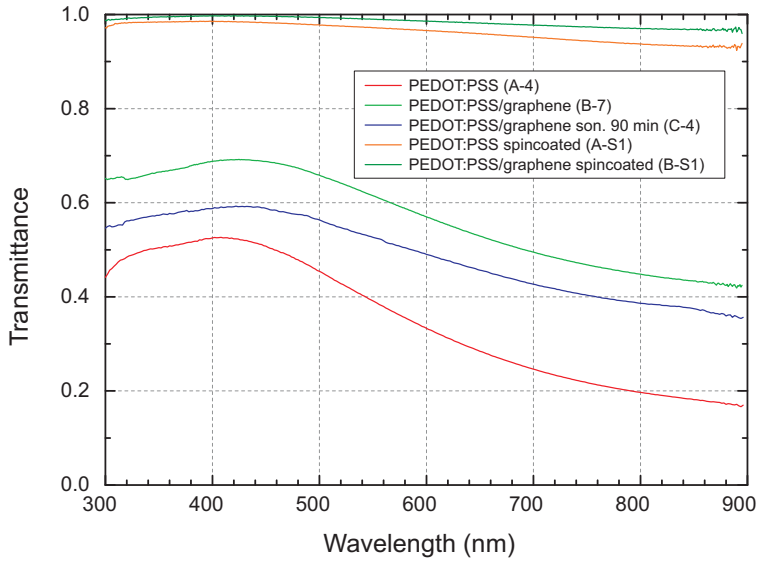

FIGURE 2.3 Optical transmittance spectra measured from differently prepared thin PEDOT:PSS polymer films. The film thicknesses for spray-coated samples are 1050±100 nm (A-4), 1020±50 nm (B-7) and 900±50 nm (C-4). The spin-coated samples have thicknesses of 29±1 nm (A-S1) and 34±5 nm (B-S1). The samples are the same as in article A.III.

2.2 Raman transitions

In a molecular system, inelastic scattering of light can reveal vibrational and rotational modes. In Raman scattering, an incoming photon interacts with the molecule, putting it to a short-lived virtual energy state before the photon is scattered. As a result, the scattered photon can be shifted in energy by an amount corresponding to a low-energy excitation, while the molecule ends up in a different vibrational or rotational state. Raman spectroscopy is based on measuring this shift, which at low temperatures occurs at high probability to lower energies. This phenomenon is called the Stokes shift. If the molecule wasn't at the ground state, the shift can also occur to a higher photon energy (anti-Stokes shift). Depending on the interactions of the dipoles in the molecule, only some of the rotational and vibrational modes could be Raman active, while some might be infrared active (visible in IR spectroscopy), while some might be optically inactive.

In a quantum mechanical oscillator, there are a number of allowed states with different potential energies. Fundamental transitions, moving only one level in energy, occur most commonly. An overtone, seen as separate bands in Raman spectra, occurs when a vibrational mode is shifted in one process by two levels (first overtone), three (second overtone) and so on.

Elastic Rayleigh scattering with no shift accounts for most of the observed scattered light, which needs to be filtered out in Raman measurements. For this practical reason, Raman measurements need to be done with monochromatic light, and the

choice of this frequency also affects the result. If the excitation energy is close to an electronic transition in the sample material, Raman scattering can be greatly enhanced. This resonance Raman spectroscopy leads to shorter measurement times, and the frequency of the excitation laser can also be used to select which compound (or even part of a molecule) gives most of the Raman signal from a sample. [66]

2.2.1 Graphene

For allotropes of carbon Raman spectroscopy provides an easy way to evaluate the quality of the material. Highly symmetric covalent bonds with a small or nonexistent natural dipole moment are the most suitable for Raman spectroscopy, and carbon-carbon bonds are a great fit for these criteria. For a single crystalline diamond sample the spectrum is very simple, as there is only a single Raman transition visible for the sp^3-bonds at an energy of 1332 cm^{-1}.

For graphitic carbon materials the G mode is a common feature, found at 1582 cm^{-1} in graphite, originating from an optical phonon in sp^2-bonded carbon. The planar sp^2-bonds have a higher energy and thus higher vibration frequency than sp^3-bonds, pushing the observed shift to a higher frequency [143]. The G mode can be seen clearly in all the materials in Fig. 2.4 with some additional shift.

The amount of defects can be evaluated by the intensity of the D mode at 1345 cm^{-1}, which is due to the breathing modes of hexagonal carbon rings. This mode requires a defect for its activation due to the need to conserve momentum for a single phonon to excite it. The band is produced due to a double resonance, where an electron-hole pair is created by the absorbed photon. The electron is scattered by a phonon and then scattered back by a defect (or vice versa) and recombined with the hole, emitting a photon with shifted frequency [134]. In such a double resonance process the energy of the scattered phonon (and the Raman peak) is dependent on the laser excitation energy [117]. The double resonance can also be produced as an intravalley process, giving the less intense D' peak at 1600 cm^{-1} [40].

The 2D (sometimes denoted G') peak at 2680 cm^{-1} is the D-peak overtone, but it does not require defects for activation, since the momentum conservation for this mode is satisfied by two phonons with opposite wave vectors. Similarly, the 2D' mode, being is an overtone for D', is present even without defects. Being produced by a double resonance, these peaks are also dispersive in regard to the excitation energy.

The Raman spectrum of single layer graphene is dominated by the 2D peak as seen in Figure 2.4 [29]. The 2D peak is roughly four times as intense as the G peak. This splits into four components with a double layer, and eventually transforms to two peaks in bulk graphite [39]. The D and D' modes, being related to defects in the carbon lattice, are forbidden in intact graphene due to the Raman selection rule [52], but are visible in damaged graphene (Fig. 2.4). There can also be combination bands,

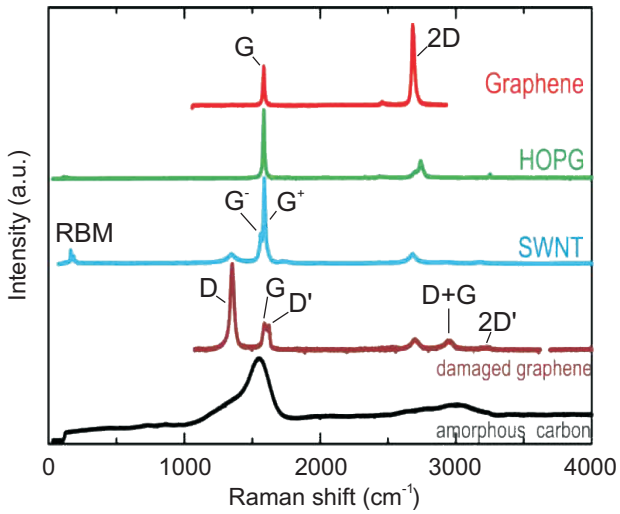

FIGURE 2.4 Raman spectra of (from top to bottom) crystalline monolayer graphene, highly oriented pyrolytic graphite, SWCNTs in bundles, damaged graphene and amorphous carbon. Adapted by permission of the publisher (Taylor & Francis Ltd) from [117].

where two fundamental modes are excited simultaneously, such as the D+G peak labeled in Fig. 2.4.

2.2.2 Carbon nanotubes

The main additional feature seen in Raman spectra of CNTs are the radial breathing mode (RBM) bands, which correspond to the expansion and contraction of the tubes. Depending on the diameter of a single tube and their aggregation state, the RBM can be seen in the range of 100 cm^{-1} to 350 cm^{-1} for tubes with diameter between 0.7 nm and 2.5 nm [66]. The shift is smaller with a thicker tube, and RBM signals of large diameter SWCNTs are usually too weak to be observed [28].

RBM phonons are not visible in tubes with two or more walls, because the outer tubes restrict the breathing mode. The D mode is much more prominent in MWCNTs compared to SWCNTs due to the multilayer structure and a higher amount of disorder. Thus, multi-walled CNTs are similar to damaged graphite in Raman measurements.

In SWCNTs, the G band splits to G^+ and G^- bands, and the latter differs in lineshape, linewidth and energy depending on whether the tube is semiconducting or metallic. Additionally, the split is larger in a thinner tube. [117]

2.2.3 Conductive polymers

As relatively complex organic compounds, the Raman spectra of conductive polymers are generally much more complex than of carbon allotropes. For PEDOT, Raman can be used in determining its properties, most notably its oxidation state by

the relative height of Raman peaks [44]. The stretching modes of C=C bonds at 1400 to 1500 cm^{-1} are the most prominent peaks, and they have been used to distinguish between coiled and linear structures of the polymer. The linear conformation is generally more conductive, and can be achieved by secondary doping. [33].

2.3 Plasmons

2.3.1 Surface plasmon polaritons

In metals, the oscillation of free electrons has a large contribution to optical properties. These plasma oscillations are plasmons, and the charge density oscillates at the fundamental plasma frequency. Photons arriving at a metal surface are reflected if they have a lower frequency than this, because the charges screen the electric field of the photon. In practice, the free electrons in the metal are oscillating at opposite phase relative to the driving electric field [103]. Photons with higher energies are transmitted, because the oscillations cannot keep up with the frequency of the incoming electromagnetic radiation. For conventional metals the plasma frequency is in the ultraviolet (UV) range, making them reflective for visible light [56].

When a plasma oscillation is confined to a surface it is called a surface plasmon. Unlike the previous bulk plasmon, in a surface plasmon the electron oscillation is inseparably coupled to a photon. The photon is the electromagnetic oscillation outside the metal in connection to the electron oscillation. The resulting quasiparticle is a surface plasmon polariton (SPP, Fig. 2.5). [121]

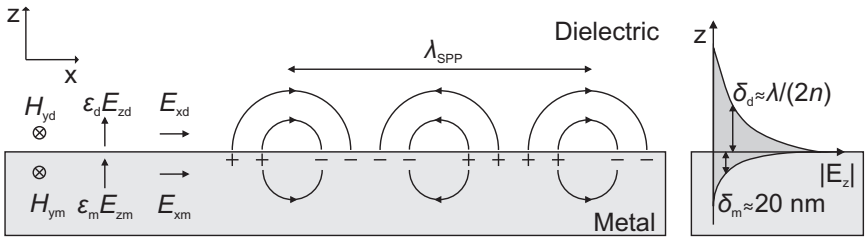

FIGURE 2.5 Schematic of the charge distribution and the electric fields of a surface plasmon polariton propagating in the x-direction on an interface between a metal (index m) and a dielectric (index d). The sketch shows on the left the magnetic field H, electric field E and the wavelength of the SPP λ_{SPP}. On the right the penetration depths δ of the electric field are shown. The other symbols are the free-space photon wavelength λ and the refractive index of the dielectric n. [78, 135, 155]

Surface plasmon polaritons are strongly confined to the dielectric-metal interface, so they can also occur in structures smaller than the wavelength of light used to excite them. Two-dimensional electron gases can also support surface plasmons as in the case of graphene (Subsection 2.3.3). The behavior of a SPP can be evaluated

by solving the Maxwell equations for an electromagnetic wave at a flat dielectric-metal interface [155]. The solutions for SPPs are wavelike parallel to the plane and the field amplitudes have exponential decay into both media from the interface.

A wavevector can be used to describe a wave, so that it points in the direction of its phase velocity. The magnitude of the wavevector is the wavenumber k, the spatial angular frequency, describing the number of oscillations (in radians) per unit of space. It relates to the wavelength λ of the wave as $k = \frac{2\pi}{\lambda}$. In contrast, the temporal angular frequency $\omega = \frac{2\pi}{T} = 2\pi f$ describes the oscillations in relation to the time period T or inversely to the frequency f. The energy of a photon is directly proportional to this as $E = \hbar\omega$, where $\hbar$ is the reduced Planck constant.

From the solution for these waves on the interface the wavenumber of the SPP as a function of ω is

$$k_{SPP} = \frac{\omega}{c}\sqrt{\frac{\epsilon_d \epsilon_m}{\epsilon_d + \epsilon_m}}. \tag{2.1}$$

This is called the dispersion relation, and it depends on the permittivities of the dielectric (ϵ_d) and the metal (ϵ_m). The permittivity measures how much resistance a medium provides in response to an electric field. For the dielectric the function ϵ_d is real and positive, but for the metal ϵ_m is complex and negative. The frequency dependent permittivities need to have opposite signs for the SPP to be excited.

From Figure 2.6 it can be seen that a free-space photon has always less momentum than the SPP, so SPPs can not be directly optically excited due to this momentum mismatch. This is due to the strong coupling between surface charges and light, which demands that the SPP has increased momentum because the light field has to also move the electrons on the surface. The SPP is bounded by the photon line at low k and the surface plasma frequency $\omega_{sp} = \frac{\omega_p}{\sqrt{\epsilon_d + 1}}$, where ω_p is the plasma frequency of the metal, at high ω. [103]

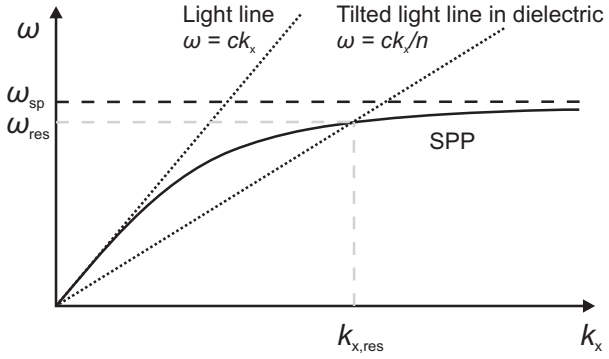

FIGURE 2.6 The dispersion relation of a surface plasmon polariton on a metal surface. The light line is plotted for vacuum. For excitation of a SPP using a prism (Kretschmann or Otto configurations), a tilted light line is drawn where n is the refractive index of the prism. This line intersects the SPP dispersion curve at resonant ω and k_x, resulting in SPP excitation. [103, 155]

The propagation length of the SPP L_{spp} is also dependent on the imaginary

parts of the dielectric functions, as given by

$$L_{SPP} = \frac{1}{2\mathrm{Im}(k_{SPP})} = \frac{c}{\omega}\frac{|\mathrm{Re}(\epsilon_m)|^{\frac{1}{2}}(|\mathrm{Re}(\epsilon_m)| - \epsilon_d)^{\frac{3}{2}}}{\epsilon_d^{\frac{3}{2}}\mathrm{Im}(\epsilon_m)}. \tag{2.2}$$

Over this length the electric field of the SPP is damped by 1/e, and the distance at 633 nm wavelength is for silver approximately 60 µm and for gold 10 µm. Due to this, SPPs are not suitable for signal transfer for distances any larger than what can fit in a microchip. [103]

The wavelength of a SPP depends on the dielectric functions of the metal and dielectric:

$$\lambda_{SPP} = \frac{2\pi}{\mathrm{Re}(k_{SPP})} \approx \sqrt{\frac{\mathrm{Re}(\epsilon_m) + \epsilon_d}{\mathrm{Re}(\epsilon_m)\epsilon_d}}\lambda, \tag{2.3}$$

where λ is the wavelength of light used for excitation.

2.3.2 Excitation of surface plasmons

SPPs can only be excited when the momentum (directly proportional to wavenumber k) of the incoming photon matches the momentum of the plasmon at the same energy. On a flat metal interface they cannot be excited by incoming far-field light, because the wavevector k_x of the plasmon is always larger than that of light in free space. The reason for the increased momentum is the strong coupling between light and surface charges.

The missing momentum can be provided with surface roughness or a grating, additionally the light cone can cross the SPP dispersion curve with evanescent waves, resulting in the excitation of the SPP. The SPP can be converted to far-field light by a scattering center on the metal, and similarly a SPP can be generated (inefficiently) simply through any impurity or uneven surface feature that would scatter the SPP.

In addition to scattering, the energy of a SPP can be expended in exciting a molecule directly like far-field light does. This weak coupling can be used e.g. to image plasmons by the fluorescence of molecules or to enhance fluorescence with plasmons [78]. Similarly as with a molecule, coupling also occurs between metal structures in close contact [75]. SERS relies on these coupling effects with molecules, enhancing the Raman cross-section by a factor of 10^6 if the molecule is next to a roughened metal surface. [129]

If this molecular excitation by SPP does not relax by fluorescence, but instead couples immediately back to the plasmon, the coupling is said to be strong. This leads to SPP-molecule hybrid modes or polaritons between molecular excitations and surface plasmons [51]. The polariton states (P- and P+) manifest themselves in the plasmon dispersion as a Rabi split, that can be several hundred meV in magni-

tude. The energy of the coupled mode oscillates virtually between the molecule and the plasmon, known as Rabi oscillations [135].

The metals most suitable for exciting a surface plasmon resonance have a small real part of the refractive index n and a large imaginary part (extinction coefficient) κ. For real and imaginary parts of the dielectric function, these values are the opposite (relatively high but negative $\mathrm{Re}(\epsilon_m)$ and low $\mathrm{Im}(\epsilon_m)$). In these cases the resonance dip in terms of angle and wavelength is the most localized. [79]

Localized surface plasmon resonance

In a nanoscale metal particle, the oscillation of free electrons can encompass the whole particle instead of just the surface. This back-and-forth oscillation produces SPP modes that can be directly excited by optical means. These modes are resonant in nature and are visible as optical absorption without dispersion. This localized surface plasmon resonance (LSPR) depends on the size, shape and dielectric function of the particle. Non-spherical metal particles can thus have several possible resonances in the same particle, as the oscillation can happen in different directions. [103]

Kretschmann configuration

To couple the momenta and energy of far-field photons and surface plasmons a total internal reflection (TIR) setup can be used. When a photon comes from a high refractive index material to a low index material at a high enough angle relative to the interface normal, the photon does not pass the interface and is reflected. An evanescent wave is also produced at the interface (frustrated TIR), which can couple to a metal surface at certain combinations of incoming angle and photon energy. In the Otto configuration (Fig. 2.7c), this is done with a gap of low-index material (usually air) which is situated between the prism and metal.

In the Kretschmann configuration (Fig. 2.7a) a thin layer of metal is situated on the high-index material, and a the evanescent wave penetrates through the metal to produce a SPP on the far interface of the metal [103]. In this case, the surface plasmon resonance can be observed by measuring the spectrum of light reflected from the interface, which will show angle-dependent dips corresponding to the resonance. Corresponding emission can be seen on the other side, which is caused by the scattering of SPPs from defects on the metal surface.

When trying to measure SPPs with the Kretschmann configuration, it is relevant to also consider other signals present in the measurement. The evanescent wave also interacts with materials present on the TIR interface, and this can be used to get useful absorption spectra of a very small amount of material (less than 100 nm from the interface). TIR absorption measurements as such do not necessarily involve any plasmons, unless enhancement by them is needed. [9]

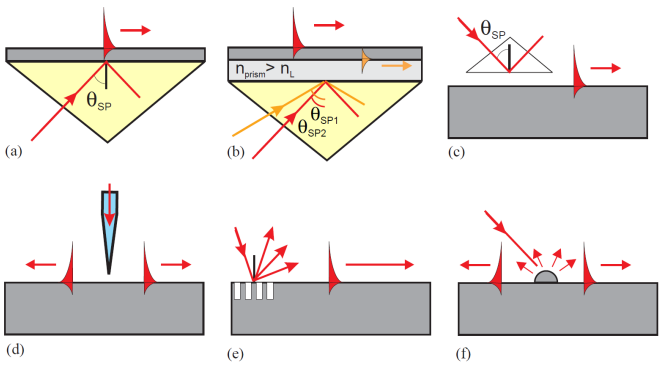

FIGURE 2.7 Excitation methods for surface plasmon polaritons. Methods shown are the Kretschmann geometry in a) one layer and b) two layers, c) Otto geometry, d) excitation with sharpened optical fiber (SNOM), e) diffraction with a grating and f) scattering on surface features. Republished with permission of Elsevier, from [155].

Grating coupler

SPPs can also be excited by using a grating coupler (Fig. 2.7e). In this approach the periodic metal structure (grooves or ridges) redirects the momentum of the photon along the surface. The situation is similar to a transmissive diffraction grating, but in this case a reflective grating directs one diffractive order of the beam along the metal surface. [113]

In such a grating SPPs are excited when the wave vector component k_x of the incident light ($k = \frac{\omega}{c}$) along the surface matches the wave vector of the SPP:

$$k_x = \frac{\omega}{c}\sin\Theta \pm n\frac{2\pi}{a} = k_{SPP}, \tag{2.4}$$

where Θ is the angle of incidence, n is an integer (order) and a is the distance between successive grooves. [113]

Scanning near-field optical microscopy

A crucial tool for imaging SPPs on a metal-dielectric interface is the scanning near-field optical microscope (SNOM), which uses evanescent waves to examine optical properties below the far-field resolution limit. To achieve this, an aperture smaller than the wavelength of light as shown in Fig. 2.7d is used, through which only an evanescent wave can pass. Alternatively a nanoscale scattering center, usually a sharp metal tip, can be used to enhance the optical signal in the vicinity of the tip or to image SPPs on a metal surface. Such tips suitable for near-field imaging are scanned across a surface similarly as in atomic force microscopy (AFM). This enables optical imaging at a resolution of tens of nanometers in the surface plane with a simultaneous measurement of topography. Here, the principles of SNOM operation are detailed as a background to experiments in Section 4.2.

In scanning probe microscopy (SPM), the probe is typically controlled electrically with piezoelectric elements, scanning the tip line by line in a xy-plane and controlling the z-axis height based on the interactions of the tip with the surface. Scanning can be done in contact mode, in which the tip deflection results directly from contact to the sample, which is often damaging to the sample or the tip. In dynamic contact mode (also called tapping mode or intermittent contact mode) the tip is tapped back and forth on the sample, usually perpendicular to the surface. Contact forces cause the amplitude of this vibration to change, which is measured. The forced vibration of the tip can also be done parallel to the surface, which is referred to as shear force mode.

Equivalently, the tip can be stationary while the sample is moved. As the piezos have a range in the scale of tens of micrometers, larger movements are usually done either with electric motors or by using the piezos in the stick-and-slip method with repetitive pulses.

Detecting topography in a SNOM is achieved similarly as in an atomic force microscope, usually relying on one of two schemes. The deflection of the tip can be detected with a laser beam reflected off the tip, which is then measured by a set of photodiodes. The signal due to deflection is fed to a feedback loop to control the height of the probe. This method is used by most dedicated AFMs.

In a SNOM setup, such a laser might interfere with the optical measurement. To avoid this, a piezoelectric signal can be used to measure the probe-sample interaction. A tuning fork attached to the probe is needed for this, and it is electrically driven close to its resonance frequency. The frequency of the fork oscillation changes if the probe is in contact with the surface, and a piezoelectric signal is generated due to mechanical stress [116].

In this way, both the driving signal for the vibration and the detection are done with the same electrodes. The deviation in phase between the excitation and the detection in particular indicates the frequency shift, and it is measured with a lock-in amplifier and used in a feedback loop controlling the z-axis height. Additionally the amplitude of the tuning fork vibration is measured for a second feedback loop, controlling the driving signal to keep the amplitude of the mechanical vibration constant. [116]

To achieve an optical signal below the diffraction limit in SNOM, a subwavelength aperture or a nanoscale scattering center is needed. These can be provided by either apertured tips or apertureless sharp tips. Additionally frustrated total internal reflection can be used to excite near-field modes to be collected with a coated or uncoated fiber as seen in Fig. 2.8c, also known as scanning tunneling optical microscopy [114].

In addition to imaging, spectroscopy can be done with SNOM systems, including Raman and fluorescence spectroscopy with laser excitation. Apertured collection or excitation typically has long collection times, but apertureless spectroscopy can have increased spatial resolution from the tip without sacrificing intensity. This

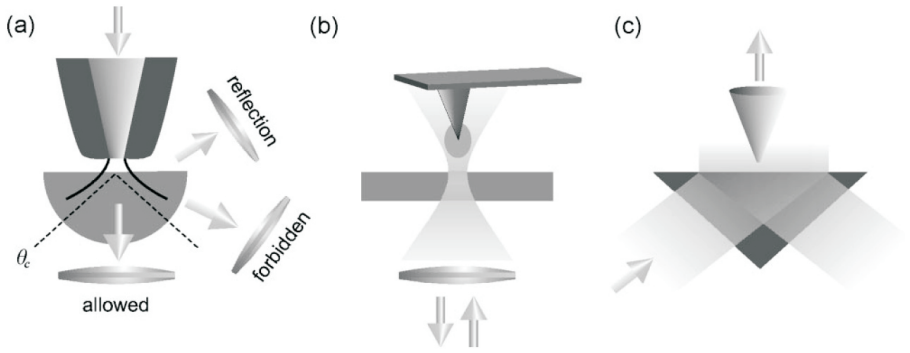

FIGURE 2.8 Different types of scanning near-field optical microscopy. a) Apertured SNOM with excitation through the probe with different far-field detection modes. Collection can also be done through the fiber probe, if the sample either emits light or is illuminated in the far-field. b) Apertureless SNOM, which is based on the probe acting as a scattering center. c) Scanning tunneling optical microscope based on total internal reflection, where the tip acts as a collection device. Reprinted from [55], with the permission of AIP Publishing.

is done for example in tip-enhanced Raman spectroscopy by using a sharp SNOM metal probe and laser excitation focused by a confocal microscope [10].

SNOM operation can be done with apertureless tips in scattering mode, as in Figure 2.8b, where both the excitation and collection of light are done in far-field. In this mode the tip acts as a scattering center, and it can be an optical fiber completely coated with metal or a silicon cantilevered probe depending on the system [55].

Apertured probes, like the one visible in Figure 2.9a, are metal-coated except for an opening at the tip. In this mode the fiber can be used for direct excitation of the sample with an evanescent wave, if the illumination is done through the fiber, or collection of light to a detector. The optical fiber tips are sharpened either by etching or pulling [114] and apertures can be made with etching or ion milling.

The size of the aperture in practice determines the optical resolution. The number of allowed electromagnetic (EM) modes decreases as the dimensions of the aperture gets smaller, and its diameter needs to be less than third of the excitation wavelength if only an evanescent wave is desired at the tip (Fig. 2.9b). Additionally, the sample distance has to be less than the aperture diameter for subwavelength imaging to be possible.

There is a significant tradeoff between the resolution provided by an apertured SNOM tip and the intensity of light transmitted through it, as the transmission scales as a^4 when a is the aperture diameter. Due to this, a 50 nm aperture is generally the smallest useful probe opening. The detected optical signal can be increased with higher laser input power, but the damage threshold of the metal coating limits this to about 15 mW. [55]

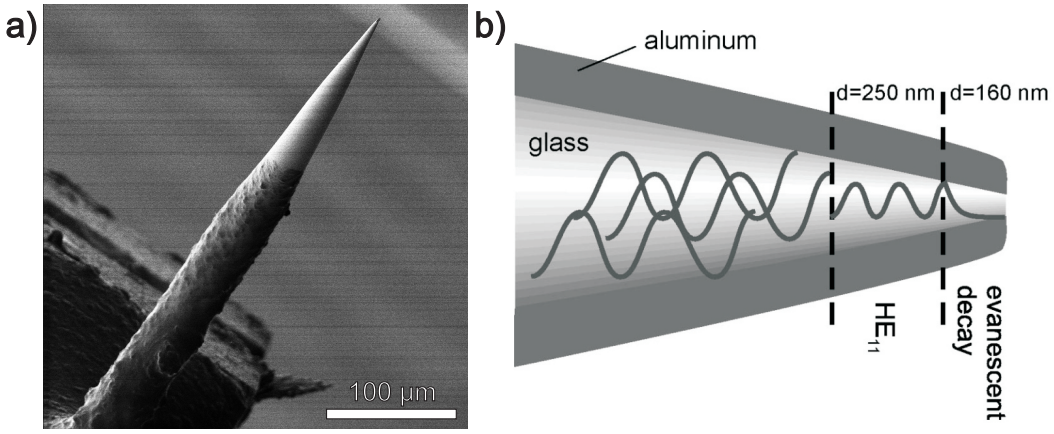

FIGURE 2.9 a) Helium ion microscope image of a SNOM tip. The optical fiber has been sharpened by pulling, coated with 10 nm Cr and 200 nm Au layers and chemically etched to produce a 100 nm aperture. The fiber has been glued to a quartz tuning fork, the end of which is visible on the lower left. Image by the author. b) Schematic for the propagation of optical modes in an aluminum-coated glass optical fiber. The vacuum wavelength of the light is 488 nm. For this wavelength, diameters smaller than 250 nm can only contain the smallest waveguide mode HE_{11}, and at diameters less than 180 nm the field is in evanescent decay and will not continue to propagate in the far field without further interaction. Part b) reprinted from [55] through [103], with the permission of AIP Publishing.

2.3.3 Plasmons in carbon nanostructures

In contrast to plasmons in metals, which have frequencies generally in the visible or near-ultraviolet range, the plasmons supported by graphene lie in the infrared (IR) and terahertz ranges [7]. These optically excitable excitations can be adjusted with the size of the structure and unlike in metals, by an external electric field and by doping. The losses of plasmons in graphene are also lower than in metals. These features make graphene an interesting material for plasmonics, and also in relation to strong coupling, because the coupling can be adjusted by an external voltage [36].

IR plasmons in graphene can also be imaged with scattering-type SNOM. The plasmons have an energy corresponding to a 10 µm wavelength far-field photon, but in graphene on SiO_2 the plasmon wavelength is at the scale of 200 nm, one of the shortest imaged for any material [38].

Localized plasmons in graphene can be found in nanoscale structures, such as ribbons [67] and disks, which can also be stacked [148]. The energies of plasmons in such structures are lower for larger structures, and strong coupling can also be seen when measured with Fourier transform infrared spectroscopy (FTIR), as in Fig. 2.10a. As the energies of the plasmons are low (around 100 meV), suitable transitions are found in vibrational states, not electronic transitions as with metals. In this case the phonons of the substrate hybridize with the plasmon, which can be observed as a Rabi split [162].

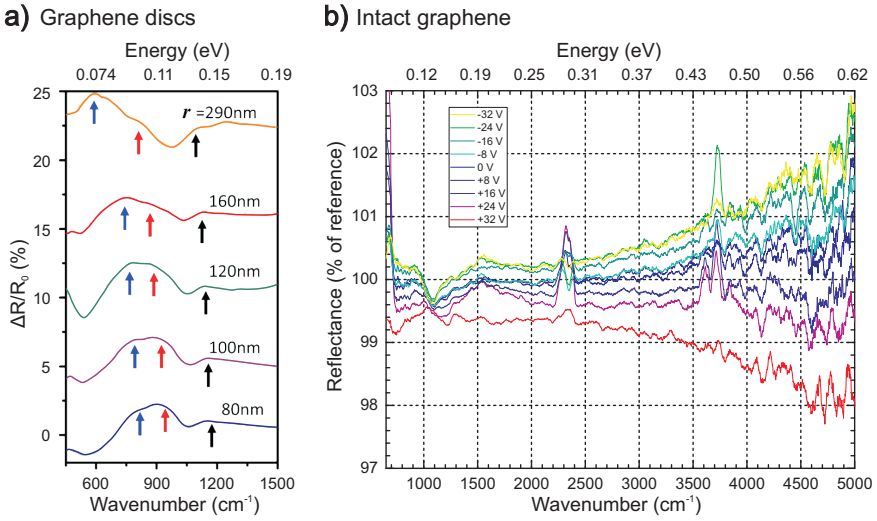

FIGURE 2.10 a) Reflectance spectra of graphene nanodiscs of different radii r made with nanosphere lithography on Si/SiO_2. The plasmon modes, seen as reflectance peaks, are hybridized with substrate phonons, and split branches are highlighted with arrows. The reference R_0 was measured from a bare substrate. Spectra vertically displaced. Reprinted with permission from [162]. Copyright 2014 American Chemical Society. b) FTIR microscope reflectance spectra of a non-milled graphene sheet on Si substrate with 300 nm SiO_2. Gate voltage was applied to graphene relative to the Si substrate, and reflectance is modulated especially at high energy. The reference is a measurement of graphene without applied gate voltage. The most prominent peaks, in addition to random noise, are related to CO_2 (2350 cm^{-1}) and H_2O (around 3700 cm^{-1}) as the measurement was done in ambient conditions.

Using an external electric field (gate voltage) changes the charge carrier concentration, and shifts the energies and intensities of the plasmons [36]. It should also be noted that in addition to plasmons, the IR reflectivity of an intact sheet of graphene can be changed with gate voltage as can be seen in Fig. 2.10b. This is caused by the shift in the Fermi level E_F due to gating, which affects interband transitions [142]. Plasmons in graphene are also affected by very high magnetic fields, as the plasmons in disk arrays can be split into bulk and edge modes with applied fields of several teslas [149].

In electron energy loss spectroscopy (EELS) plasmons can be measured by direct excitation of electrons. EELS works by exposing a sample to a beam of electrons with a narrow range of energies, and measuring the amount of energy loss due to inelastic scattering. Direct electron excitation can probe bulk plasmons, that can not be optically excited, among other inelastic interactions.

For SWCNTs, EELS measurements show a π-plasmon between 5 and 10 eV, dependent on angle of excitation, and a $\pi + \sigma$ plasmon at 25 eV [74]. There has been relatively little research about optically active plasmonic excitations in carbon nanotubes, and previous research has concentrated mostly on theoretical work

and studies of single CNTs combined with plasmonic nanoparticles. There have however recently been some reports of localized plasmon resonance in both SWCNTs [125] and MWCNTs [96]. CNT films are also known to support surface plasmons in the terahertz range [144], which is attributed to a mode parallel to the tube axis. This localized surface plasmon mode has an energy depending on tube length, and it is visible in both metallic and doped semiconducting SWCNTs [158].

There have also been theoretical studies of an another plasmon mode in highly doped tubes, equivalent to those in graphene ribbons when the tube diameter is sufficiently large [1]. Unlike the THz surface plasmon resonance parallel to the bundle, this mode is transverse to it. These intraband plasmons could occur on infrared and visible wavelengths [119]. There have been some experimental studies supporting this with electrochemically doped tubes, but attributing this specifically to a localized surface plasmon resonance in bundles [61]. More generally, the optical absorption of chirality-controlled SWCNTs can indeed be adjusted by electrochemical doping [150].

Additionally, scattering-type SNOM has been used to image plasmons in single and bundled metallic SWCNTs. These Luttinger-liquid plasmons are excited in one-dimensional Dirac electrons of the SWCNTs, and behave differently from classical plasmons. [124]

Conductive polymers

For surface plasmon polaritons to occur, a negative real permittivity is needed that is generally provided by the high carrier mobility in a metallic material. However, semiconducting materials can support surface plasmons in IR if they are doped or in resonance. Metal oxide semiconductors, silicon carbide and semiconductors with elements of groups III-V (e.g. GaAs, GaP, GaN) have been considered for plasmonics in the near-infrared when heavily doped. [146]

Even though conductive polymers can have similar carrier mobilities, studies about SPPs in them are close to nonexistent. There is one example of anomalous transmission in a sub-wavelength aperture array in a conductive polymer, which is claimed to be due to a SPP resonance at about 0.2 THz [90]. In conductive polymers with a moderate conduction electron density, any possible plasmonic excitations are necessarily limited to IR or terahertz energy ranges due to the low plasmon frequency [146].

Chapter 3

Synthesis

3.1 Graphene

Generally single layers of crystals are very difficult to produce as such. Because crystal growth requires relatively high temperatures, 1D and 2D objects in macroscopic scale cannot be reliably grown due to thermal fluctuations, and 3D structures with higher stability are produced instead. Producing 2D crystals is still possible, but it has to be done either by cleaving an existing crystal or growing an additional layer on a suitable crystal substrate. [45]

The first approach can be applied to graphene by cleaving graphite crystals. The "scotch-tape method" can be used to produce high quality graphene flakes up to a square millimeter by repeatedly dividing graphite using the glue on the tape. As this method is slow, expensive and difficult to control, it is only used for basic research. The same approach can be done on an industrial scale by using an ultrasonic processor to disperse submicrometer flakes from graphite to a suspension. This approach can be aided by using chemically intercalated graphite, and surfactants can be used to keep the flakes suspended. [45]

The second method of additive synthesis is used for producing graphene layers on a larger scale on suitable substrates. Chemical vapor deposition (CVD) can be used to create layers at a high temperature with hydrocarbons as the carbon source. Copper is the most common growing substrate, producing a single layer with highest reliability. Nickel has also been used as a substrate. A typical process on Cu foil has a hydrogen gas pretreatment, and for graphene growth a pressure of 500 mTorr (67 Pa) in the CVD chamber with 35 sccm methane flow and a temperature of 1000 °C [81]. As an additional method, a silicon carbide surface can be annealed at 1000–1500 °C in either vacuum or noble gas, decomposing SiC and leaving behind graphene layers on the surface. [25]

Graphene can be modified with different functional groups to change its surface chemistry and electrical properties. For applications in electronic devices, modification of the band gap in graphene is essential. For example, hydrogenization

results in graphane, which behaves as an insulator [46]. Oxidation can be done with chemical or thermal methods, producing a 2D material with a bandgap that can be controlled with the level of oxidation [30]. Photocatalytic reduction of graphene oxide can also be done in the presence of oxygen with ultraviolet light, enabling direct patterning, and higher resolution can be achieved by using two-photon oxidation with a high-power visible laser spot [5].

3.2 Carbon nanotubes

Production methods of carbon nanotubes can be divided into physical and chemical methods. In physical synthesis, high-energy methods are used to release carbon atoms from a carbon feedstock. The first of these to be discovered was arc discharge synthesis, which initially grew MWCNTs on a graphite anode in argon [62], and it involves temperatures of above 1700 °C produced by the electrical discharge. Laser ablation relies on a similar process, where a graphite target is heated with a pulsed laser in an inert gas, and the vaporized carbon condenses on cooler surfaces of the reactor.

In contrast, the chemical methods rely on the catalytic decomposition of molecular precursors [94]. Carbon fibers have been grown on metal catalysts for more than a century, and these methods are based on this [95]. Generally the catalysts are transition metal nanoparticles, on which the tubes grow. Chemical methods can be further divided into aerosol synthesis, where the metal particles are formed during synthesis and the entire process takes place in the gas phase, and catalytic chemical vapor deposition (CVD).

In catalytic CVD, the catalyst particles are pre-made and supported on a surface. Currently this is the most common method for SWCNT growth, because it is technically simpler than the alternatives, and there are a large number of parameters that can be used to control the growth process. Typical metals used for catalysis are iron, nickel and cobalt, and the particle can either be pinned on the surface (root growth) or be lifted (tip growth). In either case, there are typically catalyst impurities stuck on the produced tube. The carbon precursor is often a small hydrocarbon. Carbon monoxide can also be used, like in the high-pressure CO method. Typical temperatures for chemical synthesis methods are between 500 °C and 850 °C. [133]

Like graphene, CNTs can be chemically functionalized, in addition to adsorption-based non-covalent modification. The highest reactivity in the tubes is found in defect sites or on the end caps due to curvature and associated higher strain. Starting from these sites, oxidation with acids is often the first step in modification. A wide variation of different functional groups or other additions have been realized, from carboxylic acids and amines to cycloaddition and metal nanoparticles. The inner space of a CNT can also be filled to achieve linear arrays of substances, e.g. fullerenes, organic dyes, polymers or inorganic salts. [69]

In addition to using synthesis methods that favor certain chiralities, SWCNTs can be sorted after synthesis. These methods are done in suspension and include selective covalent sidewall functionalization, wrapping with non-covalent surfactants, interaction with solvents, electrophoretic separation and selective destruction. [59]

One of the most successful methods for chirality sorting has been density gradient ultracentrifugation (DGU), which uses a mix of surfactants in aqueous solution. The surfactants are non-covalently wrapped around the SWCNTs, and they have different affinities to different chiralities [59]. As the surfactants have different densities, centrifugation results in different layers as seen in Figure 3.1, where single tubes are sorted by diameter and chirality. Electronic properties also affect the interaction between the tube and surfactant, with semiconducting tubes having generally a higher affinity to surfactants [151]. Usually the surfactants are long hydrocarbons with a non-polar end (often with an aromatic ring) attached to the tube and a polar end away from the tube in the polar solvent. Common ones are sodium dodecyl sulfate, sodium dodecyl benzenesulfate, sodium cholate (SC) and sodium deoxycholate (DOC). Single-strand DNA has also been used as as a surfactant for chirality control in DGU [4]. An initial density gradient is needed for DGU, e.g. by layering aqueous dilutions of iodixanol in the centrifugation tube. Additionally, it is also possible to separate left- and righthanded SWCNT enantiomers using DGU when using chiral surfactants such as SC [86].

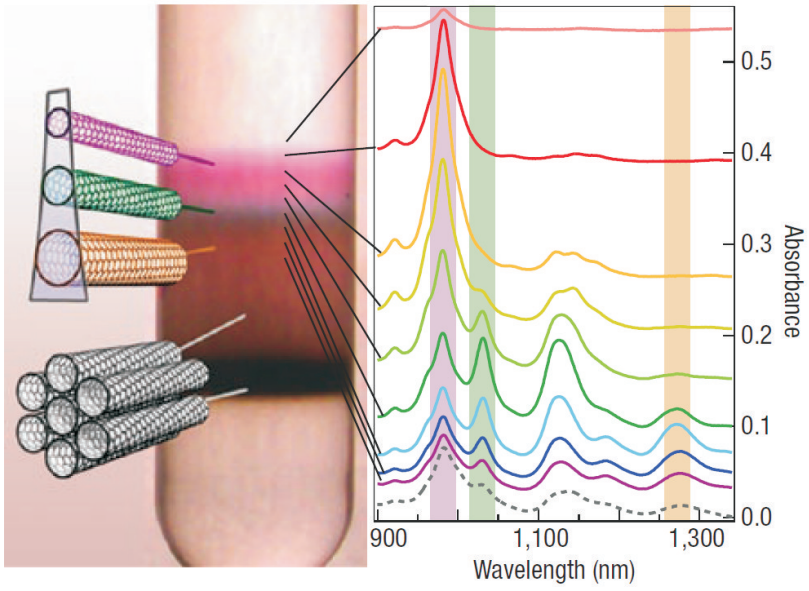

FIGURE 3.1 A centrifuge tube with SWCNTs encapsulated with sodium cholate in water following density gradient ultracentrifugation is displayed on the left. On the right, absorption spectra corresponding to different layers extracted from the tube are shown, and the illustration on the right refers to separation by diameter (and bundling status) of SWCNTs to different layers. Reprinted by permission from Macmillan Publishers Ltd: Nature Nanotechnology [59], copyright 2008.

Instead of ultracentrifugation, the same surfactants can be used to separate SWCNTs with chromatography. In this method, a solution with particles is loaded to a column filled with a dextran-based adsorbent gel, and is eluted through this gel bed. Based on the size of the particle, they travel through the gel at different speeds, enabling this size-exclusion chromatography. Large particles pass through quickly since they cannot enter the pores in the gel, while small ones are more likely to be adsorbed and trapped in the pores.

When this method is applied to separating SWCNTs, a mixture of surfactants with different affinities based on diameter (DOC) and chiral angle (SC) can be used. Based on differing amounts of these surfactants, interactions between the wrapped tubes and the gel are based on the properties of the tubes. Rather than large particle size, a higher affinity for adsorption to the gel slows down certain tubes. Chromatography can also be done by repeatedly processing the same sample with different surfactant mixtures and material with fast or slow elution, enabling the selection of precise single chirality SWCNTs of over 90 % purity in milligram quantities. [151]

3.3 Conductive polymers

The fabrication of conductive polymers is generally done by chemical polymerization from monomers. In the case of PEDOT the monomer is 3,4-ethylene dioxythiophene. There are several chemical pathways to synthesizing the monomer, e.g. synthesis from oxalic acid ester and thio-diacetic acid ester or a transesterification process [33]. The dopant PSS is prepared by the sulfonation of polystyrene. Polymerized PEDOT is insoluble, so a dispersion of PEDOT:PSS can be prepared by oxidative polymerization of the monomer in the presence of PSS in water [85]. This dispersion can be applied as a thin film by e.g. spin- or spray-coating and baked to remove water and any other solvents. Polymerization can also be done in situ after film application. [33]

Part II

Experiments

Chapter 4

Surface plasmon gating of carbon nanotubes

The electrical conductivity of a carbon nanotube is usually modulated by means of an applied electric field, which in practise means that a gate voltage is applied to a nearby terminal that is insulated from the channel. For CNTs modulation can also be done with optical excitation and by controlling the chemical environment of the tube. Using surface plasmon polaritons to control the conductivity of a CNT has a similar principle than excitation with far-field light, but it had not been previously demonstrated before the research described in this chapter. These results are also published in article A.I.

To understand better the effects of near-field optical excitation to the electrical transport properties of carbon nanotubes , CNT FETs of a different design were also excited locally using a SNOM tip. This provided a way to probe the location of spots sensitive to optical excitation at a subwavelength scale. These previously unpublished experiments are reported in Section 4.2.

4.1 Gating with SPPs

The approach used for the Kretschmann configuration utilized a CNT field effect transistor with a silver back gate. The CNT was insulated from it with a thin polymer film, and the SPPs were excited on the metal-polymer interface using a total internal reflection configuration. Palladium was used for electrode contacts because it is resistant to oxidation, it wets the CNT surface well relative to other metals and its high work function results in a relatively low Schottky barrier (Fermi level aligned with the CNT), delivering more current in the on-state [64].

4.1.1 Sample fabrication

The substrate used for the experiments was a 1 cm^2 glass slide which was cleaned with oxygen plasma in a reactive ion etcher (RIE). The metal needed for supporting the SPPs was a 63 nm thick and 1 mm wide silver strip, which was deposited with electron beam evaporation using a mechanical mask. To ensure SPP propagation with low losses, a smooth silver film is needed. This can be achieved either by having very small crystallites produced at a very low evaporation rate (0.05 nm/s) [128] or alternatively large smooth grains with very fast evaporation. When evaporating reactive metals (e.g. Ti and Cr) at fast rates (before the sample is exposed), residual gases in the chamber can be reacted with and the vacuum improved. For Ag the residual gases are a problem, as they can stop grain growth, and fast evaporation also limits exposure to the gases [91]. For these experiments, a high rate was used (12 nm/s), and the resulting large grain size in relation to films with slow evaporation was confirmed with AFM.

As a dielectric layer and for protecting the silver strip a 50 nm thick layer of the SU-8 negative photoresist (Microchem) was spin-coated immediately after Ag evaporation. The resist was then prebaked (95 °C), exposed with UV light, post-baked and developed in acetone. The layer is unusually thin for SU-8, and for this the SU-8 2025 resist had to be diluted at 1 part in 23 parts of cyclopentanone. A small part of the Ag strip (Fig. 4.1a) was left unexposed to leave space for the gate electrical connection.

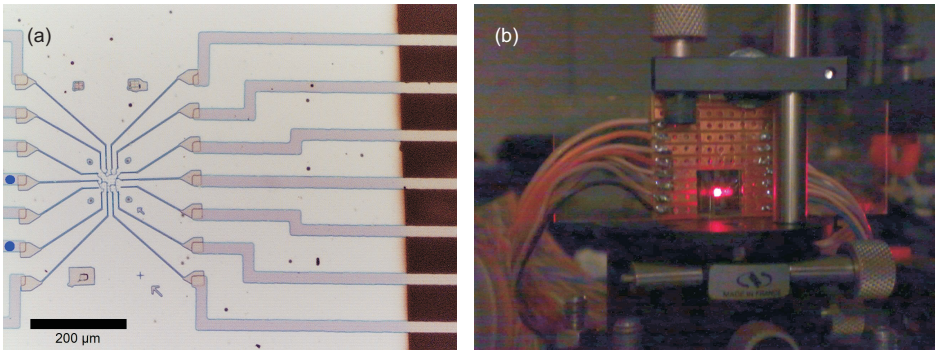

FIGURE 4.1 a) Optical microscope image of the CNT FET structure. Electrical measurements and the AFM image shown in this Chapter are from the device attached to the electrodes marked with blue circles. b) Measurement in progress, the sample was illuminated from the back from the back through a hemicylindrical prism using a 633 nm HeNe laser.

Ultraviolet photolithography was used to produce large palladium electrodes with bonding pads outside the silver strip. A positive photoresist, AZ1514H, was spin-coated and baked. The large-scale electrode design was exposed through a photomask with chromium on glass, which was prepared in advance with electron beam lithography (EBL) and wet etching. After development, a protective 36 nm

thick Al_2O_3 film was evaporated with an e-beam evaporator on the exposed SU-8 surface. To ensure a continuous film, the evaporation was done at an angle while rotating the sample. A 25 nm Pd layer was evaporated in the same vacuum after this perpendicularly. These electrodes were 20 µm wide, extending nearly 5 mm across from from contact pads on glass to on top of the silver strip as seen in Fig. 4.1a.

For transistor operation, oxides like SiO_2 or HfO_2 would be more suitable as the dielectric layer, but the processes used for those (CVD or atomic layer deposition) are often not compatible with silver, causing it to oxidize. SU-8 was used primarily due to this, and also because applying it with spin coating produces a very flat surface. Flatness is preferable for further processing, in particular for imaging deposited SWCNTs with AFM as seen in Fig. 4.2. As a downside, the durability of a layer as thin as 50 nm of SU-8 is poor. Mechanically, this layer often stripped off with later lithography processing, and electrically the gate voltage had to be restricted below 0.5 V due to electrical breakthrough of the polymer layer at higher voltages. The Al_2O_3 layer below the first Pd pattern was added to mitigate the gate leakage.

Subsequently, smaller electrodes and alignment marks were produced with EBL. A dual layer of P(MMA-MAA) EL11 (500 nm) and 950 PMMA A2 (70 nm) resists were spin-coated, baked and the pattern was exposed with a Raith eLine 50 EBL system. 70 nm of palladium was evaporated after development to produce the structure, contacting the previous Pd layer.

The SWCNTs, synthesized with CVD, were purchased from Nanocyl S.A. (Nanocyl 1100). The powder was suspended to (1,2)-dichloroethane by ultrasonication prior to the deposition, with the suspension having a SWCNT concentration of 1/300000 by mass. The suspension was spin-coated on the sample surface on top of the SU-8 film, resulting in single tubes and bundles well separated from each other. It is also possible to spread SWCNTs with surfactants from a water solution, which produces separated single tubes with a higher reliability. However, the surfactants can alter the electrical properties of the transistors, if their removal is not complete.

The positions of the SWCNTs were imaged with AFM inside the central alignment marker grid. Using the markers as reference points, the final electrode structure was designed based on the images. EBL was used similarly as before to produce 84 nm thick palladium electrodes extending from the previous Pd layer to the individual CNTs. These are visible as the smallest electrodes in among the alignment grid structures in Fig. 4.1a. An AFM image of a single device is seen in Fig. 4.2.

Locating the SWCNTs with AFM is slow, and in our case there needed to be 25 of 10 µm by 10 µm images to cover the marker grid, taking 5–10 minutes each. Recently, an alternative method has been developed for making the CNTs visible in dark-field optical microscopy, speeding up the imaging process. This method relies on the crystallization of an aromatic organic acid seeded by graphitic carbon. [156]

The final glass square with the CNT FET (Fig. 4.2) was attached with index-

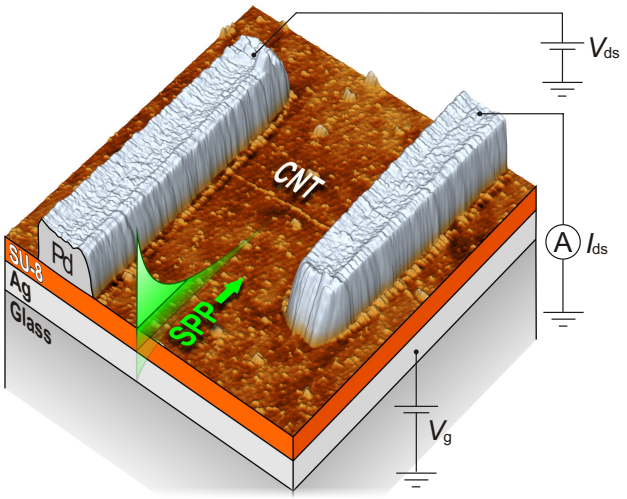

FIGURE 4.2 Schematic of a carbon nanotube field effect transistor that can be gated with surface plasmon polaritons. The excitation is done through the glass substrate and the SPPs travel on the interface between the silver layer and the SU-8 dielectric. The edges of the AFM image are 2.5 µm, the CNT channel is 1 µm long and the height of the palladium electrode is 84 nm. Adapted with permission from article A.I.

matching oil on to a glass microscope slide, which had copper contact pads epoxied on. These pads were connected with aluminum wire by ultrasonic bonding to the palladium electrode pads and the silver back gate on the sample (Fig. 4.1b). This stage was attached to the hemicylindrical glass prism on the Kretschmann configuration with the same index-matching oil.

4.1.2 SPP excitation

Using the Kretschmann configuration as seen in Fig. 4.3, SPPs were excited on the interface between the silver strip and the SU-8. The CNT was at a distance of 50 nm from this layer. White light excitation was done using a 220 W tungsten-halogen lamp. The beam was collimated with two slits, and a polarizer was used to control the SPP excitation. The total power density when using white light was measured to be 7 mW/cm^2, of which about 40 % are visible in the spectrum in Fig. 4.4 due to the limited sensitivity of the silicon-based photodetector in the IR range. The excitation angle was used to tune the energy of the excited SPPs. When measuring with white light, reflection spectra were used to measure the SPP resonance, seen as dips in reflection in Fig. 4.4.

Alternatively, a higher intensity could be achieved by using a 10 mW HeNe-laser at 633 nm. On the prism, the incident power density was 700 mW/cm^2, which was estimated to produce a 110 mW/cm^2 power density as SPPs on the silver surface. With the laser, the correct angle for SPP excitation (62°) was found by using emission from scattered SPPs.

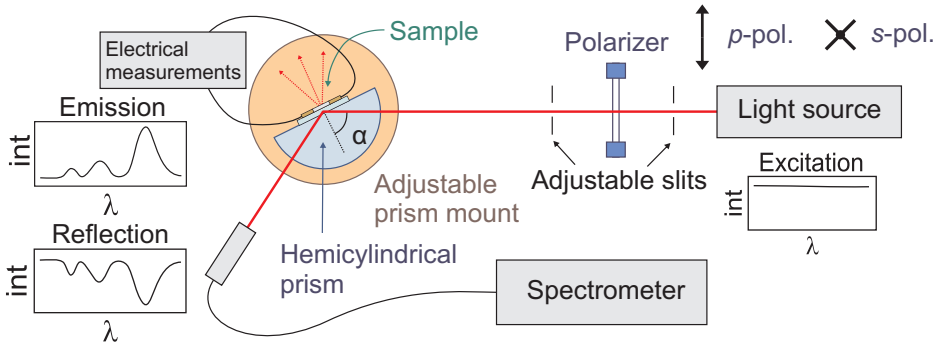

FIGURE 4.3 The measurement setup. The SPPs are excited on the silver film in the Kretschmann configuration while the electric response of the CNT FET is measured. The *p*-polarized light is parallel to the plane of incidence (defined by the incoming and reflected beams), and the *s*-polarization is perpendicular to it. The refractive index of the prism is n = 1.52, resulting in a TIR angle of $\alpha \approx 41°$. Adapted with permission from article A.I.

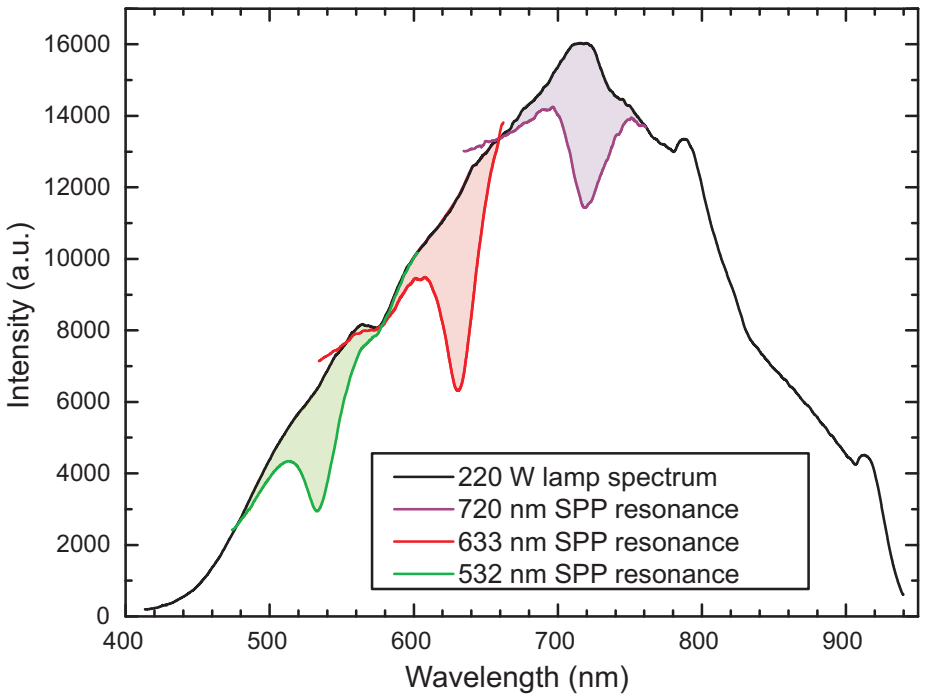

FIGURE 4.4 Optical spectrum of the tungsten-halogen lamp used for white light excitation. Reflection dips are plotted that result from SPP resonance on the silver strip of the sample. The excitation angle (from sample normal) of 55.5° corresponds to far the field wavelength 720 nm (energy 1.72 eV), 62° to 633 nm (1.96 eV) and 79.5° to 532 nm (2.33 eV). The shaded area above the dip represents the approximate intensity of the excited SPPs.

4.1.3 Results

The CNT FETs with Pd electrodes had a *p*-type response with the channel being open at negative gate voltage. In a CNT FET with a channel length of 1 µm (Fig. 4.2), effects of the SPP excitation on the electrical properties were evident. There is a clear shift in the effective gate voltage (equivalent to -0.4 V) as seen in Fig. 4.5. Only the polarization of the incident laser was changed between these measurements.

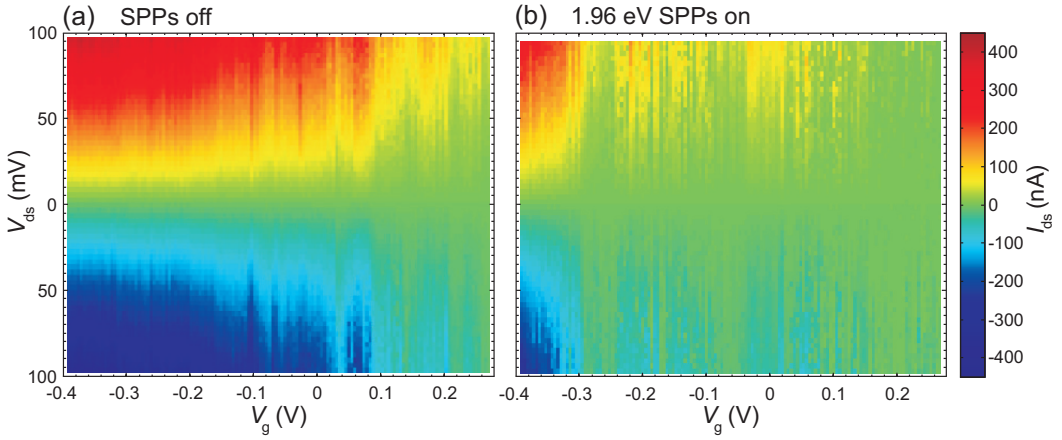

FIGURE 4.5 The drain-source current of the CNT FET as a function of the gate voltage V_g and the drain-source voltage V_{ds}. A 633 nm laser is incident on the sample in both measurements. In a) the SPPs are switched off, *s*-polarized light is used. In b) the SPPs are switched on with *p*-polarized light. Adapted with permission from article A.I.

SPP excitation was controlled with the polarization of incoming light. 633 nm laser exposure at *s*-polarization does not excite SPPs, and this does not have a measurable effect on the electrical response of the CNT FET, as seen in Fig. 4.6. The current in the channel decreases relatively slowly when the SPP excitation is turned on, as also visible in Fig. 4.6, and it recovers at a slightly slower rate. Exponential functions for time dependence are used in the figure, and they give a channel current of I_0^{des} = 14.93±0.12 nA as a low point for extended excitation and I_0^{ads} = 44.06±0.06 nA as a high point after recovery. The corresponding exponential time constants are 131±3 s and 343±3 s, respectively.

White light excitation with SPP resonances at 1.7 eV and 2.3 eV tuned by the incident angle had a minor response compared to the laser measurement. At higher photon energy, the effect was slightly more visible.

4.2 Gating with SNOM

The CNT FETs used for experiments using SNOM excitation were in many ways similar to those in detailed in Section 4.1, but they were produced on a more conventional substrate, namely highly doped silicon with a 300 nm SiO_2 oxide layer. In

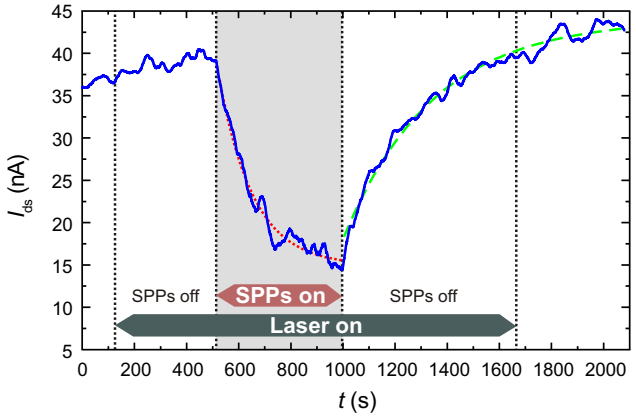

FIGURE 4.6 Time dependence of the drain-source current in the CNT FET in response to laser exposure and SPP excitation. Exponential fits for exposure and recovery are plotted, the voltages were kept constant at V_g = -0.4 V and V_{ds} = 10 mV. Reprinted with permission from article A.I.

this case, large electrodes and an alignment grid were made with palladium using EBL. The SWCNTs were deposited and imaged with AFM as previously described. Based on the images, a second electrode layer with Pd was made to contact the SWCNTs. A typical image with a corresponding design is seen in Fig. 4.10c. The silicon sample was glued to a chip carrier, and aluminum wires were ultrasonically bonded to connect the sample to the carrier. An electrical measurement setup was built to fit the inside of the SNOM scanning stage. In this case the sample cannot be moved due to the stationary electrical contacts, and only the tip (top piezo) can be used for scanning.

4.2.1 Experimental setup

The setup used in this work at the University of Jyväskylä Nanoscience Center has a Nanonics Imaging Multiview 2000 AFM/SNOM head. Far-field microscopes are situated above and below the SPM stage, which is connected to piezo drivers and controllers. As seen in Fig. 4.7a, the scanning stage with the sample is on a stone table with a vibration damping platform. This decreases noise levels especially in the AFM signal. Additionally, the setup is inside a room shielded from EM interference (Faraday cage) to improve the quality of electrical measurements.

Scanning the measurement spot can be done by moving either the tip or the sample with separate piezoelectric actuators. The probe works normally in intermittent mode, and this tapping (the resonant frequency typically 30 kHz for fiber tips) is much faster than the time spent at each measurement pixel (typically 10 ms or 100 Hz). The tuning fork is a quartz crystal with a 32768 Hz resonance frequency before the tip is attached. The Nanonics tips are manufactured by pulling the fiber, and they are attached to a tuning fork assembly, which in turn is connected to the

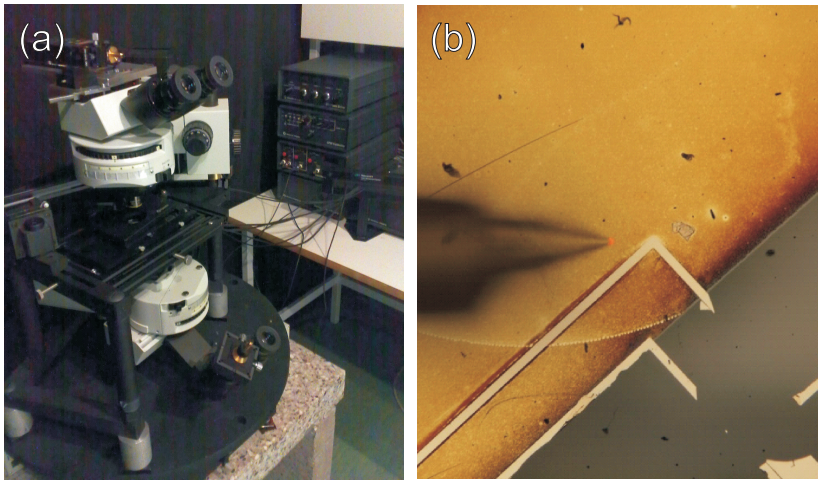

FIGURE 4.7 a) A view of the Nanonics SNOM setup. The scanning stage is between the two optical microscopes on center left, and the controller boxes are on the right. b) An optical image from the top microscope using an objective with 50 times magnification. Laser excitation at 633 nm is fed to the fiber probe in contact, visible as a red spot. The sample has an oxidized and polymer-coated silver strip (top left) on glass and traces of palladium electrodes.

scanning stage by magnets.

For detecting the SNOM signal, an avalanche photodiode is used for photon counting. The silicon diode itself has a panchromatic response (400-1100 nm), which can be limited by using filters. The SNOM signal can be detected from the upper microscope, where the tip is visible as in Fig. 4.7b, the lower microscope or through the fiber.

As an example, a typical SNOM measurement with this setup of a lithographically made silver structure is seen in Fig. 4.8. The excitation is done with a laser via the tip, and the optical intensity is recorded in the far-field. It is highest when the tip is at the edges of the triangle, and this signal practically tells where the coupling with the prism is strongest. Fringes outside the prism are most likely due to leakage of far-field light from the tip, which creates an interference pattern matching the wavelength of the laser. This suggests that the aperture is not a subwavelength one in practice.

In Fig. 4.9 a two-dimensional plasmonic lens fabricated as 60 nm high circular ridges on a gold film is seen as imaged with SNOM with the optical signal collected through the tip. The period of the grating is 605 nm, adjusted to coincide with the wavelength of a SPP on a gold-air interface with the energy of a 633 nm far-field photon. This results in a resonant lens where each ridge contributes in constructive interference of the SPPs, with high intensity at the focal point at the center of the rings [127]. A laser with 633 nm wavelength was used to illuminate the lens in far-field, and the tip was moved during scanning. The resulting SPP interference pattern

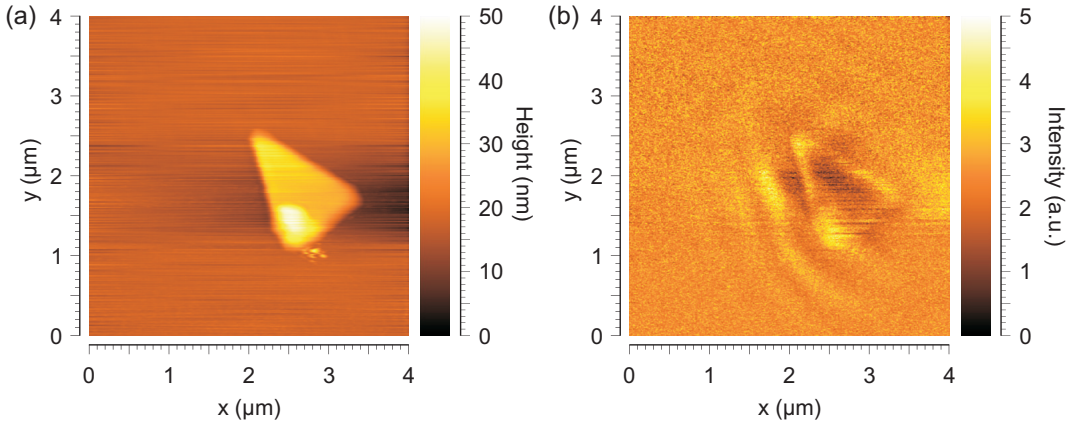

FIGURE 4.8 SNOM measurement of a silver nanoprism with 1 µm sides and 30 nm thickness on Si/ SiO_2. Simultaneously, the a) AFM height and b) optical intensity collected in far-field with a 10x objective were recorded. Laser excitation was done at 514 nm through a coated tip with a 100 nm aperture.

on the flat gold film, matching with the period of the grating, can be seen in the SNOM image. Due to sample movement and piezo drift during scanning, the scale is distorted to be larger than it actually is, especially in the y-direction.

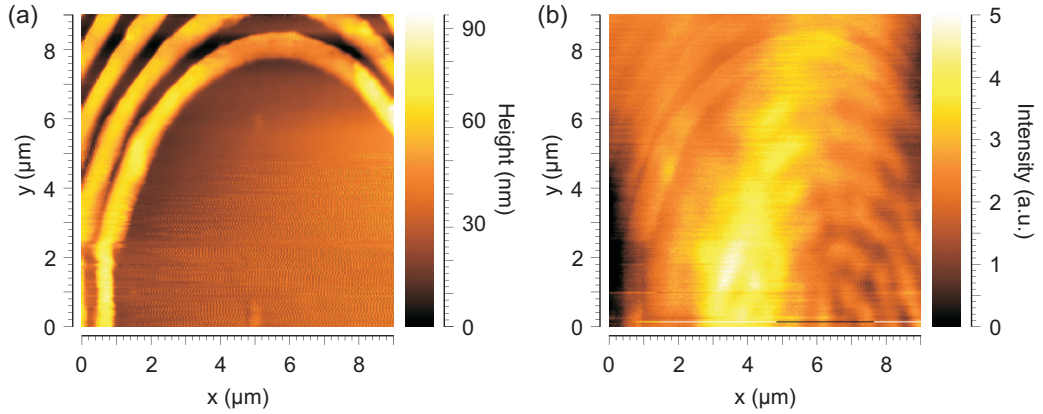

FIGURE 4.9 SNOM measurement of a plasmonic lens made of 60 nm high circular gold rims on a gold film. In a) the AFM height and in b) the optical intensity collected through a tip, coated only with cladding with a 300 nm aperture, are displayed. Laser excitation was done at 633 nm in far-field with a 10x objective.

4.2.2 Results

Using a subwavelength aperture to excite a CNT FET had some effects on its electric response. In Fig. 4.10, there was a current response when the CNT-palladium contacts were excited with a HeNe laser with an excitation power of 10 mW through the SNOM tip. In this particular *p*-type device, at 50 mV source-drain voltage and 0 V gate voltage, the maximum current due to illumination of the contact was 0.75

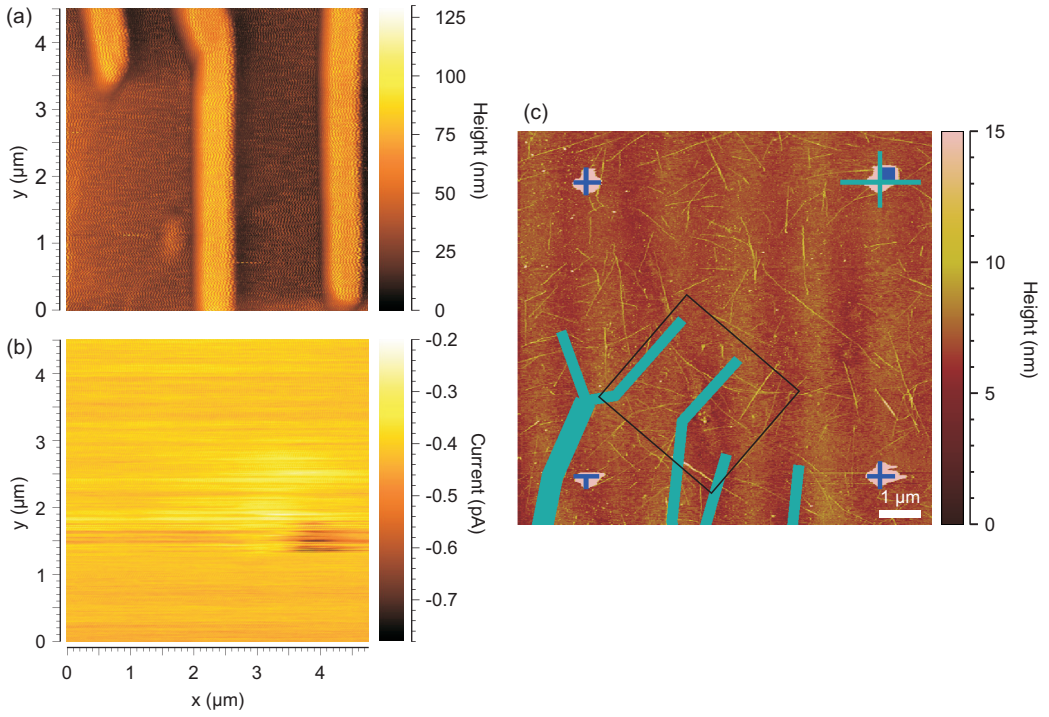

FIGURE 4.10 a) AFM height measured of a CNT FET on silicon during scanning with a SNOM probe and b) simultaneous current measurement through the device. Drain-source bias voltage is 50 mV, while the gate voltage is 0 V. The image is 384 by 384 points with 7 ms exposure time at each point, data from the right to left scanning direction is shown. Laser excitation was done with 10 mW power at 633 nm wavelength through a tip without metal coating, but with a 300 nm aperture in the cladding. In c) an AFM micrograph of the area before electrode fabrication is shown, and the electrode design is overlaid in turquoise. The alignment markers (blue overlay) were on the sample before applying the SWCNTs to aid electrode placement. The approximate area of the SNOM scan is marked with a black frame.

pA and the minimum 0.2 pA compared to a current of 0.45±0.1 pA when the excitation was not at the contacts. This effect is small and often not visible in otherwise functioning CNT FETs.

When the excitation power was greatly increased, effects could be seen much clearer. As can be seen in Fig. 4.11a, when a semiconducting device is excited with a 1064 nm laser at 632 mW power the effect on transistor behavior was significant. A large hysteresis effect is also visible in this device, as the current depends on the previous state of the channel at small gate voltages. In this case, it can be suspected that a photoinduced gate voltage in silicon could be responsible for the effect of the laser exposure, because the effect was more pronounced when the tip was at some distance above the sample surface. On the other hand, the response is slow, so desorption of chemicals off the CNT FETs could also play a role. Additionally, the power density is also large enough that the temperature change can have a significant effect on the CNT FET.

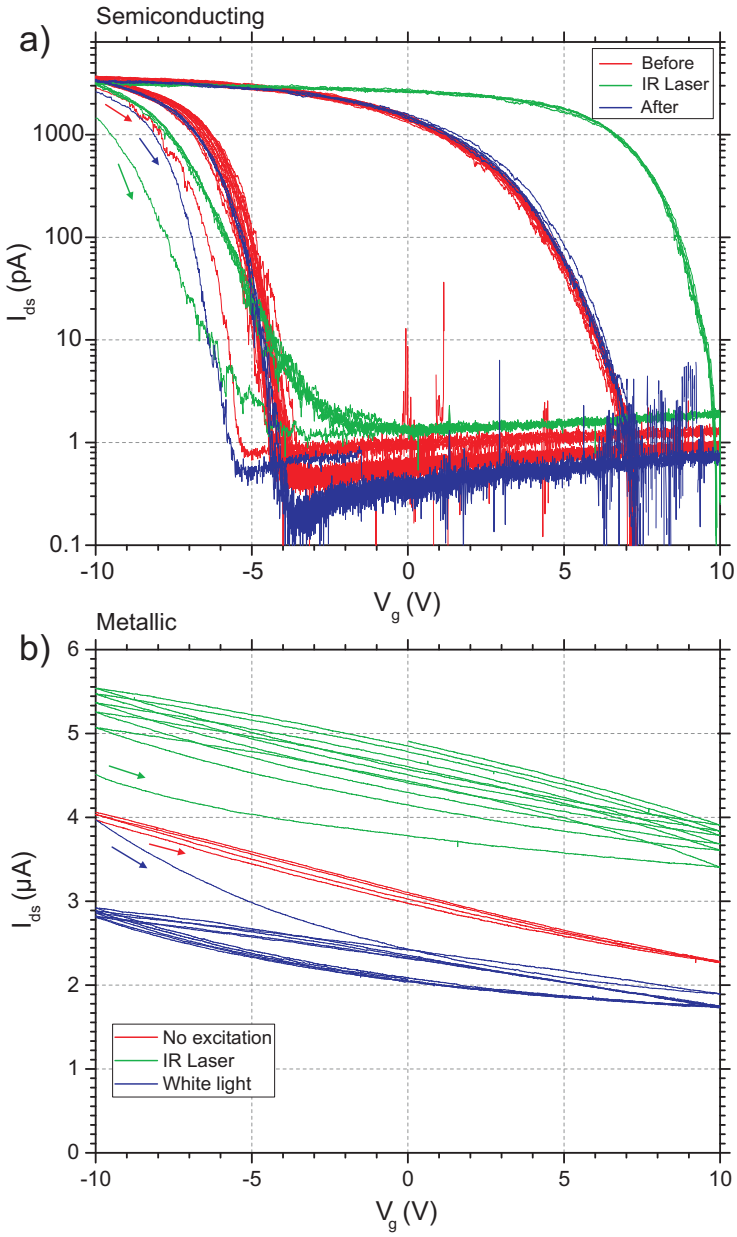

FIGURE 4.11 Drain-source current I_{ds} measured through carbon nanotube field effect transistors on Si/SiO_2 in response to gate voltage V_g and optical exposure. The drain-source voltage V_{ds} is 100 mV for all measurements, the V_g sweep cycles are 1000 s long and the measurements are started in the direction of the corresponding arrow. a) A *p*-type semiconducting device with laser exposure (1064 nm at 632 mW) through an SNOM tip without metal coating close to the CNT. Three measurements are plotted, with a comparison of behavior before, during and after the exposure. b) Response of a similarly made *p*-type metallic-type SWCNT device, with measurements with the IR laser made in a similar way. The white light exposure was done with a halogen lamp through a far-field microscope, details shown in text.

Similar measurements were also done with devices that presumably had metallic-type SWCNTs as seen in Fig. 4.11b. In this case, the current is much higher with the same V_{ds}. With a metallic tube, the response to optical excitation is much slower. Using the same IR laser at the same power, the current I_{ds} rises somewhat slower than with a semiconducting tube, with tens of minutes needed for saturation. The laser, with an initial measured output of 642 mW, has an output power of 200-250 mW through the SNOM tip. A metal coating cannot withstand this power level, so measurements were done with an uncoated tip. A crude estimation of the temperature increase in the sample was determined by exposing a Pt100 thermometer element to this power level, which resulted in its temperature rising from 22 °C to 80 °C. Surprisingly, turning on the halogen lamp of the top microscope (100 W lamp at 80 % power, measured output after the microscope 1.1 mW) results in a similarly slow decrease in current.

4.3 Discussion

4.3.1 Kretschmann measurements

The slow response of the CNT FET to optical excitation in the Kretschmann configuration rules out direct photoexcitation, which has a sub-millisecond timescale. Any changes this fast were not seen in the measurements. If the substrate would have been a semiconductor like silicon, there could have been a photovoltage generated at the dielectric-semiconductor interface due to photogeneration of carriers in the semiconductor [89]. Such an effect would be in a similar timescale than direct photoexcitation, and is not seen here because the backgate is a metal.

There has been a similar experiment with CNT FETs coated with gold nanoparticles, where the far-field light used for excitation will illuminate the CNT and its contacts, but an enhancement is reported only when the particles are used [161]. However, the power densities used are in the kW/cm^2 range. Similarly, a SWCNT film decorated with gold nanoparticles has been used as a light detector [82], where a temperature difference between SWCNT films with and without particles is generated by LSPR in the particles, producing an open circuit voltage. Large plasmonic antennas can be also produced with lithography for near-infrared detectors [42].

The response could also be simply the result of local heating of the device during optical excitation. However, the CNT FET temperature change can be calculated to be less than 1 K during the laser exposure (Supplementary material for A.I), which would not produce a significant electrical response. In addition, the control measurement was done with laser excitation of the same power but a different polarization, so the increase in temperature relative to the control would be even smaller. There was no hysteresis seen in response to gate voltage sweep, which implies that the polymer gate dielectric does not support charge traps that would cause

hysteresis.

Because the experiments were carried out in ambient conditions, the adsorption of gaseous species from the air to the CNT FET affect the electrical response. The time dependence of the CNT FET conductivity is on the same scale as in previously reported experiments involving photodesorption [19]. Therefore, the most likely reason for the observed effects is SPP-induced oxygen desorption from the CNT FET, possibly at the CNT-metal contact area [18].

4.3.2 SNOM measurements

SNOM promises a high optical resolution for imaging, but it has practical limitations that make it a specialized tool for certain types of applications. Unlike far-field optical microscopy, the need for a scanning probe limits applicable samples to flat surfaces. And unlike AFM, with apertured probes both the necessity of a (relatively) massive optical fiber and the use of a tuning fork limit the resolution in terms of topography. Additionally, both the condition of the aperture and its orientation have a huge impact on the optical signal. During scanning, mechanical wear and accumulation of debris can open or block the metal aperture, preventing subwavelength imaging. Scattering-type probes are simpler, but have a more limited field of applications, since light typically scatters also from other parts of the sample and not just the tip. Apertured SNOM is most suitable for plasmonic structures with relevant dimensions larger than 100 nm and in tip collection mode for imaging samples that emit light. Additionally, SNOM tips can be used for local optical excitation, e.g. for active components or for spectroscopy.

Gating the CNT FETs through a SNOM tip aperture was attempted, applying a large power density to a specific spot, at somewhat higher resolution than what far-field laser scanning would have provided. This method was successful in only a few devices made on silicon, where specific locations on the devices were shown to be sensitive to the laser. These excitations were fast, since each pixel in the SNOM image had a dwell time of 7 ms. The results showed a similar response for photocurrents that have previously been imaged with laser scanning at Schottky barriers in CNT-metal contacts, as photocurrents both without [41] and with [11] drain-source bias.

On some devices, imaging an active spot on the device was not successful, but optical excitation on a larger scale had a pronounced effect. Photovoltage generated in the silicon gate was one possible source of the effect the laser excitation had on the FET. At least for the IR laser, this explanation is partly supported by the fact that the laser had a larger effect when the uncoated SNOM tip was lifted off from the surface of the CNT FET. However, the response to the IR laser was slow (tens of minutes to saturation) both with semiconducting and metallic tubes. Previously published experiments have shown a negative shift in apparent gate voltage of -160

mV at maximum, saturating in regard to laser power, but here with a semiconducting tube the hysteresis window was extended in gate voltage terms 3 V in the positive direction (Fig. 4.11a), with a large difference between 100 mW and 642 mW excitation. Hysteresis was seen in all CNT FETs with a SiO_2 dielectric, in contrast to the Kretschmann devices on glass with a polymer dielectric film.

The temperature change also can have an effect, since with the laser the temperature can be tens of kelvin higher even when measuring with a thermometer in cubic millimeters. In this case the heating of the source or drain electrodes close to the tube can generate a photocurrent [8]. It should be noted that silicon starts to be transparent around the 1064 nm laser wavelength (and further in the IR) and thus some of the energy goes deeper into the sample. At high power levels the IR laser heats the sample by tens of kelvin, and this change can also decrease electrical resistance [63]. This interpretation is supported by the observation that the currents in all devices, also the off-state one in semiconducting CNT FETs, were increased with IR laser exposure.

As in experiments in the Kretschmann configuration, the desorption of chemical species, most likely oxygen, from the device could play a major role in the electrical response of several devices with both semiconducting and metallic behaviors. The lowering of current in a metallic-type CNT FET in response to white light could be due to the same effect as seen in Section 4.1 with SPP excitation in a semiconducting tube, but it is surprising that semiconducting tubes measured here are not sensitive to the same low power densities of white light. The IR excitation at 1064 nm should also have enough energy to remove physisorbed oxygen, as its binding energy is 0.25 eV when bound to a SWCNT [65], but instead the current slowly rises with this excitation for both types of CNT FETs. The situation may be different for the binding energy at the CNT-metal contact. If there is photodesorption in this case, it is masked by the effects of heating. In conclusion there are two likely and opposite causes for the photoresponse of the devices on silicon.

Chapter 5

Collective optical excitations in SWCNT films

The Kretschmann configuration is usually used to excite SPPs on metals, but it can be employed to probe collective excitations with evanescent waves more generally. In this chapter SWCNT films sorted in regard to electric properties are examined to find any possible plasmon-like features. The main focus is on thin films of metallic-type SWCNTs that have only recently become available in macroscopic quantities with relatively high purity. These experiments have been reported in Article A.II.

5.1 Experimental

The SWCNT powders used in the experiments were purchased from NanoIntegris Inc., including unsorted tubes and materials with 98 % metallic or 98 % semiconducting tubes as a percentage of total CNT content. The nanotubes had been sorted from raw arc discharge SWCNTs via repeated density gradient ultracentrifugation (DGU) [49]. The unsorted SWCNTs were also purified by using surfactants in an aqueous solution using a similar method. Both materials were prepared as powders with vacuum filtering and washing the surfactants off the SWCNTs with methanol. The tubes had an average diameter of 1.4 nm and their lengths ranged generally from 100 nm to 1 µm [99].

For producing thin films, the powders were dispersed to (1,2)-dichloroethane (DCE) with ultrasonication. This suspension was deposited as droplets on a heated (200 °C) float glass substrate. By depositing the tubes without surfactants, a high degree of bundling was seen in the films as evident in Fig. 5.1. For measurements, the glass sample was attached to a hemicylindrical prism with index oil.

The thin films were measured in the Kretschmann configuration, similarly as in Fig. 4.3, to determine any response to the excitation with evanescent waves. The light used for measuring the spectra was a 220 W tungsten-halogen lamp (Oriel), and the measured area on the film was 0.5 mm wide in the plane of incidence and

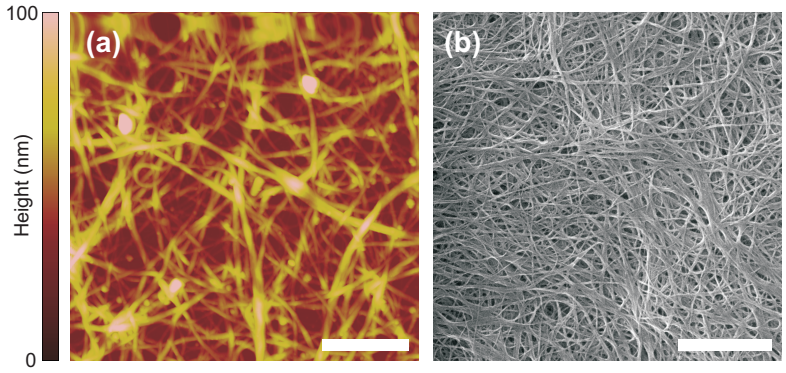

FIGURE 5.1 a) AFM image of a semiconducting-type SWCNT film and b) scanning electron micrograph of a metallic-type thick film (same sample as in Fig. 5.6). Separation was done with DGU, the films were deposited from a DCE suspension. Scale bars 1 µm.

4 mm across in the perpendicular direction. The specularly reflected light was collected via a lens to an optical fibre, which fed the signal to a spectrometer (Jobin Yvon iHR320) with a CCD array (Jobin Yvon Symphony). The anomalies in spectra seen in some measurements at around 950 nm are likely due to damage in the collection fiber, which makes the spectra slightly dependent on the bend of the fiber. The same setup was also used for measuring reflectance in Chapters 4 and 6. Since the rotation of the prism and the spectrometer collection lens were moved by hand, the intensities between the reflection spectrum measurements at different angles are not comparable, only the qualitative features of the spectra are. Exceptions are Figures 5.3b (only polarizer moved) and 5.6.

The TIR setup was used only in reflection mode, since any possible emission was too weak to be measured with these samples. Photoluminescence is possible with semiconducting tubes, not metallic ones. Additionally, if metallic tubes are present in bundles with semiconducting ones, photoluminescence is strongly quenched. [131]

Raman spectroscopy (Fig. 5.2) was used to evaluate the purity, defect density and diameter distribution of the SWCNT materials [29]. The RBM mode is unusually strong, which can be partly accounted for by the setup, where the detector has lower sensitivity when the Stokes shift moves the signal further into the infrared. The G mode peaks at 1580 cm^{-1} are strong, which indicates good resonance conditions with the 785 nm laser. The metallic-type material has a broader G^- mode, which is due to the presence of conduction electrons in tubes with metallic character. [66]

The diameter distribution of the CNT material seen in Table 5.1 can be determined from the full width at half maximum (FWHM) of the Raman RBM mode. The diameters are estimated using an empirical relation derived from diameters and RBM frequency data obtained from long isolated SWCNTs: $d = \frac{227}{\omega_{RBM}}$, where d is the SWCNT diameter in nm and ω_{RBM} the RBM frequency in cm^{-1}.

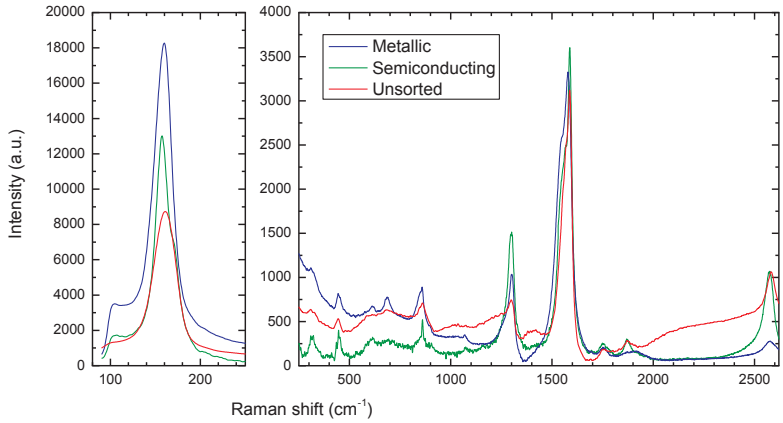

FIGURE 5.2 Raman spectra of SWCNT samples, produced with the arc discharge method. The films were measured with a Bruker Senterra R200 Raman microscope with a laser wavelength of 785 nm. The materials are from NanoIntegris Inc., who also separated the metallic and semiconducting fractions with DGU.

In this case the laser will be resonant with both metallic and semiconducting tubes of 1.4 nm diameter. The laser will not match the resonances of most other diameters, so they would not be seen in the spectra and can't be excluded from being present in the samples. As the material was stated to have a 1.4 nm diameter by NanoIntegris, the Raman measurements are used to confirm that a significant amount of the material is of this diameter, as seen in the RBM and G-band Raman peaks.

The diameter range from Raman has several possible chiralities for each sample. The metallic-type material has 14 possible SWCNT chiralities in the specified diameter range from the thinnest (14,5) at 1.337 nm to the thickest (13,10) at 1.565 nm if the tubes are assumed to be metallic. Similarly the semiconducting material would have 21 chiralities from (17,0) to (15,7) and the unsorted material 44 from (10,9) to (20,0). [104] Due to the wide range of chiralities in the samples, identifying single chiralities in absorption or reflection spectra is not possible with the equipment used in the measurements.

TABLE 5.1 CNT diameter distribution estimated from the FWHM of the RBM peaks in the Raman spectra in Fig. 5.2, see text.

CNT material	d_{peak} [nm]	d_{min} [nm]	d_{max} [nm]
Metallic	1.42	1.33	1.57
Semiconducting	1.45	1.32	1.53
Unsorted	1.41	1.29	1.57

5.2 Results

5.2.1 Metallic SWCNTs

When measuring optical spectra for metallic-type films, both E_{11}^M and E_{22}^M transitions are clearly seen in transmission. For thin films at reflection with *s*-polarization, the transitions are dispersive as clearly seen in Fig. 5.3b. The reflection spectra measured with *p*-polarization at TIR only show the absorption spectrum at variable intensities at each angle, and when the film thickness is well beyond 100 nm, the results are very similar also in regard to the intensity of absorption. This is possibly due to the limited range of the evanescent wave, so the results are essentially expected TIR absorption spectra.

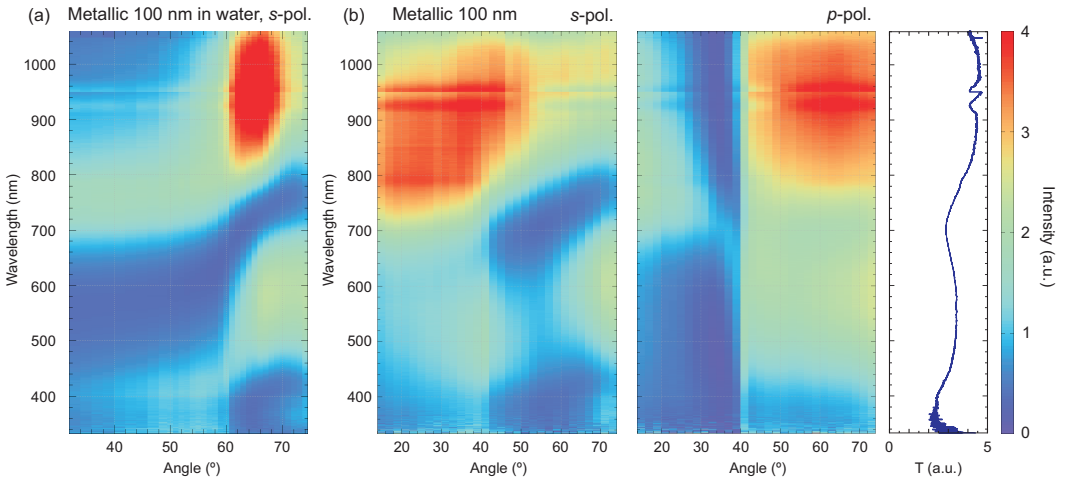

FIGURE 5.3 Reflectance of a 100 nm thick film of 98 % metallic SWCNTs in the Kretschmann configuration as a function of the incident angle. In a), reflectance spectra with *s*-polarized light measured from a film embedded in water is shown, and in b) reflectance spectra in air with a similar film is displayed with both polarizations.

When measuring the polarization dependence of the excitation light more accurately, the reflectance shows a clear minimum at *s*-polarization (Fig. 5.4). The angle dependence is also shifted when the medium behind the film is changed from air to water (Fig. 5.3a). In this case the sample had a water-filled container behind the sample glass, changing the TIR threshold angle to 61°.

To test the dependence of the angle-dependent resonances on the surface of the film, a 100 nm thick metallic SWCNT film was coated with a 50 nm layer of gold with electron beam evaporation in ultra-high vacuum. The reflectance spectra of this sample in Fig. 5.5 show a disappearance of the previously seen angle dependence. At *p*-polarization, the expected SPP resonance of gold is seen, but for the SWCNT portion the excitonic transitions are seen only similarly as in transmission spectra in samples without gold.

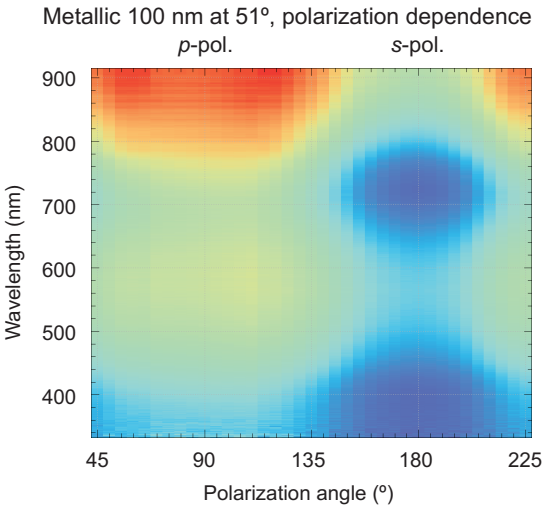

FIGURE 5.4 Polarization dependence of reflectance measured with a 100 nm thick film of 98 % metallic SWCNTs in the Kretschmann configuration. The incidence angle is fixed at 51°, and a prism polarizer is used to set the polarization. The reflectance intensities between angles are comparable.

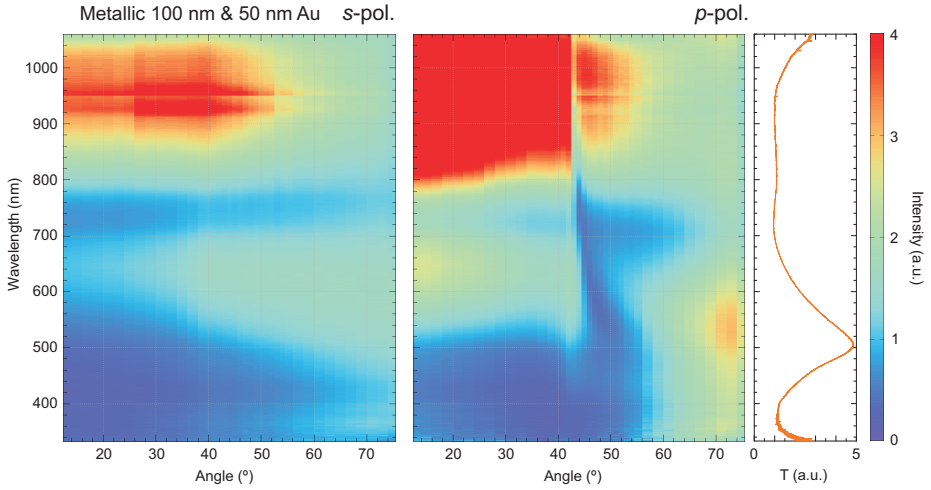

FIGURE 5.5 Reflectance spectra as a function of angle of incidence of a 100 nm metallic SWCNT film with a 50 nm gold layer on top in the Kretschmann configuration.

Thickness dependence

For metallic-type SWCNT films, the reflection spectra depend on thickness as seen in Fig. 5.6, but only for *s*-polarization. The reach of the evanescent wave in TIR conditions on the glass-air interface without CNTs would be roughly 100 nm, which corresponds to the film thickness with the most well-defined absorbance in reflection. There is also some dispersion as a function of thickness, with the E_{11}^{M} resonance in particular shifting to lower energies when the film becomes thicker.

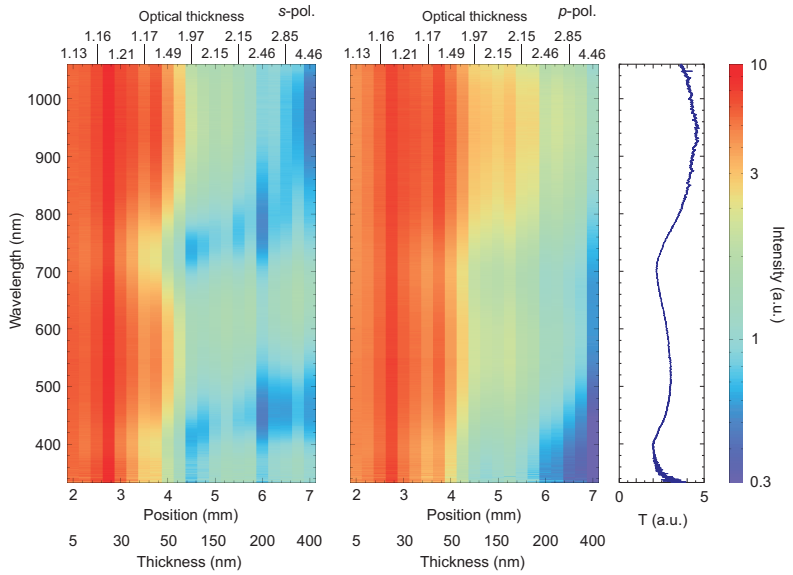

FIGURE 5.6 Thickness dependence in Kretschmann reflection spectra of a metallic SWCNT film sample in air at an excitation angle of 51° from normal. Intensities as measured (smoothed version in A.II). Optical thickness refers to the transmission intensity at 900 nm wavelength divided by the intensity at 700 nm, close to the M_{11} resonance. Reproduced with permission from article A.II.

For thin metallic SWCNT films there is no clear angle dependence, instead the reflectance spectra are not distinguishable from the transmission spectrum. As seen for a 45 nm thick film in Fig. 5.7, only the intensity changes with the angle. It should be noted that this particular sample was deposited by spray-coating the DCE suspension with a paint gun on a heated glass slide, so that it had a somewhat more even thickness distribution. Using RIE with oxygen plasma on a 100 nm metallic SWCNT film, damaging the tubes and thinning the film, both weakened the resonances and made the dispersion less prominent.

5.2.2 Semiconducting SWCNTs

The E_{11}^{S} exciton transition for semiconducting tubes with 1.4 nm diameter is in the infrared (1600 nm wavelength) and is not within the range of the measurement

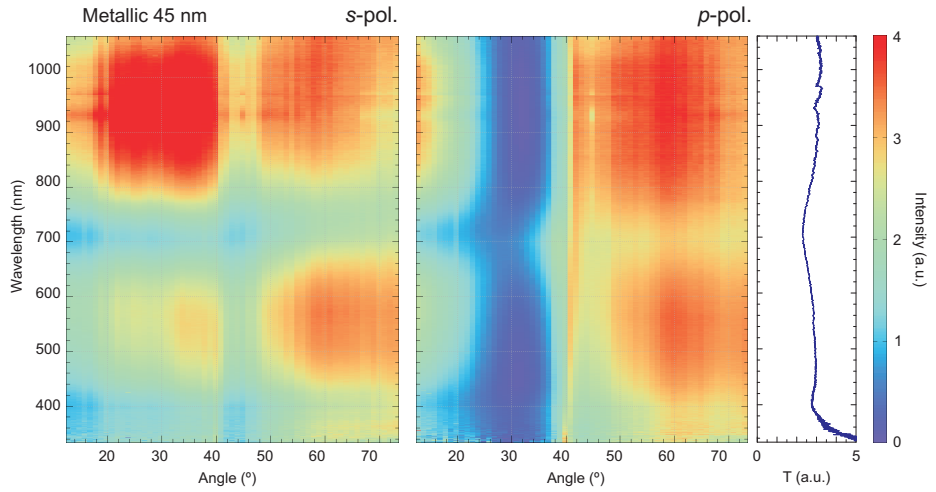

FIGURE 5.7 Kretschmann reflection spectra and the transmission spectrum of a 45 nm thick spray-coated metallic SWCNT film. The M_{11} and M_{22} resonances do not move significantly in terms of wavelength in respect to the excitation angle.

setup. The E_{22}^S transition is at 1000 nm, which is visible especially in the transmission spectrum seen on the right in Fig. 5.8a. Additionally the E_{33}^S and E_{44}^S transitions for the previously determined diameter range should appear between 370 nm and 570 nm. These transitions are hard to identify in the film transmission or reflectance spectra, instead there is a general increase in absorption when moving to shorter wavelengths.

In reflectance spectra on the left side of Fig. 5.8a there were no clear angle-dependent resonances visible, but there is a more prominent change in respect to the TIR critical angle. At the incident angles in the TIR range, there is more absorption at *s*-polarization, which could be due to the nature of the excitonic absorption of the SWCNTs. At *s*-polarization, the electric field of the photons is always aligned along the film. Because the tubes mostly lay flat on the substrate, at *s*-polarization more tubes are parallel to the polarization than at *p*-polarization. This should result in a higher absorbance than at *p*-polarization where the field is mainly through the film, because the absorption of the SWCNTs is higher when the polarization is along the tube, as discussed in Section 2.1.2. With both polarizations the reflection spectra above the TIR angle match with the transmission spectrum. Before the critical angle, there is more reflectance in the NIR region above 900 nm.

5.2.3 Unsorted SWCNTs

The transmission spectrum of unsorted tubes has transitions of both the metallic and semiconducting tubes visible. In particular, M_{11} resonance at 700 nm for metallic tubes can be seen also in the reflection spectra in Fig. 5.8b, but it does not have a clear dispersion. This result indicates that the metallic proportion of roughly one

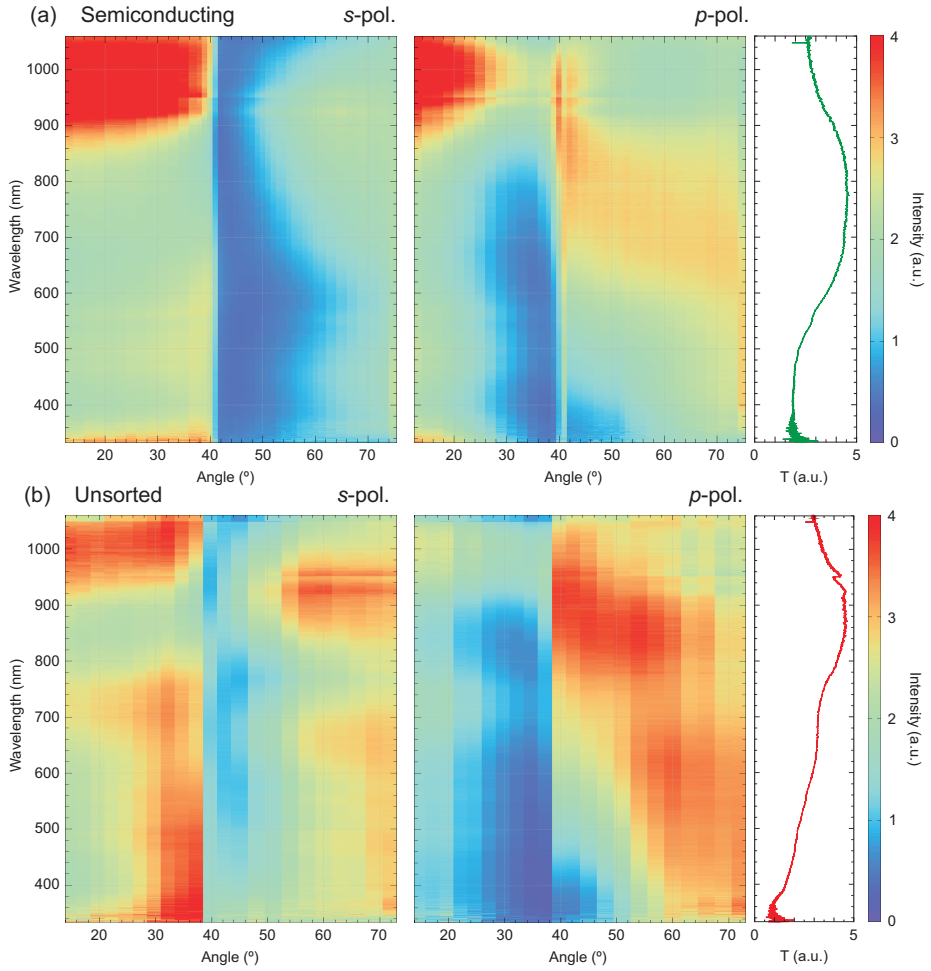

FIGURE 5.8 Reflectance of 100 nm thick SWCNT films in the Kretschmann configuration. The films are made from a) 98 % semiconducting SWCNTs and b) unsorted SWCNTs. The transmission spectra of the same measurement locations are displayed on the right.

third in the unsorted film is not enough for the resonances to be clear and dispersive. Again, the reflection intensity is lower at *s*-polarization, indicating that more excitonic absorbance would occur when the polarization is aligned with the axes of the tubes in the film.

5.3 Discussion

Clear dispersive resonances were only seen for metallic-type SWCNTs. The difference in the spectral shapes of *s*- and *p*-polarized reflection can be possibly attributed to optical anisotropy of SWCNT films. There are very few publications where the anisotropic dielectric function of CNT films have been experimentally obtained [35]. These measurements are for unsorted and unaligned SWCNT films. For sorted tubes, there are currently only isotropic attempts ([13], Supplementary

in [108]). The difficulty of acquiring a specular reflection from a CNT film most likely explains the lack of ellipsometry results.

Nevertheless, the peak of the extinction coefficient in [35] moves in regard to photon energy when the density of the SWCNT film is altered. This could explain partially the dispersion as a function of film thickness, if the film does not have a constant density through its thickness.

One possibility to consider is a cavity mode between the interfaces of the metallic-type SWCNT film, that can be considered as a type of interference [14]. Such modes with angle-dependent dispersion are possible between two reflective interfaces, which usually would be metal mirrors. Strong coupling of this cavity mode with excitons of single-chirality SWCNTs situated between metal layers has recently been demonstrated [47]. However, the dispersion of the resonance would have shorter wavelength with higher angle of incidence from the normal (like in thin-film interference), which is opposite to the one observed. The reflectance of the sample in Fig. 5.5 with metallic SWCNTs covered by gold show no angle-dependence of the M_{11} resonance, unlike the same sample without coating. If the observed resonances would be related to a cavity mode produced by reflections between film interfaces, the features would only strengthen.

The configuration of the sample is somewhat analogous to an array of metal nanowires on a waveguide, which have been shown to possess *s*-polarized resonances on reflection. These waveguide-plasmon polaritons are excited when the electric field of the incoming light is perpendicular to the nanowire [23]. With SWCNT bundles, the situation can be similar in terms of nanoscale wires, but there is no explicit waveguide in the system. On the other hand, the SWCNT layer itself is porous and has a thickness of 100 nm.

Because the sample is made of nanowires that also are at regular spacings in bundles, there is also a possibility that they couple with each other to produce magnetic resonances [118]. Magnetic plasmon polaritons would also be dispersive at *s*-polarization, the opposite of electric ones. In addition to the polarization dependence, this interpretation is supported by the influence of the dielectric environment to the dispersion, implying surface waves. In this case there could also be coupling with excitons to produce exciton-plasmon states [50]. However, the actual explanation of the discussed resonances is still unclear.

Chapter 6

Optical anisotropy in PEDOT:PSS

Conductive polymers can be considered to be somewhat analogous to graphitic materials, with similar bonding between carbon atoms and a relatively high charge mobility. With this in mind, we studied thin films of conductive polymers to see if there are any similar collective optical effects that were seen for metallic SWCNTs in Chapter 5. The films were measured in a TIR configuration to see if there would be any previously undetected optical phenomena. Additionally, films of a graphene-containing polymer composite were measured as a comparison. In addition to optical properties, sheet conductivity, roughness and effects of different deposition methods were tested. These results were reported in Article A.III of this dissertation.

6.1 Experimental details

We studied spray- and spin-coated thin PEDOT:PSS films for changes in optical and electric properties. A PEDOT:PSS/-graphene composite (Innophene Phene+ I3015 inkjet ink) was measured in comparison to Clevios PH500 PEDOT:PSS ink. The inks are water-based and baked after deposition. Some inks were treated with 90 minutes of sonication (Elma S120H bath sonicator, 1000 W) to see if the properties change due to possible reduction in graphene flake size.

To check for optical anisotropy and any possible collective excitations related to graphene, a total internal reflection (TIR) configuration was used for reflection spectroscopy. The attenuated TIR provides a higher absorbance signal of thin films than a transmittance measurement. The evanescent wave produced at the interface provides conditions also for producing surface plasmon polaritons, if the film can support them. As a comparison, variable angle spectroscopic ellipsometry was performed (J.A. Woollam M-2000UI) to determine the refractive index n and extinction coefficient k as a function of wavelength for simulation purposes. Optical absorbance was separately measured with a PerkinElmer Lambda 850 UV/VIS Spectrometer.

The structure of the films was also characterized with AFM and SEM to determine film thickness and roughness. Sheet resistance measurements were done using a Keithley 2456 Sourcemeter with a linear four-point setup with mercury-dipped spikes, where current was fed and measured through the two outer electrodes and voltage was measured between the inner electrodes.

6.2 Results

Four-point sheet resistance measurements were done on 6-10 samples of each type with different thicknesses. Spray-coated PEDOT:PSS/graphene films had a conductivity of 310±40 S/cm, which was essentially unchanged at 320±60 S/cm for films of the same material that were treated with sonication. Bare PEDOT:PSS films had a conductivity of 0.8±0.3 S/cm (Fig. 6.1). All of the conductance difference cannot be attributed to only the graphene content, since the Innophene PEDOT:PSS/graphene ink also contains diethylene glycol, a secondary dopant. Optical absorbance per thickness based on the same samples was 0.27±0.03 μm^{-1} for PEDOT:PSS/graphene, unchanged 0.28±0.05 μm^{-1} for sonicated PEDOT:PSS/graphene and 0.46±0.05 μm^{-1} for PEDOT:PSS.

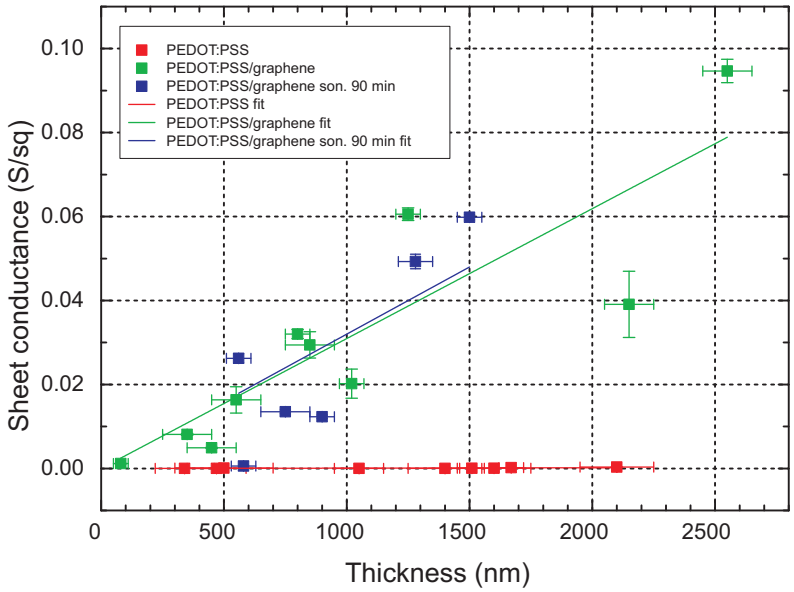

FIGURE 6.1 Plot of sheet conductance as a function of film thickness for spray-coated PEDOT:PSS and PEDOT:PSS/graphene thin films, some with 90 minutes of sonication before film fabrication. The plot includes linear fits for each material used to determine conductivity.

6.2.1 Simulated reflectance

Reflection spectra were simulated using the transfer-matrix method with anisotropic refractive indices obtained from spectroscopic ellipsometry. For spray-coated samples these simulations do not match measurements very well due to the roughness of the thin films. The general trend of the interference patterns can be obtained from the simulations, as seen in Fig. 6.2a-b. The curvature of interference fringes is due to the change in refractive index as a function of wavelength.

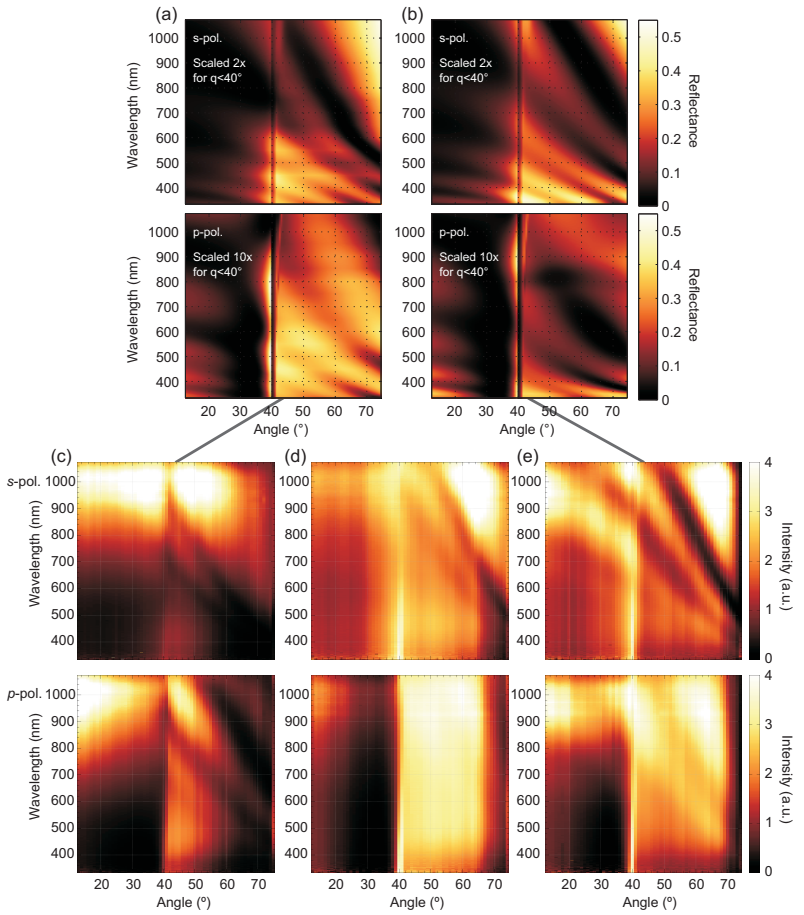

FIGURE 6.2 Reflection spectra of thin films in TIR conditions. The upper rows display reflectance with *s*-polarized light and lower rows *p*-polarized. In (a,b) the spectra are simulated from ellipsometry data: (a) PEDOT:PSS, 500 nm thick, refractive index was obtained from previously published data measured from spin-coated samples [110]. (b) PEDOT:PSS/graphene 560 nm thick, sonicated, refractive index obtained from ellipsometry of spray-coated samples. Reflectance spectra below 40° angles are scaled. (c-e) Measured reflection spectra in TIR (Kretschmann) conditions: (c) PEDOT:PSS, 500 nm thick, (d) PEDOT:PSS/graphene 550 nm thick, (e) PEDOT:PSS/graphene 560 nm thick, which was sonicated for 90 min in an attempt to reduce graphene flake size. The intensities of measured reflectance spectra at different angles are not to scale. Adapted with permission from article A.III.

6.2.2 Reflectance measurements

The reflectance measurements revealed clear interference patterns, especially in the TIR angle region as seen in Figures 6.2c-e. The interference maxima and minima are clearly different at *s*- and *p*-polarizations, which points to anisotropic optical properties. The *s*-polarized incident light only experiences the refractive index parallel to the film, while at *p*-polarization also the perpendicular direction of the refractive index affects the reflection. The addition of graphene does not seem to result in a significant change in anisotropy (Fig. 6.2d-e). Interestingly, the resonances from interference seem to be better defined for samples with graphene and even more so for samples that were treated with sonication.

6.3 Discussion

The main motivation for using TIR spectroscopy to measure conductive polymers with graphene was to search for collective optical modes that might result from their complex structure. Thin films of PEDOT:PSS can have a highly anisotropic structure at least for some methods of production. Usually spin-coated films have been studied due to their relatively smooth surface and ease of control on the thickness of the film. Spray-coating, similar to inkjet printing, produces much rougher films than spin-coating.

In this study it was seen that spray-coating also produces highly anisotropic films, contrary to earlier assumptions. Previously it has been thought that the spin-coating process, necessary to make films smooth enough for ellipsometry, would be the reason for the alignment of highly conductive PSS-rich region along the plane of the thin film [110]. A second reason, more likely in this case, is that the drying process during film processing orients the PEDOT chromophores parallel to the film [33].

Any angle-dependent resonances that cannot be explained by interference and uniaxial anisotropy were not seen in PEDOT:PSS films, with or without graphene. Even though a similar TIR configuration can be used to excite SPPs on suitable metal films, the films measured here do not support such plasmonic phenomena in optical wavelengths. To test that the interference pattern really is one, the surface of one sample was blocked with a thin gold film, similarly as in Chapter 5, and the pattern remained the same in the case of the PEDOT:PSS film, unlike previously with metallic SWCNTs. With one surface changed to a metal mirror, the interference pattern will not change in terms of angle and wavelength. Interestingly, the resonances from interference seem to be better defined for samples with graphene, which could indicate smoother surfaces or alternatively a more consistent refractive index in the sample.

With the reflectance measurements in a TIR configuration, it was possible to evaluate the optical properties of optically absorbing films as thick as 2.5 µm, which

would not give a reasonable signal in ellipsometry measurements. Additionally, uneven films that do not give a decent specular reflection that is needed for ellipsometry, can be measured with this method.

Chapter 7

Summary and outlook

Plasmonics in graphene has attained considerable interest in recent years, but applying carbon nanotubes in plasmonics has been much less popular. The contents of this thesis shed light on the latter area, with some results also in related fields.

Optical gating of CNT FETs

We have demonstrated that the current in CNT FETs can be controlled with plasmons, at least using a chemically intermediated process. Excluding the possibility of direct far-field optical excitation required an unconventional sample design, which had a relatively low fabrication yield and durability. Nevertheless, SPP-mediated gating showed higher sensitivity than with far-field excitation, and this result could have applications in optical sensors.

These downsides could be overcome by having a more durable dielectric deposited on the device, since the thin polymer layer was often removed during processing, and could not handle much gate voltage. However, the underlaying silver layer is prone to oxidation, which will destroy its optical properties. For a good quality oxide, atomic layer deposition (ALD) would be the best option. There are specific coating recipes for oxides, such as Al_2O_3 or TiO_2 [126], which have been used to protect silver from corrosion in optical or plasmonic applications.

The response of CNT FETs to optical excitation was also studied using SNOM, and active areas were found at the CNT-metal contacts. Far-field optical excitation also had pronounced effects, which may be due to desorption of chemical species, due to temperature change, or because of photovoltage generation in silicon.

Optical properties of SWCNT films

SWCNT materials with selected metallic chiralities were shown to display interesting collective optical effects, resulting in an anisotropic optical response. The angle-dependence of the SWCNT optical transitions in the Kretschmann configuration for metallic-type films of a specific thickness is a novel result, and should ignite new

interest in optical resonances arising from excitations in a large amount of similar tubes. The research could have applications in metamaterials, if the resonances are magnetic in nature. Research on the unusual optical properties of purified metallic-type SWCNTs is also useful in the case that films of this material are applied as transparent conductors.

The SWCNT films that were measured in this research had a variety of chiralities, were aligned randomly along the plane, had various degrees of bundling and a relatively uneven thickness. All of these factors affect the measurements, and could be controlled better, if some improvements in sample fabrication would be implemented. After the publication of article A.II, high-purity sorting of single chirality tubes has been accomplished in a macroscopic scale for semiconducting tubes, but unfortunately the metallic tubes relevant for this research are more difficult to separate [151]. Still, better tube material would contribute to sharper resonances and more insight to the nature of the phenomenon.

The second major improvement would involve having a unidirectional film, which would give information on the directionality of the resonances and on the optical anisotropy of the SWCNT film. To achieve this, there are several possible methods. The easiest way would be to directly grow the tubes as a nanotube forest and possibly comb it over in one direction, but synthesis methods are not yet selective enough to have a consistently metallic-type film. From a suspension, a flow of liquid [147] or a moving interface of a droplet over a substrate [122] can be used to direct the tubes with some success. Dielectrophoresis is also possible, but requires electrodes and is not suitable for a thick film. Surfactant-aided crystallization has also been suggested, but would only produce small islands of directed film [71]. Vacuum filtration, however, has been shown to have the best results of possible methods so far [53].

Conductive polymers

Conductive polymers have applications mostly as thin films, and specifically for transparent ones like PEDOT:PSS optical properties are also important in addition to electrical ones. For non-flat surfaces spin coating, which provides a smooth surface, is not possible. The relatively rough surface provided by spray coating on the other hand is not that suitable for optical measurement due to scattering, and the properties of the polymer film may also depend on the deposition method. As an application of the research, spectroscopy in TIR conditions was shown to be useful in checking the optical anisotropy in rough or thick films of PEDOT:PSS, even though the original purpose of the research was to search for more complex collective optical excitations.

The polymer materials used in the measurements were commercial ones, of which the Clevios PH series has seen widespread use in applied research [33]. The Innophene polymer inks have been used significantly less (a dozen articles as of

2016), and as a commercial material, the exact contents are not available. Relevant to this research, the amount of graphene flakes in the Innophene ink and their size is not precisely known, and this ink also has extra dopants in relation to the Clevios PH500 ink. A more robust approach in studying the effects of graphene would be to produce and add the flakes in controlled amounts to the ink. For studying graphene plasmons in the flakes with possible coupling to the polymer matrix, as well as possible plasmonic excitations in the conductive polymer itself, additional spectroscopic studies further in the infrared would also be needed.

The approaches used in the development of conductive polymers could also be used in an attempt to increase the conductivity of SWCNT films. A carbon nanotube is analogous to the conjugated backbone of a conductive polymer, and by selectively functionalizing SWCNTs a charge transfer complex could be created to improve intertube conductivity. This could be done by e.g. amino functionalization for some tubes and carboxyl functionalization for others, forming a macromolecular salt of SWCNTs. To maximize conductivity, metallic tubes obtained from chirality sorting could be used. Functionalization as such generally decreases the conductivity of an individual tube, but this might be offset by the additional charge transfer between the tubes. A secondary dopant could also be applied (such as ethylene glycol for PEDOT:PSS), filling the spaces in the SWCNT network and facilitating additional conductivity.

Bibliography

[1] GARCIA DE ABAJO, F. J., *Graphene plasmonics: challenges and opportunities*. ACS Photonics **1** (2014) 135–152.

[2] AIKAWA, S., EINARSSON, E., THURAKITSEREE, T., CHIASHI, S., NISHIKAWA, E., AND MARUYAMA, S., *Deformable transparent all-carbon-nanotube transistors*. Appl. Phys. Lett. **100** (2012) 063502.

[3] ALLEN, M. J., TUNG, V. C., AND KANER, R. B., *Honeycomb carbon: a review of graphene*. Chem. Rev. **110** (2009) 132–145.

[4] ARNOLD, M. S., STUPP, S. I., AND HERSAM, M. C., *Enrichment of single-walled carbon nanotubes by diameter in density gradients*. Nano Lett. **5** (2005) 713–718.

[5] AUMANEN, J., JOHANSSON, A., KOIVISTOINEN, J., MYLLYPERKIÖ, P., AND PETTERSSON, M., *Patterning and tuning of electrical and optical properties of graphene by laser induced two-photon oxidation*. Nanoscale **7** (2015) 2851–2855.

[6] AVOURIS, P., CHEN, Z., AND PEREBEINOS, V., *Carbon-based electronics*. Nat. Nanotechnol. **2** (2007) 605–615.

[7] AVOURIS, P. AND FREITAG, M., *Graphene photonics, plasmonics, and optoelectronics*. IEEE J. Sel. Top. Quant. **20** (2014) 72–83.

[8] AVOURIS, P., FREITAG, M., AND PEREBEINOS, V., *Carbon-nanotube photonics and optoelectronics*. Nat. Photon. **2** (2008) 341–350.

[9] AXELROD, D., BURGHARDT, T. P., AND THOMPSON, N. L., *Total internal reflection fluorescence*. Annu. Rev. Biophys. Bio. **13** (1984) 247–268.

[10] BAILO, E. AND DECKERT, V., *Tip-enhanced Raman scattering*. Chem. Soc. Rev. **37** (2008) 921–930.

[11] BALASUBRAMANIAN, K., FAN, Y., BURGHARD, M., KERN, K., FRIEDRICH, M., WANNEK, U., AND MEWS, A., *Photoelectronic transport imaging of individual semiconducting carbon nanotubes*. Appl. Phys. Lett. **84** (2004) 2400–2402.

[12] BARNES, T., BLACKBURN, J., VAN DE LAGEMAAT, J., COUTTS, T., AND HEBEN, M., *Reversibility, dopant desorption, and tunneling in the temperature-dependent conductivity of type-separated, conductive carbon nanotube networks*. ACS Nano **2** (2008) 1968–1976.

[13] BATTIE, Y., JAMON, D., NACIRI, A. E., LAURET, J.-S., AND LOISEAU, A., *Chirality distribution in single walled carbon nanotube films by spectroscopic ellipsometry*. Appl. Phys. Lett. **102** (2013) 091909.

[14] BECKER, H., BURNS, S., TESSLER, N., AND FRIEND, R., *Role of optical properties of metallic mirrors in microcavity structures*. J. Appl. Phys. **81** (1997) 2825–2829.

[15] BELIN, T. AND EPRON, F., *Characterization methods of carbon nanotubes: a review*. Mat. Sci. Eng. B **119** (2005) 105–118.

[16] BETHUNE, D., KLANG, C., DE VRIES, M., GORMAN, G., SAVOY, R., VAZQUEZ, J., AND BEYERS, R., *Cobalt-catalysed growth of carbon nanotubes with single-atomic-layer walls*. Nature **363** (1993) 605–607.

[17] BONACCORSO, F., SUN, Z., HASAN, T., AND FERRARI, A., *Graphene photonics and optoelectronics*. Nat. Photon. **4** (2010) 611–622.

[18] BONDAVALLI, P., LEGAGNEUX, P., AND PRIBAT, D., *Carbon nanotubes based transistors as gas sensors: state of the art and critical review*. Sens. Actuators B Chem. **140** (2009) 304–318.

[19] CHEN, R., FRANKLIN, N., KONG, J., CAO, J., TOMBLER, T., ZHANG, Y., AND DAI, H., *Molecular photodesorption from single-walled carbon nanotubes*. Appl. Phys. Lett. **79** (2001) 2258.

[20] CHEN, Y., SHEN, Z., XU, Z., HU, Y., XU, H., WANG, S., GUO, X., ZHANG, Y., PENG, L., DING, F., *et al.*, *Helicity-dependent single-walled carbon nanotube alignment on graphite for helical angle and handedness recognition*. Nat. Commun. **4** (2013) 2205.

[21] CHEN, Z., APPENZELLER, J., KNOCH, J., LIN, Y.-M., AND AVOURIS, P., *The role of metal-nanotube contact in the performance of carbon nanotube field-effect transistors*. Nano Lett. **5** (2005) 1497–1502.

[22] CHIANG, C. K., FINCHER JR, C., PARK, Y. W., HEEGER, A. J., SHIRAKAWA, H., LOUIS, E. J., GAU, S. C., AND MACDIARMID, A. G., *Electrical conductivity in doped polyacetylene*. Phys. Rev. Lett. **39** (1977) 1098.

[23] CHRIST, A., ZENTGRAF, T., KUHL, J., TIKHODEEV, S., GIPPIUS, N., AND GIESSEN, H., *Optical properties of planar metallic photonic crystal structures: Experiment and theory*. Phys. Rev. B **70** (2004) 125113.

[24] COLLINS, P. G., BRADLEY, K., ISHIGAMI, M., AND ZETTL, A., *Extreme oxygen sensitivity of electronic properties of carbon nanotubes*. Science **287** (2000) 1801–1804.

[25] COOPER, D. R., D'ANJOU, B., GHATTAMANENI, N., HARACK, B., HILKE, M., HORTH, A., MAJLIS, N., MASSICOTTE, M., VANDSBURGER, L., WHITEWAY, E., *et al.*, *Experimental review of graphene*. ISRN Condensed Matter Physics **2012** (2012).

[26] DE VOLDER, M. F., TAWFICK, S. H., BAUGHMAN, R. H., AND HART, A. J., *Carbon nanotubes: present and future commercial applications*. Science **339** (2013) 535–539.

[27] DERYCKE, V., MARTEL, R., APPENZELLER, J., AND AVOURIS, P., *Controlling doping and carrier injection in carbon nanotube transistors*. Appl. Phys. Lett. **80** (2002) 2773–2775.

[28] DRESSELHAUS, M. S., DRESSELHAUS, G., SAITO, R., AND JORIO, A., *Raman spectroscopy of carbon nanotubes*. Phys. Rep. **409** (2005) 47–99.

[29] DRESSELHAUS, M. S., JORIO, A., HOFMANN, M., DRESSELHAUS, G., AND SAITO, R., *Perspectives on carbon nanotubes and graphene Raman spectroscopy*. Nano Lett. **10** (2010) 751–758.

[30] DREYER, D. R., PARK, S., BIELAWSKI, C. W., AND RUOFF, R. S., *The chemistry of graphene oxide*. Chem. Soc. Rev. **39** (2010) 228–240.

[31] DUKOVIC, G., BALAZ, M., DOAK, P., BEROVA, N. D., ZHENG, M., MCLEAN, R. S., AND BRUS, L. E., *Racemic single-walled carbon nanotubes exhibit circular dichroism when wrapped with DNA*. J. Am. Chem. Soc. **128** (2006) 9004–9005.

[32] EBBESEN, T. W., LEZEC, H., GHAEMI, H., THIO, T., AND WOLFF, P., *Extraordinary optical transmission through sub-wavelength hole arrays*. Nature **391** (1998) 667–669.

[33] ELSCHNER, A., KIRCHMEYER, S., LOVENICH, W., MERKER, U., AND REUTER, K., *PEDOT: Principles and applications of an intrinsically conductive polymer* (CRC Press, 2010).

[34] FALCAO, E. H. AND WUDL, F., *Carbon allotropes: beyond graphite and diamond*. J. Chem. Technol. Biot. **82** (2007) 524–531.

[35] FANCHINI, G., MILLER, S., PAREKH, B. B., AND CHHOWALLA, M., *Optical anisotropy in single-walled carbon nanotube thin films: implications for transparent and conducting electrodes in organic photovoltaics*. Nano Lett. **8** (2008) 2176–2179.

[36] FANG, Z., THONGRATTANASIRI, S., SCHLATHER, A., LIU, Z., MA, L., WANG, Y., AJAYAN, P. M., NORDLANDER, P., HALAS, N. J., AND GARCIA DE ABAJO, F. J., *Gated tunability and hybridization of localized plasmons in nanostructured graphene*. ACS Nano **7** (2013) 2388–2395.

[37] FANO, U., *The theory of anomalous diffraction gratings and of quasi-stationary waves on metallic surfaces (Sommerfeld's waves)*. J. Opt. Soc. Am. **31** (1941) 213–222.

[38] FEI, Z., RODIN, A., ANDREEV, G., BAO, W., MCLEOD, A., WAGNER, M., ZHANG, L., ZHAO, Z., THIEMENS, M., DOMINGUEZ, G., *et al.*, *Gate-tuning of graphene plasmons revealed by infrared nano-imaging*. Nature **487** (2012) 82–85.

[39] FERRARI, A. C., *Raman spectroscopy of graphene and graphite: disorder, electron–phonon coupling, doping and nonadiabatic effects*. Solid State Commun. **143** (2007) 47–57.

[40] FERRARI, A. C. AND BASKO, D. M., *Raman spectroscopy as a versatile tool for studying the properties of graphene*. Nat. Nanotechnol. **8** (2013) 235–246.

[41] FREITAG, M., TSANG, J., BOL, A., YUAN, D., LIU, J., AND AVOURIS, P., *Imaging of the Schottky barriers and charge depletion in carbon nanotube transistors*. Nano Lett. **7** (2007) 2037–2042.

[42] FUNG, C. K. M., XI, N., SHANKER, B., AND LAI, K. W. C., *Nanoresonant signal boosters for carbon nanotube based infrared detectors*. Nanotechnology **20** (2009) 185201.

[43] GABOR, N., ZHONG, Z., BOSNICK, K., PARK, J., AND MCEUEN, P., *Extremely efficient multiple electron-hole pair generation in carbon nanotube photodiodes*. Science **325** (2009) 1367.

[44] GARREAU, S., LOUAM, G., LEFRANT, S., BUISSON, J., AND FROYER, G., *Optical study and vibrational analysis of the poly (3, 4-ethylenedioxythiophene)(PEDT)*. Synth. Met. **101** (1999) 312–313.

[45] GEIM, A. K., *Graphene: status and prospects*. Science **324** (2009) 1530–1534.

[46] GEORGAKILAS, V., OTYEPKA, M., BOURLINOS, A. B., CHANDRA, V., KIM, N., KEMP, K. C., HOBZA, P., ZBORIL, R., AND KIM, K. S., *Functionalization of graphene: covalent and non-covalent approaches, derivatives and applications*. Chem. Rev. **112** (2012) 6156–6214.

[47] GRAF, A., TROPF, L., ZAKHARKO, Y., ZAUMSEIL, J., AND GATHER, M. C., *Near-infrared exciton-polaritons in strongly coupled single-walled carbon nanotube microcavities*. Nat. Commun. **7** (2016) 13078.

[48] GRAMOTNEV, D. K. AND BOZHEVOLNYI, S. I., *Plasmonics beyond the diffraction limit*. Nat. Photon. **4** (2010) 83–91.

[49] GREEN, A. A. AND HERSAM, M. C., *Ultracentrifugation of single-walled nanotubes*. Mater. Today **10** (2007) 59–60.

[50] GRÜNING, M., MARINI, A., AND GONZE, X., *Exciton-plasmon states in nanoscale materials: breakdown of the Tamm-Dancoff approximation*. Nano Lett. **9** (2009) 2820–2824.

[51] HAKALA, T., TOPPARI, J., KUZYK, A., PETTERSSON, M., TIKKANEN, H., KUNTTU, H., AND TÖRMÄ, P., *Vacuum Rabi splitting and strong-coupling dynamics for surface-plasmon polaritons and rhodamine 6G molecules*. Phys. Rev. Lett. **103** (2009) 053602.

[52] HANG, S., MOKTADIR, Z., AND MIZUTA, H., *Raman study of damage extent in graphene nanostructures carved by high energy helium ion beam*. Carbon **72** (2014) 233–241.

[53] HE, X., GAO, W., XIE, L., LI, B., ZHANG, Q., LEI, S., ROBINSON, J. M., HÁROZ, E. H., DOORN, S. K., WANG, W., *et al.*, *Wafer-scale monodomain films of spontaneously aligned single-walled carbon nanotubes*. Nat. Nanotechnol. (2016).

[54] HEBER, J., *Surfing the wave*. Nature **461** (2009) 720–722.

[55] HECHT, B., SICK, B., WILD, U. P., DECKERT, V., ZENOBI, R., MARTIN, O. J., AND POHL, D. W., *Scanning near-field optical microscopy with aperture probes: Fundamentals and applications*. J. Chem. Phys **112** (2000) 7761–7774.

[56] HEEGER, A. J., *Semiconducting and metallic polymers: the fourth generation of polymeric materials*. J. Phys. Chem. B **105** (2001) 8475–8491.

[57] HEINZE, S., TERSOFF, J., AND AVOURIS, P., *Electrostatic engineering of nanotube transistors for improved performance*. Appl. Phys. Lett. **83** (2003) 5038–5040.

[58] HEINZE, S., TERSOFF, J., MARTEL, R., DERYCKE, V., APPENZELLER, J., AND AVOURIS, P., *Carbon nanotubes as Schottky barrier transistors*. Phys. Rev. Lett. **89** (2002) 106801.

[59] HERSAM, M., *Progress towards monodisperse single-walled carbon nanotubes*. Nat. Nanotechnol. **3** (2008) 387–394.

[60] HUANG, Y. Y. AND TERENTJEV, E. M., *Dispersion of carbon nanotubes: mixing, sonication, stabilization, and composite properties*. Polymers **4** (2012) 275–295.

[61] IGARASHI, T., KAWAI, H., YANAGI, K., CUONG, N. T., OKADA, S., AND PICHLER, T., *Tuning Localized Transverse Surface Plasmon Resonance in Electricity-Selected Single-Wall Carbon Nanotubes by Electrochemical Doping*. Phys. Rev. Lett. **114** (2015) 176807.

[62] IIJIMA, S., *Helical microtubules of graphitic carbon*. Nature **354** (1991) 56–58.

[63] ITKIS, M. E., BORONDICS, F., YU, A., AND HADDON, R. C., *Bolometric infrared photoresponse of suspended single-walled carbon nanotube films*. Science **312** (2006) 413–416.

[64] JAVEY, A., GUO, J., WANG, Q., LUNDSTROM, M., AND DAI, H., *Ballistic carbon nanotube field-effect transistors*. Nature **424** (2003) 654–657.

[65] JHI, S., LOUIE, S., AND COHEN, M., *Electronic properties of oxidized carbon nanotubes*. Phys. Rev. Lett. **85** (2000) 1710–1713.

[66] JORIO, A., PIMENTA, M., SOUZA FILHO, A., SAITO, R., DRESSELHAUS, G., AND DRESSELHAUS, M., *Characterizing carbon nanotube samples with resonance Raman scattering*. New J. Phys. **5** (2003) 139.

[67] JU, L., GENG, B., HORNG, J., GIRIT, C., MARTIN, M., HAO, Z., BECHTEL, H. A., LIANG, X., ZETTL, A., SHEN, Y. R., *et al.*, *Graphene plasmonics for tunable terahertz metamaterials*. Nat. Nanotechnol. **6** (2011) 630–634.

[68] KANO, K., *Semiconductor devices* (Prentice Hall, 1998).

[69] KAROUSIS, N., TAGMATARCHIS, N., AND TASIS, D., *Current progress on the chemical modification of carbon nanotubes*. Chem. Rev. **110** (2010) 5366–5397.

[70] KATAURA, H., KUMAZAWA, Y., MANIWA, Y., UMEZU, I., SUZUKI, S., OHTSUKA, Y., AND ACHIBA, Y., *Optical properties of single-wall carbon nanotubes*. Synthetic Met. **103** (1999) 2555–2558.

[71] KAWAI, H., HASEGAWA, K., OYANE, A., NAITOH, Y., AND YANAGI, K., *Self-formation of highly aligned metallic, semiconducting and single chiral single-walled carbon nanotubes assemblies via a crystal template method*. Appl. Phys. Lett. **105** (2014) 093102.

[72] KAWATA, S., INOUYE, Y., AND VERMA, P., *Plasmonics for near-field nano-imaging and superlensing*. Nat. Photon. **3** (2009) 388–394.

[73] KNOCH, J. AND APPENZELLER, J., *Tunneling phenomena in carbon nanotube field-effect transistors*. Phys. Status Solidi A **205** (2008) 679–694.

[74] KRAMBERGER, C., HAMBACH, R., GIORGETTI, C., RÜMMELI, M., KNUPFER, M., FINK, J., BÜCHNER, B., REINING, L., EINARSSON, E., MARUYAMA, S., *et al.*, *Linear plasmon dispersion in single-wall carbon nanotubes and the collective excitation spectrum of graphene*. Phys. Rev. Lett. **100** (2008) 196803–196806.

[75] KRENN, J., DEREUX, A., WEEBER, J., BOURILLOT, E., LACROUTE, Y., GOUDONNET, J., SCHIDER, G., GOTSCHY, W., LEITNER, A., AUSSENEGG, F., *et al.*, *Squeezing the optical near-field zone by plasmon coupling of metallic nanoparticles*. Phys. Rev. Lett. **82** (1999) 2590.

[76] KRETSCHMANN, E. AND RAETHER, H., *Radiative decay of non radiative surface plasmons excited by light*. Z. Naturforsch. A **23** (1968) 2135–2136.

[77] KROTO, H. W., HEATH, J. R., O'BRIEN, S. C., CURL, R. F., SMALLEY, R. E., *et al.*, *C 60: buckminsterfullerene*. Nature **318** (1985) 162–163.

[78] LAKOWICZ, J. R., *Plasmonics in biology and plasmon-controlled fluorescence*. Plasmonics **1** (2006) 5–33.

[79] LECARUYER, P., CANVA, M., AND ROLLAND, J., *Metallic film optimization in a surface plasmon resonance biosensor by the extended Rouard method*. Appl. Optics **46** (2007) 2361–2369.

[80] LI, B., CAO, X., ONG, H. G., CHEAH, J. W., ZHOU, X., YIN, Z., LI, H., WANG, J., BOEY, F., HUANG, W., *et al.*, *All-Carbon Electronic Devices Fabricated by Directly Grown Single-Walled Carbon Nanotubes on Reduced Graphene Oxide Electrodes*. Adv. Mater. **22** (2010) 3058–3061.

[81] LI, X., CAI, W., AN, J., KIM, S., NAH, J., YANG, D., PINER, R., VELAMAKANNI, A., JUNG, I., TUTUC, E., *et al.*, *Large-area synthesis of high-quality and uniform graphene films on copper foils*. Science **324** (2009) 1312–1314.

[82] LIU, J., HE, W., HU, L., LIU, Z., ZHOU, H., WU, X., AND SUN, L., *Visible light detection using single-walled carbon nanotube film and gold nanoparticles or nanorods*. J. Appl. Phys. **107** (2010) 094311.

[83] LIU, P., SUN, Q., ZHU, F., LIU, K., JIANG, K., LIU, L., LI, Q., AND FAN, S., *Measuring the work function of carbon nanotubes with thermionic method*. Nano Lett. **8** (2008) 647–651.

[84] DE LOS ARCOS, T., OELHAFEN, P., AND MATHYS, D., *Optical characterization of alignment and effective refractive index in carbon nanotube films*. Nanotechnology **18** (2007) 265706.

[85] LOUWET, F., GROENENDAAL, L., DHAEN, J., MANCA, J., VAN LUPPEN, J., VERDONCK, E., AND LEENDERS, L., *PEDOT/PSS: synthesis, characterization, properties and applications*. Synthetic Met. **135** (2003) 115–117.

[86] MAGG, M., KADRIA-VILI, Y., OULEVEY, P., WEISMAN, R. B., AND BURGI, T., *Resonance Raman Optical Activity Spectra of Single-Walled Carbon Nanotube Enantiomers*. J. Phys. Chem. Lett. **7** (2016) 221–225.

[87] MAIER, S. A., *Plasmonics: fundamentals and applications* (Springer Science & Business Media, 2007).

[88] MAK, K. F., SFEIR, M. Y., WU, Y., LUI, C. H., MISEWICH, J. A., AND HEINZ, T. F., *Measurement of the optical conductivity of graphene*. Phys. Rev. Lett. **101** (2008) 196405.

[89] MARCUS, M., SIMMONS, J., CASTELLINI, O., HAMERS, R., AND ERIKSSON, M., *Photogating carbon nanotube transistors*. J. Appl. Phys. **100** (2006) 084306.

[90] MATSUI, T., VARDENYA, Z. V., AGRAWAL, A., NAHATA, A., AND MENON, R., *Resonantly-enhanced transmission through a periodic array of subwavelength apertures in heavily-doped conducting polymer films*. Appl. Phys. Lett. **88** (2006) 071101.

[91] MCPEAK, K. M., JAYANTI, S. V., KRESS, S. J., MEYER, S., IOTTI, S., ROSSINELLI, A., AND NORRIS, D. J., *Plasmonic films can easily be better: rules and recipes*. ACS Photonics **2** (2015) 326–333.

[92] MIE, G., *Beiträge zur Optik trüber Medien, speziell kolloidaler Metallösungen*. Ann. Phys. **330** (1908) 377–445.

[93] MIYAMOTO, Y., JINBO, N., NAKAMURA, H., RUBIO, A., AND TOMÁNEK, D., *Photodesorption of oxygen from carbon nanotubes*. Phys. Rev. B **70** (2004) 233408.

[94] MOISALA, A., NASIBULIN, A. G., AND KAUPPINEN, E. I., *The role of metal nanoparticles in the catalytic production of single-walled carbon nanotubes - a review*. J. Phys. Condens. Matter **15** (2003) S3011.

[95] MONTHIOUX, M. AND KUZNETSOV, V. L., *Who should be given the credit for the discovery of carbon nanotubes?* Carbon **44** (2006) 1621–1623.

[96] MORIMOTO, T. AND OKAZAKI, T., *Optical resonance in far-infrared spectra of multiwalled carbon nanotubes*. Appl. Phys. Express **8** (2015) 055101.

[97] MURAKAMI, Y., EINARSSON, E., EDAMURA, T., AND MARUYAMA, S., *Polarization dependence of the optical absorption of single-walled carbon nanotubes*. Phys. Rev. Lett. **94** (2005) 087402.

[98] MUSTONEN, T., KORDÁS, K., SAUKKO, S., TÓTH, G., PENTTILÄ, J. S., HELISTÖ, P., SEPPÄ, H., AND JANTUNEN, H., *Inkjet printing of transparent and conductive patterns of single-walled carbon nanotubes and PEDOT-PSS composites*. Phys. Status Solidi B **244** (2007) 4336–4340.

[99] NANOINTEGRIS, *Carbon Nanotubes Technical Data Sheet*, `http://www.nanointegris.com/skin/frontend/default/nano/downloads/Carbon%20Nanotubes%20Technical%20Data%20Sheet.pdf` (2012 (accessed 2016-02-04)).

[100] NARDES, A. M., KEMERINK, M., JANSSEN, R. A., BASTIAANSEN, J. A., KIGGEN, N. M., LANGEVELD, B. M., VAN BREEMEN, A. J., AND DE KOK, M. M., *Microscopic understanding of the anisotropic conductivity of PEDOT: PSS thin films*. Adv. Mater. **19** (2007) 1196–1200.

[101] NERKARARYAN, K. V., *Superfocusing of a surface polariton in a wedge-like structure*. Phys. Lett. A **237** (1997) 103–105.

[102] NOVOSELOV, K. S., GEIM, A. K., MOROZOV, S. V., JIANG, D., ZHANG, Y., DUBONOS, S. V., GRIGORIEVA, I. V., AND FIRSOV, A. A., *Electric field effect in atomically thin carbon films*. Science **306** (2004) 666–669.

[103] NOVOTNY, L. AND HECHT, B., *Principles of nano-optics* (Cambridge University Press, 2012).

[104] NUGRAHA, A., SAITO, R., SATO, K., ARAUJO, P., JORIO, A., AND DRESSELHAUS, M., *Dielectric constant model for environmental effects on the exciton energies of single wall carbon nanotubes*. Appl. Phys. Lett. **97** (2010) 091905.

[105] OBERLIN, A., ENDO, M., AND KOYAMA, T., *High resolution electron microscope observations of graphitized carbon fibers*. Carbon **14** (1976) 133–135.

[106] OGIEGLO, W., WORMEESTER, H., EICHHORN, K.-J., WESSLING, M., AND BENES, N. E., *In situ ellipsometry studies on swelling of thin polymer films: A review*. Prog. Polym. Sci. **42** (2015) 42–78.

[107] OSAWA, E., *Superaromaticity*. Kagaku **25** (1970) 101.

[108] PARK, Y. R., KIM, W.-J., KO, M. J., MIN, N. K., AND LEE, C. J., *Investigation of ultraviolet optical properties of semiconducting-enriched and metal-enriched single-walled carbon nanotube networks using spectroscopic ellipsometry*. Nanoscale **4** (2012) 6532–6536.

[109] PATIL, A., HEEGER, A., AND WUDL, F., *Optical properties of conducting polymers*. Chem. Rev. **88** (1988) 183–200.

[110] PETTERSSON, L. A., GHOSH, S., AND INGANÄS, O., *Optical anisotropy in thin films of poly (3, 4-ethylenedioxythiophene)–poly (4-styrenesulfonate)*. Org. Electron. **3** (2002) 143–148.

[111] QIU, X., FREITAG, M., PEREBEINOS, V., AND AVOURIS, P., *Photoconductivity spectra of single-carbon nanotubes: Implications on the nature of their excited states*. Nano Lett. **5** (2005) 749–752.

[112] RADUSHKEVICH, L. AND LUKYANOVICH, V., *About the structure of carbon formed by thermal decomposition of carbon monoxide on iron substrate*. J. Phys. Chem. (Moscow) **26** (1952) 88–95.

[113] RAETHER, H., *Surface Plasmons on Smooth and Rough Surfaces and on Gratings*. Springer Tr. Mod. Phys. **111** (1988).

[114] REDDICK, R., WARMACK, R., AND FERRELL, T., *New form of scanning optical microscopy*. Phys. Rev. B **39** (1989) 767.

[115] RINKIÖ, M., JOHANSSON, A., ZAVODCHIKOVA, M. Y., TOPPARI, J. J., NASIBULIN, A. G., KAUPPINEN, E. I., AND TÖRMÄ, P., *High-yield of memory elements from carbon nanotube field-effect transistors with atomic layer deposited gate dielectric*. New J. Phys. **10** (2008) 103019.

[116] RYCHEN, J., *Combined low-temperature scanning probe microscopy and magnetotransport experiments for the local investigation of mesoscopic systems*, Ph.D. thesis, Naturwissenschaften ETH Zürich, Nr. 14119 (2001).

[117] SAITO, R., HOFMANN, M., DRESSELHAUS, G., JORIO, A., AND DRESSELHAUS, M., *Raman spectroscopy of graphene and carbon nanotubes*. Adv. Phys. **60** (2011) 413–550.

[118] SARYCHEV, A., SHVETS, G., AND SHALAEV, V., *Magnetic plasmon resonance*. Phys. Rev. E **73** (2006) 036609–036618.

[119] SASAKI, K.-I., MURAKAMI, S., AND YAMAMOTO, H., *Theory of intraband plasmons in doped carbon nanotubes: Rolled surface-plasmons of graphene*. Appl. Phys. Lett. **108** (2016) 163109.

[120] SATO, K., SAITO, R., JIANG, J., DRESSELHAUS, G., AND DRESSELHAUS, M., *Discontinuity in the family pattern of single-wall carbon nanotubes*. Phys. Rev. B **76** (2007) 195446.

[121] SCHULLER, J. A., BARNARD, E. S., CAI, W., JUN, Y. C., WHITE, J. S., AND BRONGERSMA, M. L., *Plasmonics for extreme light concentration and manipulation*. Nat. Mater. **9** (2010) 193–204.

[122] SHARMA, R., LEE, C. Y., CHOI, J. H., CHEN, K., AND STRANO, M. S., *Nanometer positioning, parallel alignment, and placement of single anisotropic nanoparticles using hydrodynamic forces in cylindrical droplets*. Nano Lett. **7** (2007) 2693–2700.

[123] SHI, L., ROHRINGER, P., SUENAGA, K., NIIMI, Y., KOTAKOSKI, J., MEYER, J. C., PETERLIK, H., WANKO, M., CAHANGIROV, S., RUBIO, A., *et al., Confined linear carbon chains as a route to bulk carbyne*. Nat. Mater. **15** (2016) 634–639.

[124] SHI, Z., HONG, X., BECHTEL, H. A., ZENG, B., MARTIN, M. C., WATANABE, K., TANIGUCHI, T., SHEN, Y.-R., AND WANG, F., *Observation of a Luttinger-liquid plasmon in metallic single-walled carbon nanotubes*. Nat. Photon. **9** (2015) 515–519.

[125] SHUBA, M., PADDUBSKAYA, A., PLYUSHCH, A., KUZHIR, P., SLEPYAN, G., MAKSIMENKO, S., KSENEVICH, V., BUKA, P., SELIUTA, D., KASALYNAS, I., *et al., Experimental evidence of localized plasmon resonance in composite materials containing single-wall carbon nanotubes*. Phys. Rev. B **85** (2012) 165435–165440.

[126] STANDRIDGE, S. D., SCHATZ, G. C., AND HUPP, J. T., *Toward plasmonic solar cells: protection of silver nanoparticles via atomic layer deposition of TiO2*. Langmuir **25** (2009) 2596–2600.

[127] STEELE, J. M., LIU, Z., WANG, Y., AND ZHANG, X., *Resonant and non-resonant generation and focusing of surface plasmons with circular gratings*. Opt. Express **14** (2006) 5664–5670.

[128] STEFANIUK, T., WRÓBEL, P., GÓRECKA, E., AND SZOPLIK, T., *Optimum deposition conditions of ultrasmooth silver nanolayers*. Nanoscale Research Letters **9** (2014) 1.

[129] STILES, P. L., DIERINGER, J. A., SHAH, N. C., AND VAN DUYNE, R. P., *Surface-enhanced Raman spectroscopy*. Annu. Rev. Anal. Chem. **1** (2008) 601–626.

[130] TAKAHARA, J., YAMAGISHI, S., TAKI, H., MORIMOTO, A., AND KOBAYASHI, T., *Guiding of a one-dimensional optical beam with nanometer diameter*. Opt. Lett. **22** (1997) 475–477.

[131] TAN, P., ROZHIN, A., HASAN, T., HU, P., SCARDACI, V., MILNE, W., AND FERRARI, A., *Photoluminescence spectroscopy of carbon nanotube bundles: Evidence for exciton energy transfer*. Phys. Rev. Lett. **99** (2007) 137402.

[132] TANS, S. J., VERSCHUEREN, A. R., AND DEKKER, C., *Room-temperature transistor based on a single carbon nanotube*. Nature **393** (1998) 49–52.

[133] TESSONNIER, J.-P. AND SU, D. S., *Recent progress on the growth mechanism of carbon nanotubes: a review*. ChemSusChem **4** (2011) 824–847.

[134] THOMSEN, C. AND REICH, S., *Double resonant Raman scattering in graphite*. Phys. Rev. Lett. **85** (2000) 5214.

[135] TÖRMÄ, P. AND BARNES, W. L., *Strong coupling between surface plasmon polaritons and emitters: a review*. Rep. Prog. Phys. **78** (2015) 013901.

[136] TUUKKANEN, S., HOIKKANEN, M., POIKELISPÄÄ, M., HONKANEN, M., VUORINEN, T., KAKKONEN, M., VUORINEN, J., AND LUPO, D., *Stretching of solution processed carbon nanotube and graphene nanocomposite films on rubber substrates*. Synthetic Met. **191** (2014) 28–35.

[137] TUUKKANEN, S., JULIN, T., RANTANEN, V., ZAKRZEWSKI, M., MOILANEN, P., LILJA, K. E., AND RAJALA, S., *Solution-processible electrode materials for a heat-sensitive piezoelectric thin-film sensor*. Synthetic Met. **162** (2012) 1987–1995.

[138] VALENTINI, L., ARMENTANO, I., PUGLIA, D., LOZZI, L., SANTUCCI, S., AND KENNY, J., *A deeper understanding of the photodesorption mechanism of aligned carbon nanotube thin films by impedance spectroscopy*. Thin Solid Films **449** (2004) 105–112.

[139] VUORINEN, T., ZAKRZEWSKI, M., RAJALA, S., LUPO, D., VANHALA, J., PALOVUORI, K., AND TUUKKANEN, S., *Printable, transparent, and flexible touch panels working in sunlight and moist environments*. Adv. Funct. Mater. **24** (2014) 6340–6347.

[140] WALLACE, P. R., *The band theory of graphite*. Phys. Rev. **71** (1947) 622.

[141] WANG, F., DUKOVIC, G., BRUS, L., AND HEINZ, T., *The optical resonances in carbon nanotubes arise from excitons*. Science **308** (2005) 838–841.

[142] WANG, F., ZHANG, Y., TIAN, C., GIRIT, C., ZETTL, A., CROMMIE, M., AND SHEN, Y. R., *Gate-variable optical transitions in graphene*. Science **320** (2008) 206–209.

[143] WANG, Y., ALSMEYER, D. C., AND MCCREERY, R. L., *Raman spectroscopy of carbon materials: structural basis of observed spectra*. Chem. Mater. **2** (1990) 557–563.

[144] WANG, Y., WANG, X., WU, Q., HE, X.-J., GUI, T.-L., AND TONG, Y.-J., *Surface Plasmon Resonant THz Wave Transmission on Carbon Nanotube Film*. Plasmonics **7** (2012) 411–415.

[145] WEIGHTMAN, P., MARTIN, D., COLE, R., AND FARRELL, T., *Reflection anisotropy spectroscopy*. Rep. Prog. Phys. **68** (2005) 1251.

[146] WEST, P. R., ISHII, S., NAIK, G. V., EMANI, N. K., SHALAEV, V. M., AND BOLTASSEVA, A., *Searching for better plasmonic materials*. Laser Photon. Rev. **4** (2010) 795–808.

[147] XIONG, X., JABERANSARI, L., HAHM, M. G., BUSNAINA, A., AND JUNG, Y. J., *Building highly organized single-walled-carbon-nanotube networks using template-guided fluidic assembly*. Small **3** (2007) 2006–2010.

[148] YAN, H., LI, X., CHANDRA, B., TULEVSKI, G., WU, Y., FREITAG, M., ZHU, W., AVOURIS, P., AND XIA, F., *Tunable infrared plasmonic devices using graphene/insulator stacks*. Nat. Nanotechnol. **7** (2012) 330–334.

[149] YAN, H., LI, Z., LI, X., ZHU, W., AVOURIS, P., AND XIA, F., *Infrared spectroscopy of tunable Dirac terahertz magneto-plasmons in graphene*. Nano Lett. **12** (2012) 3766–3771.

[150] YANAGI, K., MORIYA, R., YOMOGIDA, Y., TAKENOBU, T., NAITOH, Y., ISHIDA, T., KATAURA, H., MATSUDA, K., AND MANIWA, Y., *Electrochromic Carbon Electrodes: Controllable Visible Color Changes in Metallic Single-Wall Carbon Nanotubes*. Adv. Mater. **23** (2011) 2811–2814.

[151] YOMOGIDA, Y., TANAKA, T., ZHANG, M., YUDASAKA, M., WEI, X., AND KATAURA, H., *Industrial-scale separation of high-purity single-chirality single-wall carbon nanotubes for biological imaging*. Nat. Commun. **7** (2016) 12056.

[152] YOO, D., KIM, J., AND KIM, J. H., *Direct synthesis of highly conductive poly (3, 4-ethylenedioxythiophene): poly (4-styrenesulfonate)(PEDOT: PSS)/graphene composites and their applications in energy harvesting systems*. Nano Res. **7** (2014) 717–730.

[153] YOO, D., KIM, J., LEE, S. H., CHO, W., CHOI, H. H., KIM, F. S., AND KIM, J. H., *Effects of one-and two-dimensional carbon hybridization of PEDOT:PSS on the power factor of polymer thermoelectric energy conversion devices*. J. Mater. Chem. A **3** (2015) 6526–6533.

[154] ZAKHARKO, Y., GRAF, A., SCHIESSL, S. P., HÄHNLEIN, B., PEZOLDT, J., GATHER, M. C., AND ZAUMSEIL, J., *Broadband Tunable, Polarization-Selective and Directional Emission of (6, 5) Carbon Nanotubes Coupled to Plasmonic Crystals*. Nano Lett. **16** (2016) 3278–3284.

[155] ZAYATS, A. V., SMOLYANINOV, I. I., AND MARADUDIN, A. A., *Nano-optics of surface plasmon polaritons*. Phys. Rep. **408** (2005) 131–314.

[156] ZEEVI, G., SHLAFMAN, M., TABACHNIK, T., ROGACHEVSKY, Z., RECHNITZ, S., GOLDSHTEIN, I., SHLAFMAN, S., GORDON, N., ALCHANATI, G., ITZHAK, M., *et al., Automated circuit fabrication and direct characterization of carbon nanotube vibrations*. Nat. Commun. **7** (2016) 12153.

[157] ZHANG, J., BOYD, A., TSELEV, A., PARANJAPE, M., AND BARBARA, P., *Mechanism of NO2 detection in carbon nanotube field effect transistor chemical sensors*. Appl. Phys. Lett. **88** (2006) 123112.

[158] ZHANG, Q., HÁROZ, E. H., JIN, Z., REN, L., WANG, X., ARVIDSON, R. S., LÜTTGE, A., AND KONO, J., *Plasmonic nature of the terahertz conductivity peak in single-wall carbon nanotubes*. Nano Lett. **13** (2013) 5991–5996.

[159] ZHAO, J. AND XIE, R., *Electronic and photonic properties of doped carbon nanotubes.* J. Nanosci. Nanotechno. **3** (2003) 459–478.

[160] ZHAO, X., LIU, Y., INOUE, S., SUZUKI, T., JONES, R., AND ANDO, Y., *Smallest carbon nanotube is 3 Å in diameter*. Phys. Rev. Lett. **92** (2004) 125502.

[161] ZHOU, C., WANG, S., SUN, J., WEI, N., YANG, L., ZHANG, Z., LIAO, J., AND PENG, L.-M., *Plasmonic enhancement of photocurrent in carbon nanotube by Au nanoparticles*. Appl. Phys. Lett. **102** (2013) 103102.

[162] ZHU, X., WANG, W., YAN, W., LARSEN, M. B., BØGGILD, P., PEDERSEN, T. G., XIAO, S., ZI, J., AND MORTENSEN, N. A., *Plasmon–phonon coupling in large-area graphene dot and antidot arrays fabricated by nanosphere lithography*. Nano Lett. **14** (2014) 2907–2913.

A.I

Surface plasmon effects on carbon nanotube field effect transistors

T. Isoniemi,[1] A. Johansson,[1] T. K. Hakala,[1,a)] M. Rinkiö,[1,2] P. Törmä,[2] J. J. Toppari,[1,b)] and H. Kunttu[3]

[1]*Nanoscience Center, Department of Physics, University of Jyväskylä, P.O. Box 35 (YN), FIN-40014 Jyväskylä, Finland*

[2]*Department of Applied Physics, Aalto University School of Science, P.O. Box 15100, FIN-00076 AALTO, Finland*

[3]*Nanoscience Center, Department of Chemistry, University of Jyväskylä, P.O. Box 35 (YN), FIN-40014 Jyväskylä, Finland*

(Received 19 April 2011; accepted 28 June 2011; published online 19 July 2011)

Herein, we experimentally demonstrate surface plasmon polariton (SPP) induced changes in the conductivity of a carbon nanotube field effect transistor (CNT FET). SPP excitation is done via Kretschmann configuration while the measured CNT FET is situated on the opposite side of the metal layer away from the laser, but within reach of the launched SPPs. We observe a shift of ~0.4 V in effective gate voltage. SPP-intermediated desorption of physisorbed oxygen from the device is discussed as a likely explanation of the observed effect. This effect is visible even at low SPP intensities and within a near-infrared range. © *2011 American Institute of Physics*. [doi:10.1063/1.3614543]

Field effect transistors (FETs) utilizing carbon nanotubes (CNTs) as their conductance channel have possible applications, among others, as chemical[1,2] and optical sensors[3] as well as in photoelectronics.[4] Chemical sensing is generally based on adsorption or desorption of different molecular species that alter the electrical response of semiconducting single-walled (SW) CNTs (Refs. 1 and 5) (as well as graphene[6]). In ambient conditions, specifically oxygen and water vapor have been shown to significantly influence CNT FETs,[7,8] even though most of the oxygen is only physisorbed on the SWCNT via van der Waals interactions.[9] On the other hand, photoexcitation of a SWCNT, which is especially important for photoelectrical applications, can induce several different effects in its electrical transport properties.[3–5] While the direct electron-hole generation is the most desired effect in photoelectronics, another usually even more important and widely studied effect is due to photodesorption of atmospheric molecules.[5,8,10,11] The photodesorption is strongest in the UV range and usually negligible in near-IR.[5]

Surface plasmon polaritons (SPPs) are coupled modes of electromagnetic waves and oscillations of free electrons in a metal surface. They can be considered as two-dimensional light bound to a metal-dielectric interface, however, with all the properties modified by the subwavelength confinement of these optical fields.[12,13] Thus, SPPs offer fascinating prospects for photoelectronics. For example, a huge field enhancement near the interface produced by the confinement has been widely utilized in surface enhanced Raman spectroscopy.[14] In this letter, we utilize SPPs to "illuminate" the CNT FET, which leads to a significant effect on its charge transfer properties. Surface plasmons have been shown to cause desorption on metal surfaces.[15] Here, the observed effect can also be explained by the desorption of oxygen induced by the SPP illumination. Contrary to far-field induced photodesorption, the effect observed here is visible at low intensities and even in near-IR.

Schematics of the experimental setup and an AFM image of the CNT FET measured are shown in Fig. 1. SPPs are launched in the Kretschmann configuration, where the incoming light at the resonant angle couples to SPPs on the outer surface of a thin metal film deposited on an optically transparent substrate.[16,17] A light source was collimated by two narrow slits and incident on the half-cylinder prism through a polarizer. Photons are coupled into SPPs on the sample at the bottom of the prism when the incoming beam is *p*-polarized, while the SPP excitation is turned off when the polarizer is turned 90°, producing an *s*-polarized ray.[16]

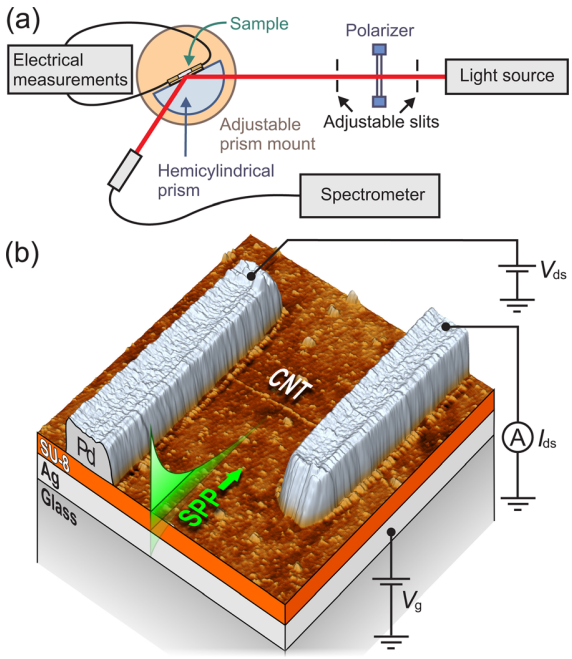

FIG. 1. (Color online) (a) Schematics of the experimental setup. (b) AFM image of the device. Edge dimensions are 2.5 μm and the SPPs are excited on the interface between SU-8 and silver in the direction of the arrow.

a)Present address: School of Engineering and Applied Sciences, Harvard University, Cambridge, Massachusetts 02138, USA.
b)Electronic mail: j.jussi.toppari@jyu.fi.

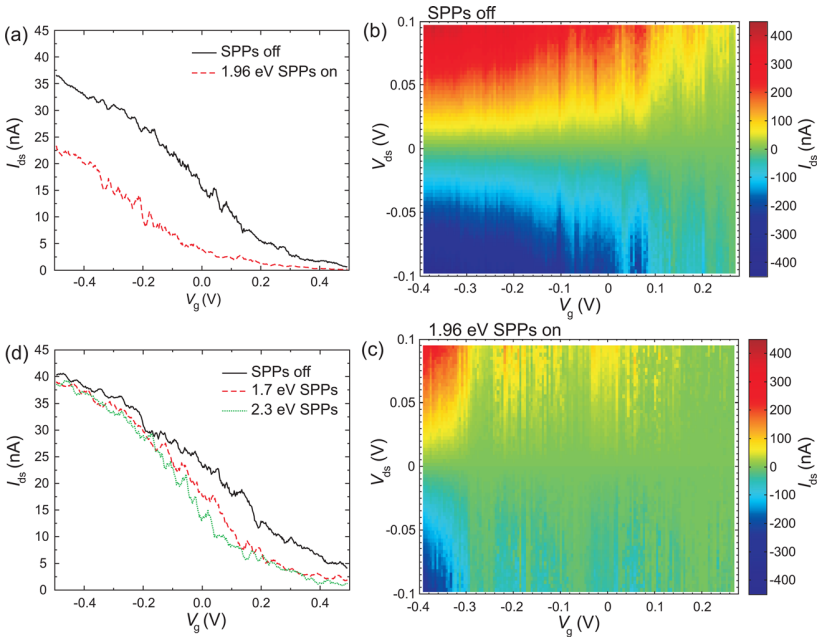

FIG. 2. (Color online) (a) Gate voltage sweeps with SPPs on and off. Four traces were averaged for each curve to decrease the noise level (negligible hysteresis). $V_{ds} = 10$ mV. (b) Drain-source current as a function of V_g and V_{ds}. 1.96 eV SPPs are switched off by polarization. V_{ds} is the fast scan axis (23 s for one line) and V_g is the slow scan axis. (c) A corresponding measurement for the same device with SPPs switched on. (d) V_g sweeps with excitation by white light and plasmon energy adjusted with the angle of incidence. 1.7 eV excitation angle was used in the measurement with SPPs off. $V_{ds} = 10$ mV.

This is used in the measurements as a control for possible effects due to direct light excitation; even though the sample is illuminated on the other side of the metal film compared to the CNT FET. The excited SPPs travel to the CNT FET perpendicular to the SWCNT, as shown in Fig. 1(b).

Samples were produced on a 1 cm^2 glass slide. For SPPs, a 63 nm thick and 1 mm wide silver strip was evaporated on the glass followed by spin-coating with diluted SU-8 2025 (MicroChem) resist. The resulting 50 nm thick cured SU-8 layer acts as a dielectric between the CNT circuit and the Ag strip, which doubles as a back gate. Photolithography and electron beam lithography (EBL) were used to produce palladium electrodes and alignment markers on the SU-8 surface.[18]

Commercial SWCNTs (Nanocyl S.A.) were spinned from a 1,2-dichloroethane suspension on the sample surface after breaking up bundles with sonication and located in relation to the alignment markers by AFM scans.[18] Finally, 84 nm thick Pd electrodes completing the CNT circuit were fabricated with EBL and the sample was connected to the setup.

Circularly polarized 633 nm (1.96 eV) HeNe laser (Uniphase 1125) was used as a light source producing a power density of ~700 mW/cm^2 on the prism after polarization. The incident beam had a spot size of 0.8 mm in diameter, pointed at the section of the Ag film where on the opposite side, the CNT FET is located. Plasmon resonance for the beam occurred at an angle of incidence of 62°, and the intensity of the SPPs produced to the Ag/SU-8 interface was approximately 110 mW/cm^2 based on the measured reflected intensity.[18] The exposed length of the 2.3 ± 0.7 nm thick SWCNT was 1 μm [see Fig. 1(b)].

The current, I_{ds}, flowing through the channel of the CNT FET was simultaneously measured during excitation by applying a drain-source voltage, V_{ds}, and a gate voltage, V_g. The CNT FET was initially measured with the *s*-polarized beam (no SPPs). It was found to have a *p*-type transistor response [see Fig. 2(a)], which is typical for devices with Pd contacts in ambient conditions.[19] Gate voltages greater than ± 0.5 V were not used due to the limited durability of the SU-8 layer. Notable is that the CNT FETs made with an SU-8 dielectric layer showed almost no hysteresis in the gate sweep curves (not shown).[20] When the laser beam was set to allow SPP excitation (*p*-polarized), the current response is suppressed and shifted to the left in Fig. 2(a). The contour plots in Figures 2(b) and 2(c) show clearly that a shift of about 0.4 V in effective gate voltage has taken place when turning the polarization of the laser 90°.

The temporal current response, I_{ds}, with a constant V_{ds} and V_g, is slow both after turning the SPPs on, inducing a drop in the conductance, and when the device is recovering after turning SPPs off. We suggest that photoinduced desorption and subsequent adsorption of molecules on the CNT FET explain the results. A likely candidate is O_2, which has been shown to spontaneously *p*-dope CNTs when exposed to air.[2,5,8] We cannot rule out the possibility of desorption of other molecules present in ambient conditions. However, oxygen has been shown to have the strongest influence.[8] The time dependence in Fig. 3 conforms well to an exponential fit in both directions, with time constants of 131 ± 3 s and 343 ± 3 s for the desorption and adsorption,[18] respectively, while there is no response in current to the laser excitation when it is not producing SPPs. The observed desorption rate is faster than measured for far field photodesorption with the same wavelength,[5] even when taking into account our higher intensity. This is consistent with the observations on the plasmon stimulated desorption on metal,[15] indicating SPP induced rate enhancement.

To study the energy dependence, the device was excited with a white light source, i.e., a tungsten-halogen lamp, and the energy of the excited SPPs was adjusted by the angle of incidence. Figure 2(d) shows the response for SPPs of two different approximate energies,[18] compared to no SPPs. The overall effect is much smaller than observed with laser due to the lower intensity of the light source, i.e., 7 mW/cm^2. Also, it should be noted that the produced SPPs have a Gaussian spectrum centered at the resonance wavelength. The intensity coupled to SPPs was ~20 μW/cm^2 for both green

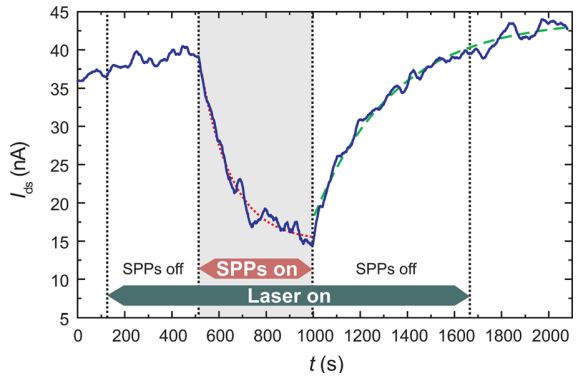

FIG. 3. (Color online) A typical measurement of the current response to laser exposure and SPP excitation controlled by polarization. Exponential fits are provided for desorption (dotted) and adsorption (dashed). $V_g = -0.4$ V, $V_{ds} = 10$ mV.

(2.3 eV) and near-infrared (1.7 eV) excitation.[18] We note that all these excitation energies are significantly higher than the binding energy of physisorbed oxygen, which is about 0.25 eV.[21] However, as seen from the figure, the response was slightly larger with higher plasmon energy, which is expected behavior for a photodesorption effect.[5]

Direct photocurrent due to electron-hole–pair creation would give the opposite effect, a fast increase in the current response, which at no point was observed.[3,22] However, the polarization of the SPPs being perpendicular to the axis of the CNT can explain this, since the photocurrent generation is maximized for light linearly polarized along the length of the CNT.[3] Also, highest response is at energies corresponding to the van Hove singularities,[23] so the effect should be minimal in these measurements.

If the substrate is a semiconductor such as Si, a photovoltage can also be generated at the interface between the backgate and the dielectric,[24] producing a shift in the effective gate voltage. Here, the use of a metal backgate prevents this effect, as evidenced by the lack of response for *s*-polarized laser. Direct heating of the sample by the laser is not affecting the conductivity of the CNT FET, as can be seen in Fig. 3. Neither can heating by SPPs be the reason for the observations; even a conservative estimation of temperature change in the device is less than 1 K, changing the conductivity less than 1%.[18] Note also that such scaling of the resistance could not explain the observed shift in effective gate voltage.[25,26] In addition, it has been shown that CNTs well connected to the substrate do not show an appreciable increase in temperature for incident far-field light power densities up to 100 kW/cm^2.[4]

The exact place of the molecular photodesorption, i.e., either at the CNT-metal contact region or along the CNT itself, is widely disputed.[2] The switching properties of CNT FETs are generally dominated by the response of the CNT-metal contact region, resulting in a Schottky-barrier transistor instead of a bulk-switching transistor.[4,27] Some studies point to strongest chemical activity on the CNT-metal contact,[11] but others show doping effects of the SWCNT itself[19] or are otherwise contradicting the idea of oxygen modifying the Schottky barrier via the electrode metal work function.[28] Yet, CNT FETs connected with Pd electrodes are shown to have lower effect, if any at all, on the desorption on the CNT-metal interface region.[19] From our data, it cannot be determined whether the desorption happens on the CNT or the CNT-metal contacts, and what type of desorption process is in question. Even though AFM imaging did not reveal obvious defects in the CNT, the processing with ultrasonication could have introduced them, providing possibly more active sites for molecular adsorption directly to SWCNT.

In summary, we demonstrated that 1.96 eV SPPs propagating at an interface 50 nm below the active region of a *p*-type CNT FET significantly modulate its conductivity and induce a 0.4 V shift in the effective gate voltage. The conductivity diminishing at a slow rate in response to the SPP excitation, as well as the decreasing of the effect with lower SPP energy can be explained by desorption of physisorbed molecules, most likely oxygen. The effect was observed even at low intensities and in near-IR, which is contrary to direct photodesorption.

This work was supported by the Academy of Finland (Project Nos. 135193, 218182, 130039, 213362, 217045, 135000, 141039) and conducted (see www.esf.org/euryi) as part of a EURYI scheme grant.

[1]D. Kauffman and A. Star, Angew. Chem. Int. Ed. **47**, 6550 (2008).
[2]P. Bondavalli, P. Legagneux, and D. Pribat, Sens. Actuators, B **140**, 304 (2009).
[3]M. Freitag, Y. Martin, J. A. Misewich, R. Martel, and P. Avouris, Nano Lett. **3**, 1067 (2003).
[4]P. Avouris, J. Chen, M. Freitag, V. Perebeinos, and J. Tsang, Phys. Status Solidi B **243**, 3197 (2006).
[5]R. Chen, N. Franklin, J. Kong, J. Cao, T. Tombler, Y. Zhang, and H. Dai, Appl. Phys. Lett. **79**, 2258 (2001).
[6]Y. Shi, W. Fang, K. Zhang, W. Zhang, and L. Li, Small **5**, 2005 (2009).
[7]D. McClain, N. Thomas, S. Youkey, R. Schaller, J. Jiao, and K. O'Brien, Carbon **47**, 1493 (2009).
[8]P. Collins, K. Bradley, M. Ishigami, and A. Zettl, Science **287**, 1801 (2000).
[9]H. Ulbricht, G. Moos, and T. Hertel, Phys. Rev. B **66**, 75404 (2002).
[10]D. Kang, N. Park, J. Hyun, E. Bae, J. Ko, J. Kim, and W. Park, Appl. Phys. Lett. **86**, 093105 (2005).
[11]M. Shim and G. Siddons, Appl. Phys. Lett. **83**, 3564 (2003).
[12]W. L. Barnes, A. Dereux, and T. W. Ebbesen, Nature **424**, 824 (2003).
[13]A. V. Zayats, I. I. Smolyaninov, and A. A. Maradudin, Phys. Rep. **408**, 131 (2005).
[14]K. Kneipp, H. Kneipp, P. Corio, S. D. M. Brown, K. Shafer, J. Motz, L. T. Perelman, E. B. Hanlon, A. Marucci, G. Dresselhaus, and M. S. Dresselhaus, Phys. Rev. Lett. **84**, 3470 (2000).
[15]W. Hoheisel, K. Jungmann, M. Vollmer, R. Weidenauer, and F. Träger, Phys. Rev. Lett. **60**, 1649 (1988).
[16]L. Novotny and B. Hecht, *Principles of Nano-optics* (Cambridge University Press, Cambridge, 2006).
[17]T. K. Hakala, J. J. Toppari, A. Kuzyk, M. Pettersson, H. Tikkanen, H. Kunttu, and P. Törmä, Phys. Rev. Lett. **103**, 053602 (2009).
[18]See supplementary material at http://dx.doi.org/10.1063/1.3614543 for sample fabrication details and plasmon resonance data.
[19]M. Shim, J. Back, T. Ozel, and K. Kwon, Phys. Rev. B **71**, 205411 (2005).
[20]M. Rinkiö, A. Johansson, G. S. Paraoanu, and P. Törmä, Nano Lett. **9**, 643 (2009).
[21]S. Jhi, S. Louie, and M. Cohen, Phys. Rev. Lett. **85**, 1710 (2000).
[22]I. Levitsky and W. Euler, Appl. Phys. Lett. **83**, 1857 (2003).
[23]X. Qiu, M. Freitag, V. Perebeinos, and P. Avouris, Nano Lett. **5**, 749 (2005).
[24]M. Marcus, J. Simmons, O. Castellini, R. Hamers, and M. Eriksson, J. Appl. Phys. **100**, 084306 (2006).
[25]E. Pop, D. Mann, Q. Wang, K. Goodson, and H. Dai, Nano Lett. **6**, 96 (2006).
[26]M. Itkis, F. Borondics, A. Yu, and R. Haddon, Science **312**, 413 (2006).
[27]V. Vitale, A. Curioni, and W. Andreoni, J. Am. Chem. Soc. **130**, 5848 (2008).
[28]D. McClain, N. Thomas, S. Youkey, R. Schaller, J. Jiao, and K. O'Brien, IEEE Electron Device Lett. **31**, 156 (2010).

A.II

ship between experimental findings (a) and (b). It also seems to me that literature studies in general [10], and Han et al.'s article in particular [1], laid very little emphasis on the fact that XPS not only offers oxidation-state speciation and elemental quantitative analysis of the catalyst's chemistry, it directly probes the surface layers which are crucial both to understand the chemical reaction pathway through which the catalyst works, as well as to improve its performance.

Acknowledgement

I express my gratitude to Dr. Rosanna Larciprete for useful discussions.

REFERENCES

[1] Han F, Wang X, Lian J, Wang Y. The effect of Sn content on the electrocatalytic properties of Pt–Sn nanoparticles dispersed on graphene nanosheets for the methanol oxidation reaction. Carbon 2012;50(15):5498–504.
[2] Barr TL. Modern ESCA: The Principles and Practice of X-ray Photoelectron Spectroscopy. Boca Raton FLA: CRC Press; 1994.
[3] Dreyer DR, Park S, Christopher W, Bielawski CW, Ruoff RS. The chemistry of graphene oxide. Chem Soc Rev 2010;39(1):228–40.
[4] Condon EU, Shortley GH. The Theory of Atomic Spectra. Cambridge: Cambridge University Press; 1977. p. 122–4.
[5] Ono KL, Yuan B, Heinrich H, Roldan Cuenya B. Formation and thermal stability of platinum oxides on size-selected platinum nanoparticles: support effects. J Phys Chem C 2010;114(50):22119–33.
[6] Yang D-Q, Zhang G-X, Sacher E, José Yacamán, Elizondo N. Evidence of the interaction of evaporated Pt nanoparticles with variously treated surfaces of highly oriented pyrolytic graphite. J Phys Chem B 2006;110(50):8348–56.
[7] Wertheim GK. Shape of core-electron photoemission spectra from metals. Phys Rev B 1982;25(3):1987–9.
[8] Wang DN, Miller AC, Notis MR. XPS study of the oxidation behavior of the Cu_3Sn intermetallic compound at low temperatures. Surf Interface Anal 1996;24(2):127–32.
[9] Shukla A, Aricò A, El-Khatib K, Kim H, Antonucci P, Antonucci V. An X-ray photoelectron spectroscopic study on the effect of Ru and Sn additions to platinised carbons. Appl Surf Sci 1999;137(1–4):20–9.
[10] Antolini E, Gonzalez E. The electro-oxidation of carbon monoxide, hydrogen/carbon monoxide and methanol in acid medium on Pt–Sn catalysts for low-temperature fuel cells: a comparative review of the effect of Pt–Sn structural characteristics. Electrochim Acta 2010;56(1):1–14. and references therein.

Collective optical resonances in networks of metallic carbon nanotubes

T. Isoniemi [a], A. Johansson [a], J.J. Toppari [a,], H. Kunttu [b]*

[a] *Nanoscience Center, Department of Physics, P.O. Box 35 (YN), FI-40014 University of Jyväskylä, Finland*
[b] *Nanoscience Center, Department of Chemistry, P.O. Box 35 (YN), FI-40014 University of Jyväskylä, Finland*

ARTICLE INFO

Article history:
Received 4 February 2013
Accepted 4 July 2013
Available online 13 July 2013

ABSTRACT

We demonstrate that thin films of randomly oriented metallic single-walled carbon nanotubes possess optical resonances with significant dispersion. The resonances are observed in the Kretschmann configuration as minima in reflection spectra close to 400 nm and 700 nm wavelengths. The dispersions are visible only when the material is excited with *s*-polarized light, and most prominent in layers with thickness near 100 nm. We conclude that magnetic plasmon polaritons arising from intertube interactions are a likely explanation. Closeness of the M_{11} and M_{22} transition energies to the observed resonances points to a possible coupling with excitons.

Carbon nanotubes (CNTs) have gathered huge interest due to their unique mechanical and electric properties. However, they show great promise also for new optical nanostructures. Due to the van Hove singularities in their density of states, they have distinct optical resonances with excitonic characteristics [1]. In addition, CNTs may also possess plasmonic properties. In electron energy loss spectroscopy π-plasmons have been observed in unsorted single walled (SW)

* *Corresponding author.*
E-mail address: j.jussi.toppari@jyu.fi (J.J. Toppari).
0008-6223/$ - see front matter
http://dx.doi.org/10.1016/j.carbon.2013.07.018

CNTs showing a prominent dispersion between the energies 5 and 10 eV; and $\pi + \sigma$-plasmons appearing similarly at 15–25 eV [2].

Despite a variety of theoretical predictions (see [3] and references therein), few experimental results exist on optical plasmons in CNT materials. Surface plasmon polaritons (SPPs) excited by a commonly used total internal reflection (TIR) setup, the Kretschmann configuration (see Fig. 1a), have been shown to couple through an array of vertical multi-walled CNTs [4]. In addition, composite materials of SWCNTs can show localized surface plasmon resonances (LSPRs) dependent on tube length [5].

In this article we demonstrate dispersive and polarization dependent optical modes excited via the Kretschmann configuration within a randomly oriented planar network of metallic SWCNTs.

The used SWCNT materials were purchased from NanoIntegris Inc. (Menlo Park, CA, USA), and consisted of arc discharge produced SWCNTs with a mean diameter of 1.4 nm. The SWCNTs had been enriched to either high metallic or

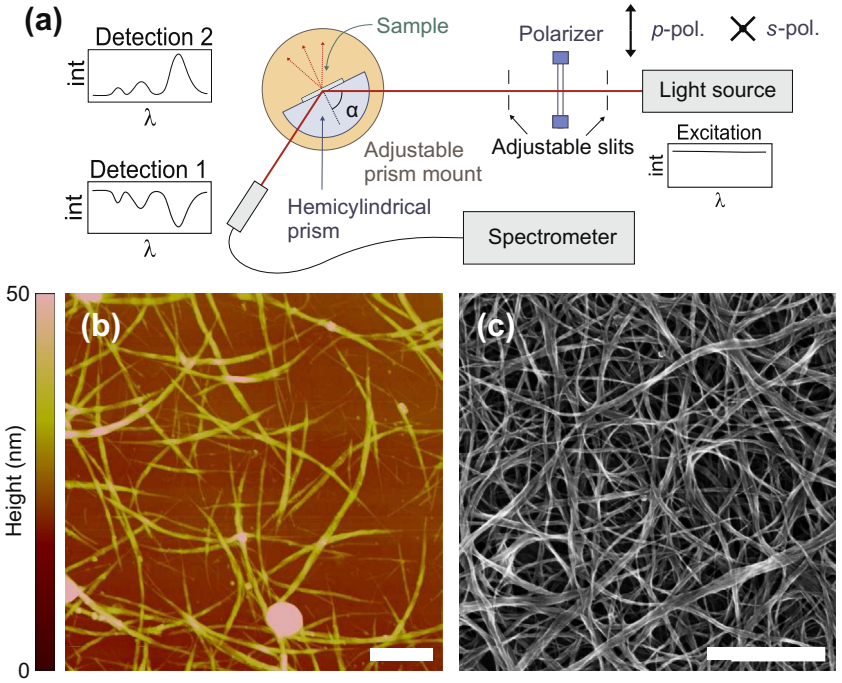

Fig. 1 – (a) Schematics of the measurement setup utilizing Kretschmann configuration. (b) Atomic force microscope (AFM) image of a typical thin network of metallic SWCNTs. (c) Scanning electron micrograph of a thick network of metallic SWCNTs. All the scale bars are 500 nm.

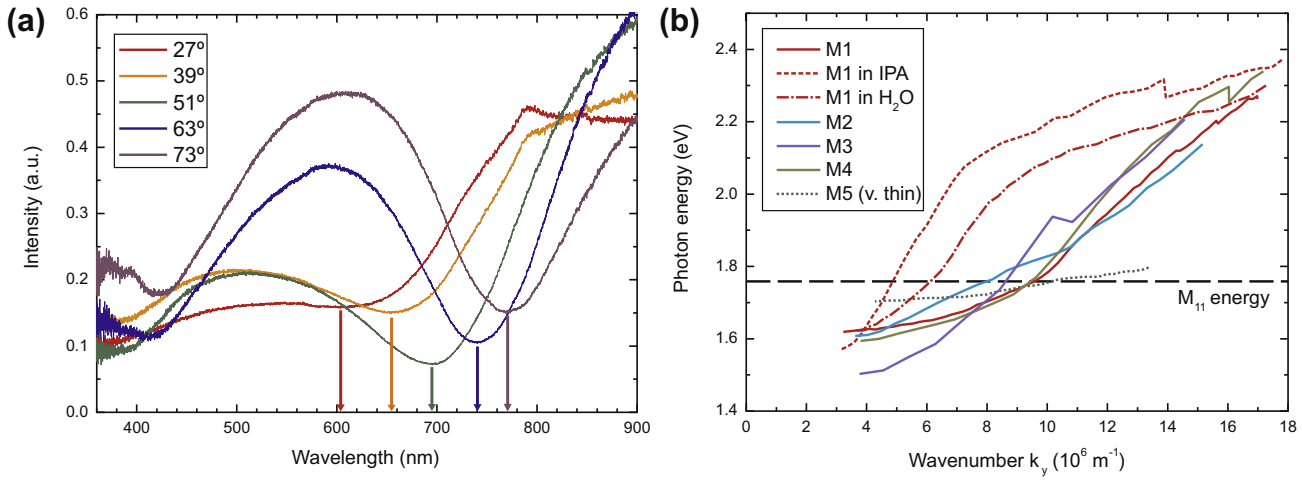

Fig. 2 – (a) Reflection spectra from a metallic SWCNT network (sample M2). Excitation angles are given relative to the sample normal. (b) Dispersion curves, i.e., minimum of the dip in the reflectance spectrum as a function of a vertical component of the wavevector, k_y, measured from various metallic SWCNT film samples. M1 is measured in air, as well as embedded in isopropanol and water; others only in air. Samples M1–M4 are roughly 100 nm thick, while M5 is only 5 nm thick.

semiconducting concentrations (98%) using density gradient ultracentrifugation. The material was deposited on glass slides as described in the Supplementary material. The formed layers consist of randomly oriented CNT networks consisting mainly of bundles, as seen in Fig. 1b and c.

Reflection spectroscopy was performed on the SWCNT networks, using the Kretschmann configuration with a varying excitation angle and a collimated white light source, as shown in Fig. 1a and Supplementary material. The measurements with *s*-polarized light showed a clear dip moving from 600 to 800 nm as the excitation angle, α, relative to the sample normal increased (see Figs. 2 and 3a). A similar feature was also found around 400 nm. With *p*-polarized excitation no clear dispersion was observed, and only a spectrum similar to the transmission of the sample was visible as shown in Fig. 3a. Control samples prepared similarly but using semiconducting (Fig. 3d) and unsorted (Supplementary material) SWCNTs did not display any dispersive features.

To test the influence of the surrounding medium on the resonances, the metallic SWCNT layers were measured within additional media. When embedding the SWCNT film in isopropanol ($n_{air} = 1.00 \rightarrow n_{IPA} = 1.38$), the dispersive resonances

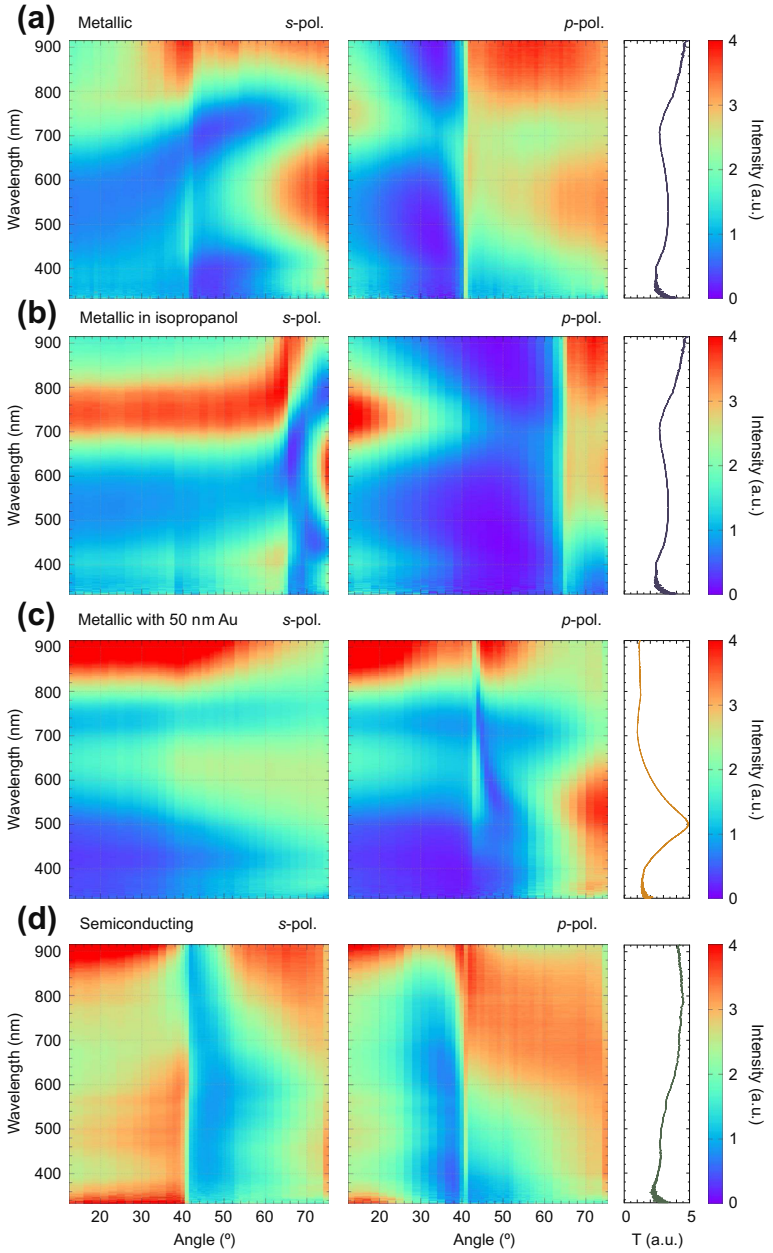

Fig. 3 – Intensity of reflected light as a function of the excitation angle and the wavelength for ~100 nm thick SWCNT networks. (a) Sample M1, which has metallic SWCNTs. The observed resonances are visible with *s*-polarization at angles above the TIR angle, ~ 41°. (b) M1 embedded in isopropanol. The resonances appear again with *s*-polarization at angles above the TIR angle, ~65°. (c) Sample M4 with metallic SWCNTs and a 50 nm Au coating on top. Typical SPP resonance is visible at *p*-polarization. (d) Sample with semiconducting SWCNTs. Transmission spectrum for each sample is also visible on the right, except for (b), where transmission was measured without isopropanol.

appeared at the same energies, but with shifted and more prominent angle dependence, as shown in Figs. 3b and 2b. Changing the surrounding medium to water yielded similar response (see Supplementary material). Instead, evaporation of 50 nm of gold on top of the SWCNT film destroyed any previous dispersive resonances: only the stagnant transmission spectrum of the SWCNTs was visible at *s*-polarization, and the characteristic surface plasmon resonance of a gold layer is seen with *p*-polarized excitation, as shown in Fig. 3c. The described resonances have also a clear dependence on the thickness of the SWCNT layer, being more pronounced near 100 nm thickness, see Fig. 4. Very thin ($\leqslant$20 nm) and thick ($\geqslant$0.5 μm) layers do not have the dispersive resonances in their reflectivity spectra as shown in Fig. 2b, where the observed dispersions of different samples and environments are collected.

In our case the resonances are observed at *s*-polarization, where the electric field of the optical excitation is parallel to the rotation axis of the Kretschmann configuration, and changing the angle does not affect its projection. On the other hand, the magnetic field of an *s*-polarized photon is perpendicular to the CNT film, and thus the angle makes a difference in terms of momentum, and could imply a dispersive behavior. One possible interpretation agreeing with the observed phenomenon is thus magnetic resonances within the network [6], excited by the magnetic field of the excitation light.

The thickness dependence of the resonances further points to a collective resonance similar to electric SPPs, which can only be excited with *p*-polarized light in thin metal films. If the metal is too thin in the case of SPPs excited via the Kretschmann configuration, the SPP will be weak because of radiation damping into the glass. As for a thick film, the SPP cannot be efficiently excited due to absorption in the metal. Similar mechanics with magnetic fields could produce the same dependence in a SWCNT film if the excitations appear at the surface [7]. These resonances could be for example magnetic plasmon resonances (MPR) formed due to coupling and regular spacing of SWCNTs within bundles. In this case the bundle acts like a lattice of nanowires with uneven endpoints [6]. Further, these resonances could enable a collective magnetization wave to propagate at the surface of the film. These magnetic plasmon polaritons (MPPs) are a likely explanation because *s*-polarized MPPs have strong dispersion whereas *p*-polarized ones are non-dispersive [8]. In addition to the above thickness dependence, this interpretation is further supported by the sensitivity to the dielectric environment, and it would also hint at a negative magnetic permeability in the material [7]. The effective dispersion also changes, because for very thin films at the M_{11} and M_{22} transition energies only regular absorption will be visible, which has no angle dependence.

Gap plasmon modes could also explain the observed phenomenon. However, these modes should depend on the length of the gap, i.e., in this case the length of the SWCNTs in bundles. To test this, a new sample was fabricated out of CNTs shortened by an extensive sonication. This resulted in a similar bundled film, but the resonances were still at the same energies; only weakened in intensity, most probably due to the additional amorphous carbon. Furthermore, LSPR in catalyst metal nanoparticles left over from the CNT synthesis would not display dispersion, and any possible combination with CNTs would have resonances dependent on the tube length. Thus, this possibility can also be ruled out.

Notable is that the dispersive resonances around 600–800 nm and 400 nm are close to the M_{11} and M_{22} transition energies of metallic SWCNTs, respectively (Figs. 2b and 3a). This raises the question whether exciton creation is causing the optical resonances. Excitons can have momentum dependence in periodic systems, but in the measured SWCNT films

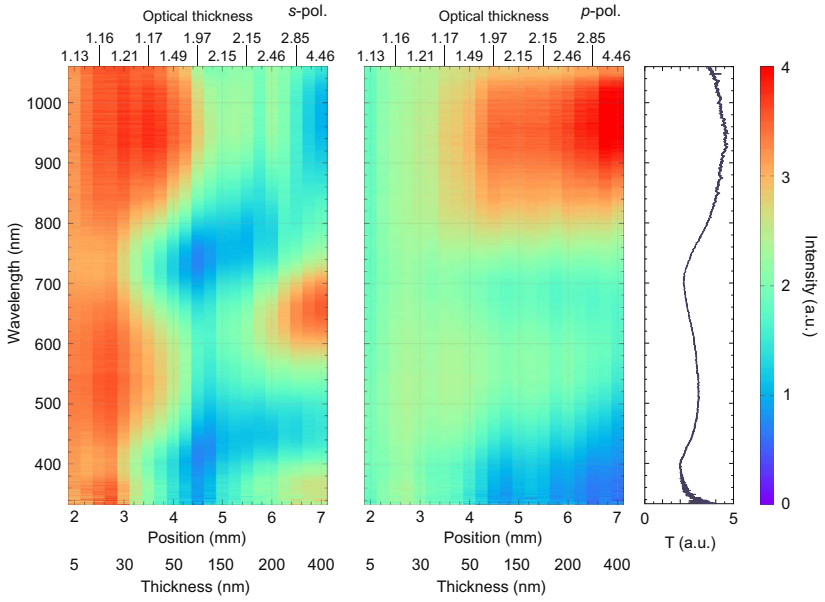

Fig. 4 – Intensity of the reflected light as a function of the network thickness and wavelength for metallic SWCNTs. Excitation angle is 51°. Optical thickness refers to transmission intensity at 900 nm wavelength divided by the intensity at 700 nm (close to the M_{11} resonance). Position refers to location on the glass sample parallel to the plane of incidence and the thickness is measured with AFM. The transmission spectrum at right is taken at the position 4.5 mm.

also the thickness affects the intensity of the resonance, which is not fully consistent with an excitonic resonance. However, an exciton–plasmon state could be responsible for the resonances in our system [9]. Graphene sandwiched between glass and polymer has also shown to pose an excess broadband absorption at s-polarization in TIR [10]. However, further experimental and theoretical studies are needed to confirm the underlying mechanism of the observed dispersive optical resonance.

In conclusion, we have observed a clearly dispersive optical resonance in reflection spectroscopy of metallic SWCNT films. It appears only for an s-polarized excitation source, and is strongest at film thicknesses around 100 nm. The dependence of intensity and dispersion of the resonance on the thickness and the surrounding environment is consistent with creation of magnetic plasmons or MPPs, and the vicinity of M_{11} and M_{22} transitions suggests that excitons may be involved in the process.

This work was supported by the Academy of Finland (Project Nos. 135193 and 218182). We thank Jaakko Koivisto for acquiring Raman spectra. T.I. thanks the Finnish National Doctoral Programme in Nanoscience.

Appendix A. Supplementary data

Supplementary data associated with this article can be found, in the online version, at http://dx.doi.org/10.1016/j.carbon.2013.07.018.

REFERENCES

[1] Wang F, Dukovic G, Brus LE, Heinz TF. The optical resonances in carbon nanotubes arise from excitons. Science 2005;308(5723):838–41.
[2] Kramberger C, Hambach R, Giorgetti C, Rümmeli MH, Knupfer M, Fink J, et al. Linear plasmon dispersion in single-wall carbon nanotubes and the collective excitation spectrum of graphene. Phys RevLett 2008;100(19):196803.
[3] Perez R, Que W. Plasmons in isolated single-walled carbon nanotubes. J Phys: Condens Matter 2006;18:3197–216.
[4] Lu Q, Rao R, Sadanadan B, Que W, Rao AM, Ke PC. Coupling of photon energy via a multiwalled carbon nanotube array. Appl Phys Lett 2005;87(17):173102.
[5] Shuba MV, Paddubskaya AG, Plyushch AO, Kuzhir PP, Slepyan GY, Maksimenko SA, et al. Experimental evidence of localized plasmon resonance in composite materials containing single-wall carbon nanotubes. Phys Rev B 2012;85(16):165435.
[6] Sarychev AK, Shvets G, Shalaev VM. Magnetic plasmon resonance. Phys Rev E 2006;73(3):036609.
[7] Ruppin R. Surface polaritons of a left-handed medium. Phys Lett A 2000;277(1):61–4.
[8] Li T, Wang S-M, Liu H, Li J-Q, Wang F-M, Zhu S-N, et al. Dispersion of magnetic plasmon polaritons in perforated trilayer metamaterials. J Appl Phys 2008;103(2):023104.
[9] Grüning M, Marini A, Gonze X. Exciton–plasmon states in nanoscale materials: breakdown of the Tamm–Dancoff approximation. Nano Lett 2009;9(8):2820–4.
[10] Ye Q, Wang J, Liu Z, Deng Z-C, Kong X-T, Xing F, et al. Polarization-dependent optical absorption of graphene under total internal reflection. Appl Phys Lett 2013;102(2):021912.

Preparation of mesoporous polyacrylonitrile and carbon fibers by electrospinning and supercritical drying

Dandan Sun [a], *Guotong Qin* [a,*], *Miao Lü* [a], *Wei Wei* [b], *Nü Wang* [a], *Lei Jiang* [a]

[a] *Key Laboratory of Bio-Inspired Smart Interfacial Science and Technology of Ministry of Education, School of Chemistry and Environment, Beihang University, 37 Xueyuan Road, Beijing 100191, China*
[b] *College of Arts and Science of Beijing Union University, 197 Beituchengxi Road, Beijing 100083, China*

ARTICLE INFO

Article history:
Received 22 March 2013
Accepted 4 July 2013
Available online 13 July 2013

ABSTRACT

Mesoporous polyacrylonitrile and carbon fibers have been prepared by electrospinning and subsequent supercritical drying and carbonization. Polyvinylpyrrolidone was used as a template. Ambient drying, oxidation, and supercritical drying were conducted to investigate the effects of treatment methods on the structure of the fibers. Interesting surface morphologies of the fibers, including nanoconvexities and nanorods, were found when the different drying methods were used. The surface area of the mesoporous carbon fibers was estimated as 602.0 $m^2 g^{-1}$, with an average pore size of 3.6 nm.

* *Corresponding author:* Fax: +86 10 82338556.
E-mail addresses: qingt@buaa.edu.cn, guotongqin@gmail.com (G. Qin).
0008-6223/$ - see front matter
http://dx.doi.org/10.1016/j.carbon.2013.07.020

A.III

Organic Electronics 25 (2015) 317–323

Contents lists available at ScienceDirect

Organic Electronics

journal homepage: www.elsevier.com/locate/orgel

Measuring optical anisotropy in poly(3,4-ethylene dioxythiophene):poly(styrene sulfonate) films with added graphene

Tommi Isoniemi [a], Sampo Tuukkanen [b,1], David C. Cameron [c,2], Janne Simonen [a], J. Jussi Toppari [a,*]

[a] University of Jyvaskyla, Department of Physics, Nanoscience Center, P.O. Box 35 (YN), FI-40014 University of Jyvaskyla, Finland
[b] Department of Electronics and Communications Engineering, Tampere University of Technology (TUT), P.O. Box 692, FI-33101 Tampere, Finland
[c] Miktech Oy, Sammonkatu 12, FI-50130 Mikkeli, Finland

ARTICLE INFO

Article history:
Received 25 March 2015
Received in revised form 22 June 2015
Accepted 24 June 2015

Keywords:
PEDOT:PSS
Graphene
Anisotropy
Spectroscopy
Conducting polymer

ABSTRACT

Graphene is a 2D nanomaterial having a great potential for applications in electronics and optoelectronics. Composites of graphene with conducting polymers have shown high performance in practical devices and their solution-processability enables low-cost and high-throughput mass manufacturing using printing techniques. Here we measure the effect of incorporation of graphene into poly(3,4-ethylene dioxythiophene):poly(styrene sulfonate) (PEDOT:PSS) to the optical anisotropy, absorbance and conductivity of the film. Uniaxial anisotropy in PEDOT:PSS films has been thought to be caused by the spin-coating process used in fabrication. We have characterized spray- and spin-coated films using ellipsometry and total internal reflection spectroscopy, the latter especially for films too thick and uneven for ellipsometry, and show that spray-coating, similar to inkjet printing, also produces consistently anisotropic properties even in very thick and uneven films. Possible plasmonic excitations related to graphene are not seen in the films. The optical and electrical anisotropy of graphene/PEDOT:PSS enables routes to high performance devices for electronics, photonics and optoelectronics.

1. Introduction

Nanostructured carbon materials, such as graphene [1,2] and carbon nanotubes (CNT) [3], have gathered vast interest due to numerous desirable properties such as high and especially tunable electrical and thermal conductivity, high tensile strength, high surface area, chemical sensitivity, flexibility, transparency and light weight. Their potential has been already proven in the fields of electronics [1,4,5], optoelectronics and optics [5–7], materials technology [8,9] as well as in energy technology and biotechnology [10]. More recently CNTs and graphene in particular have also been of interest due to their plasmonic properties [11,12].

Printing technologies offer a promising route for low-cost and high-throughput manufacturing of flexible, lightweight and even transparent electronic devices such as flexible displays, radio frequency identification (RFID) antennas, batteries, supercapacitors and solar cells [13,14]. In addition, the combination of printing technologies with disposable, non-toxic organic molecular materials offers a route towards green electronics [15]. The nanostructural carbon materials and their composites with polymers are promising solution-processable materials, e.g., for supercapacitor electrodes [16,17].

Poly(3,4-ethylene dioxythiophene) (PEDOT) is a low band-gap conjugated conducting polymer with a high charge mobility and good stability. It has a poor solubility, but when poly(styrene sulfonate) (PSS) is used as a counterion, it forms a stable dispersion that can be used to produce films with high conductivity and good transparency in the visible region. [18, p. 113] Due to these properties it has found widespread usage, particularly as a transparent electrode material and as an antistatic agent [18].

It has been shown that spin-coated PEDOT:PSS films display anisotropic properties, both optically as a uniaxial refractive index as well as in their electrical conductivity. The conductivity in the direction parallel to the film can be 500 times higher than perpendicular to the film [18, p. 133]. These anisotropic features have been explained as being caused by PSS-rich regions lying parallel to the film [19]. Electrostatic mist deposition also produces anisotropic PEDOT:PSS thin films, even before baking [20]. The choice of substrate, especially the surface roughness, has a significant effect on the structure of PEDOT:PSS thin films. Uniaxial anisotropy is

* Corresponding author.
E-mail address: j.jussi.toppari@jyu.fi (J.J. Toppari).
[1] Present address: Department of Automation Science and Engineering, Tampere University of Technology (TUT), P.O. Box 692, FI-33101 Tampere, Finland.
[2] Present address: R&D Center for Low-Cost Plasma and Nanotechnology Surface Modification, Masaryk University, Kotlářská 267/2, CZ-61137 Brno, Czech Republic.

http://dx.doi.org/10.1016/j.orgel.2015.06.037
1566-1199/

stronger when the deposition has been done on a very smooth surface such as crystalline silicon [21].

The optical anisotropy is a highly desired feature in PEDOT:PSS based optoelectronic devices such as polymer based light-emitting diodes and photovoltaic devices [22]. For instance, the photovoltaic performance of crystalline silicon/organic heterojunction solar cells was enhanced by increased anisotropy of PEDOT:PSS film [23].

Due to their enhanced electronic and optical properties, graphene and polymer/graphene composite films are promising materials for photonic and optoelectronic devices [6], for example ultra-fast lasers [24]. PEDOT:PSS/graphene has been used as low-cost counter electrode material for high performance dye-sensitized solar cells (DSSC) [25]. Very recently, large scale synthesis of PEDOT:PSS/graphene was demonstrated using in situ polymerization and the composite was used for the fabrication of thermoelectric and DSSC devices for energy harvesting applications [26].

PEDOT:PSS/graphene is a promising alternative also for conventionally used transparent and conductive coatings such as commercial indium-tin-oxide (ITO) films. Further, the solution processability of PEDOT:PSS/graphene allows for low-cost and high throughput fabrication making it interesting material for flexible and transparent optoelectronic devices such as a flexible display, solar cell and sensors. For example, printed PEDOT:PSS/graphene films have been used as stretchable [27] and transparent [28,29] electrodes.

Despite all of the above, optical properties of conductive polymers incorporating graphene have not been widely studied, even though optical characterization and analysis of these composites is a prerequisite to be able to design high performance optoelectronic devices. Here, we present analysis of optical properties of a PEDOT:PSS/graphene composite using ellipsometry and reflection measurements in total internal reflection conditions. The obtained results are compared with results from bare PEDOT:PSS films. In addition, the results of reflectance measurements are compared with the results from simulations based on experimental data from the literature.

Films that are thick, highly absorbing or uneven are not favorable for ellipsometry. However, angle-dependent spectroscopy in total internal reflection (TIR) conditions can provide a stronger and more reliable signal in these cases. TIR absorption spectroscopy is usually used to measure absorption for a very small amount of material, because the evanescent wave at the TIR interface only reaches about 100 nm beyond the interface, and the spectroscopic signal comes from this region. When used on a thin metal film in plasmonics, this setup is also referred to as the Kretschmann configuration. It thus reveals simultaneously the interference patterns as well as possible plasmonic excitations.

The setup can also be used when the TIR conditions are not completely met, and in our case we determine anisotropy from the difference of *s*- and *p*-polarization in reflectance. Measuring the reflectance with different polarizations of incoming light yields information about the anisotropy of the film due to its influence on thin-film interference [30]. This has usually been used in the case of an anisotropic film with perpendicular beam incidence, when it is known as reflection anisotropy spectroscopy [31].

2. Experimental

2.1. Solution-processable materials

Two different solution processable materials were used for the fabrication of thin films using spin- and spray-coating methods. PEDOT:PSS ink (Clevios PH500 solution purchased from H.C. Starck GmbH) is an aqueous dispersion with the PEDOT:PSS ratio of 1:2.5 by weight. The product is a blue dispersion of PEDOT:PSS containing organic solvents and polymeric binders with a solid content of 1.0–1.3 wt.%. The PEDOT:PSS ink viscosity is 8–25 mPas.

PEDOT:PSS/graphene ink (Phene + I3015 transparent inkjet conductive ink purchased from Innophene Co., Ltd.) is an aqueous dispersion containing 15 wt.% PEDOT:PSS polymer, 15 wt.% graphene, 5–10 wt.% diethylene glycol and 1–5 wt.% ethanol. The PEDOT:PSS/graphene ink has a solid content of 0.6 wt.%, its viscosity is 7.2 mPas and the conductivity is given as 300 S/cm. The graphene flakes are homogeneously dispersed in the polymer matrix [27]. For some PEDOT:PSS/graphene samples ultrasonication (Elma S120H Elmasonic 1000 W, 90 min) was used on the ink before applying it on the substrate. This was done to check for any possible effects resulting from breaking down the graphene flakes within the ink.

2.2. Preparation of films

The PEDOT:PSS and PEDOT:PSS/graphene films were produced with a spray-coating process. Glass substrates (Präzisions Glas & Optik Selected White Float glass, $20 \times 20 \times 1.25$ mm, $n = 1.52$) were cleaned with acetone and isopropanol. The spray-coating was done using a Silverline airbrush perpendicularly on the substrate at a distance of 10 cm operated with standard compressed (1 bar) air. The substrate was on a hot-plate at 115 °C, and the spray-coating was done slowly to avoid the formation of any visible droplets. For comparison, some samples were instead spin-coated at 2000 or 6000 rpm. Deposited PEDOT:PSS films were baked in an oven at 100 °C for 6 min and PEDOT:PSS/graphene films at 120 °C for 10 min. The samples were stored in ambient conditions.

2.3. Characterization of the films

The sheet resistances of the thin films were obtained with a four-point probe measurement setup. The probe included four electrodes with mercury contacts in a line with probe separation of 2.5 mm. A Keithley 2456 Sourcemeter was used to drive a constant current of 0.1 mA (except 1 μA for samples with square resistances over 100 kΩ) to the outer electrodes and to measure the voltage at the inner electrodes. Five measurements were averaged for each sample, using the standard error of the mean, and the sheet resistances were calculated depending on the dimensions of the samples [28].

Thickness and topography of the films were characterized using a Veeco Dimension 3100 atomic force microscope (AFM). Scanning electron microscopy (SEM) was done on cut surfaces of the polymer films on a silicon substrate with a Raith e-Line 50 system.

The optical reflection measurements were performed in a TIR configuration depicted in Fig. 1. Measured incidence angles ranged from 13° to 74°, extending across the TIR angle of 41° for a simple glass-air interface. The glass slides with polymer layers on top were mounted on a flat face of a hemicylindrical prism with index matching oil (Zeiss Immersol 518F, $n = 1.518$). The angle of the collimated excitation light (220 W Oriel tungsten-halogen lamp) was tuned with a goniometric prism mount, and the reflected light was collected to an optical fiber and fed to a spectrometer (Jobin Yvon iHR320) equipped with a CCD camera (Jobin Yvon Symphony CCD-1024X256-OPEN-STE).

Absorbance measurements were done with a PerkinElmer Lambda 850 UV/VIS Spectrometer. The transmission data were normalized in respect to the empty glass substrate, and the absorbance is presented as the average absorption at wavelength range 400–700 nm.

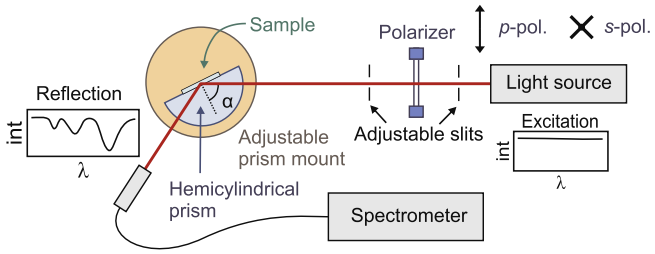

Fig. 1. Schematics of the total internal reflection setup and geometry used in the experiment.

Variable-angle spectroscopic ellipsometry (VASE) measurements were done with a J.A. Woollam M-2000UI ellipsometer. As the measured films were on glass substrates, the second glass interface was covered with black paint to eliminate reflections from it.

3. Results and discussion

3.1. Film morphology and conductivity

Details of the fabricated samples, including sample names/codes (starting with 'A' for PEDOT:PSS films, 'B' for PEDOT:PSS/graphene films and 'C' for PEDOT:PSS/graphene films with presonication), film thickness d, root mean square roughness r_q in a 1 μm × 1 μm area and sheet resistance R_S, are presented in Table S1 in Supplementary material. The spray-coated films are typically about ten times thicker than spin-coated films (340–2100 nm versus 29–77 nm).

AFM images of typical spray- and spin-coated films are presented in Fig. 2a–d. It can be noticed that the PEDOT:PSS/graphene films have typically higher roughness than bare PEDOT:PSS films, which is particularly noticeable in spin-coated films. This can result from the presence of graphene flakes which

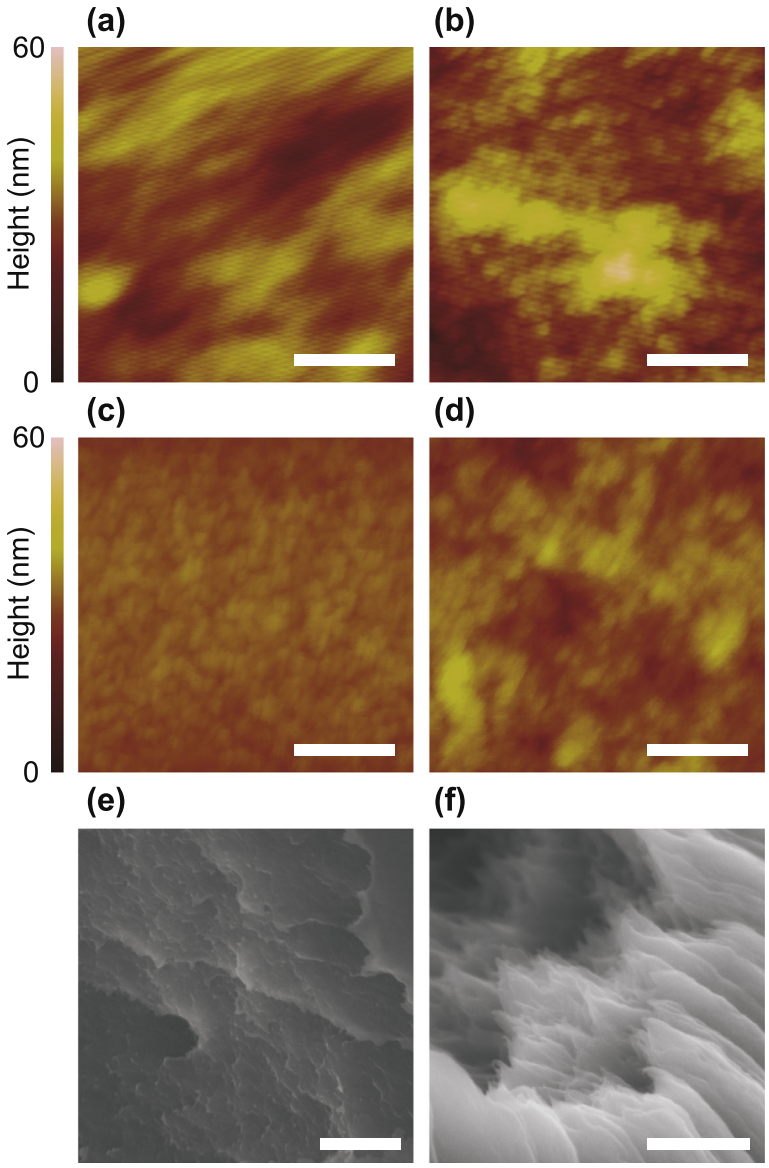

Fig. 2. AFM micrographs of flat surfaces of spray-coated films of (a) 2100 ± 100 nm thick PEDOT:PSS, root mean square roughness for the image area r_q = 4.5 nm (A-9) and (b) 2150 ± 150 nm thick PEDOT:PSS/graphene, r_q = 5.7 nm (B-9), and corresponding spin-coated films of (c) 29 ± 1 nm thick PEDOT:PSS, r_q = 0.96 nm (A-S1), (d) 34 ± 5 nm thick PEDOT:PSS/graphene, r_q = 3.1 nm (B-S1). SEM micrographs at 5 kV acceleration voltage of cut surfaces of (e) PEDOT:PSS and (f) PEDOT:PSS/graphene. All scale bars are 300 nm.

could prevent relaxation of the ink surface during the deposition process.

Spray-coated samples expectedly have a much higher roughness than the spin-coated ones, especially when considering large areas. Because film thickness measurements were done with AFM on one 10 μm long cut interface for each film, and the uncertainty is estimated from this measurement, the thickness values for a whole spray-coated sample may have even higher variations than those presented.

SEM images of cut edges of droplet-deposited polymers are presented in Fig. 2e and f. The presence of flakes can be observed in the PEDOT:PSS/graphene film. However, some layered edge formation also appears in the bare PEDOT:PSS film.

The addition of graphene into the PEDOT:PSS film had a clear effect on the properties of the film. The most remarkable effect was observed in the conductivity. For instance, a 550 nm thick PEDOT:PSS/graphene film has a sheet resistance of 61 ± 12 Ω/sq, which is less than 1% of the sheet resistance of a similar bare PEDOT:PSS film, i.e., 10.8 ± 1.2 kΩ/sq (see Table S1 and Fig. S1 in Supplementary material). Spray-coated bare PEDOT:PSS had a conductivity at 0.8 ± 0.3 S/cm, while PEDOT:PSS/graphene had a conductivity of 310 ± 40 S/cm. PEDOT:PSS/graphene with 90 min of sonication had an unchanged conductivity of 320 ± 60 S/cm. The conductivities were determined by linear fits for films of different thicknesses (Fig. S3 in Supplementary material). As expected, there is a linear dependence between increasing film thickness and increasing conductivity in the deposited films. However, in spray-coated PEDOT:PSS, this linear dependence is not very clear. Thin spin-coated samples have lower conductivities, 0.104 ± 0.013 S/cm for PEDOT:PSS (29 and 77 nm thick films) and 130 ± 30 S/cm for unsonicated PEDOT:PSS/graphene (34 nm thick film).

3.2. Absorption measurements

It can be noticed that the optical absorption increases linearly with the thickness of the film and decreases as a function of sheet resistance (see Figs. S2 and S4 in Supplementary material). The absorbance used here is defined in Section 2.3. (roughly comparable to absorbance at 550 nm) and representative transmittance spectra are shown in Fig. S8 of the Supplementary material. Fitting a linear dependency on absorption as a function of thickness one obtains an absorption per film thickness of 0.46 ± 0.05 1/μm for spray-coated PEDOT:PSS, while PEDOT:PSS/graphene had a clearly lower value at 0.27 ± 0.03 1/μm. Sonicating PEDOT:PSS/graphene for 90 min had no clear effect on this, producing films with 0.28 ± 0.05 1/μm absorption. For spin-coated samples the absorption values were somewhat lower, 0.38 ± 0.03 1/μm for two PEDOT:PSS samples and 0.14 ± 0.03 1/μm for one (not sonicated) PEDOT:PSS/graphene sample.

The optical absorbance in a similar PEDOT:PSS/graphene ink has been shown to have a linear relationship with graphene content [32]. In light of this, the measured higher absorbance of plain PEDOT:PSS is surprising, but the compositions of our measured inks are not directly comparable.

3.3. Reflection measurements

Results from the reflection measurements are shown in Fig. 3 for some of the samples (more data in Supplementary material in Figs. S5–S7). Clear interference patterns are visible in all of the samples, and with both polarizations. The anisotropic optical properties of the films are clearly visible as different positions and depths of the destructive interference resonances at *s*- and

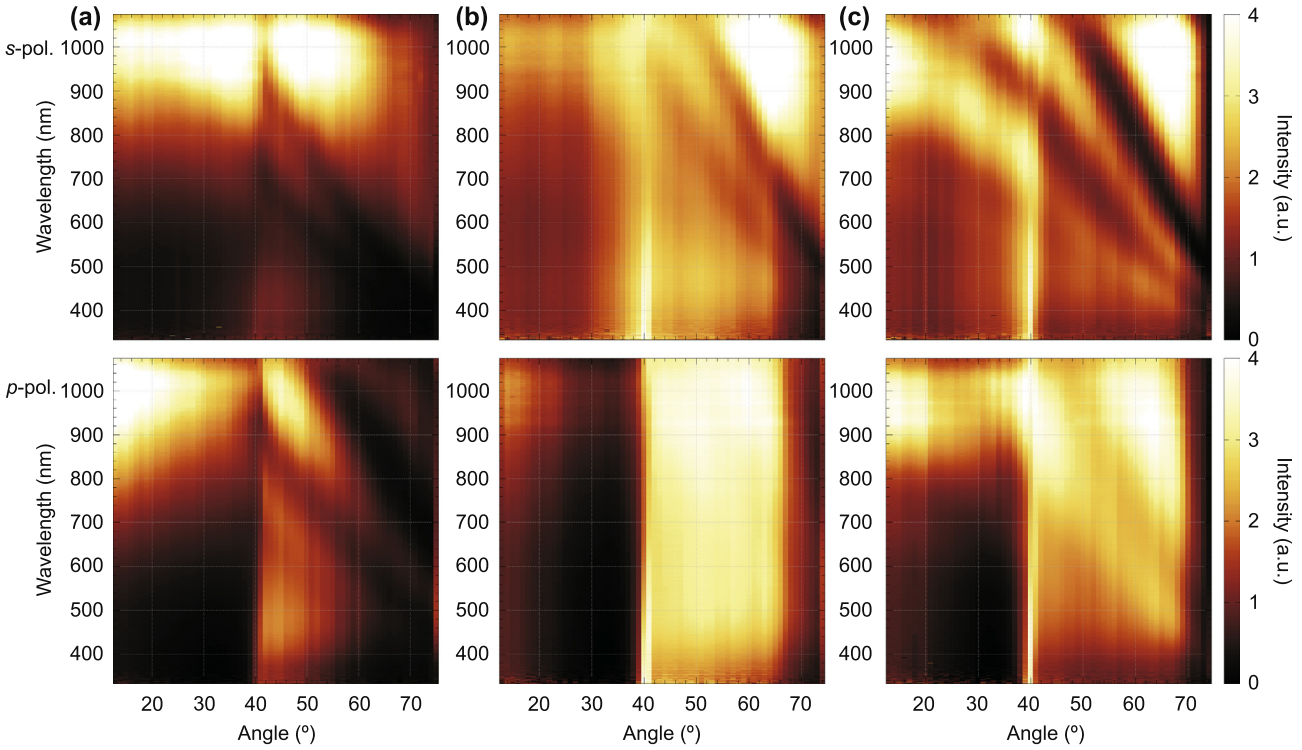

Fig. 3. Reflection spectra for spray-coated films measured in total internal reflection conditions. (a) PEDOT:PSS, 500 nm thick (A-3), (b) PEDOT:PSS/graphene, 550 nm thick (B-4), (c) PEDOT:PSS/graphene, 560 nm thick, sonicated 90 min to reduce flake size (C-1). Upper row s-polarization and lower row p-polarization. Intensity of spectra below 41° angles are not to scale.

p-polarizations. In addition, inclusion of graphene enhances the resonances and anisotropy between the polarizations, and sonication does so even further, as more clearly visible in Figs. S5–S7. However, in case of the sonication, stronger interference resonances are most likely due to smoother film surfaces.

Collective optical excitations with angle-dependent resonances that cannot be explained by interference were found on thin films of single-walled metallic carbon nanotubes [12], but not seen in PEDOT:PSS or PEDOT:PSS/graphene films. The lack of this kind of plasmonic behavior, which might suppress optical signals, increases their viability for optoelectronics applications. The optical excitation in TIR conditions can easily reach through a μm-scale PEDOT:PSS/graphene film, as can be seen in Fig. S7f of the Supplementary material. In this case, surface plasmon polaritons (SPP) were excited on a 50 nm gold film through a 1280 nm thick PEDOT:PSS/graphene layer, which can be seen in the observed SPP dispersion.

3.4. Ellipsometer measurements

For spray-coated samples, the ellipsometric model used to fit the VASE data utilized uniaxial anisotropy with the perpendicular and parallel components using multiple Lorenz functions [33]. In cases where different thicknesses of the same material were measured, a coupled model has been used. The ellipsometry fits of the spin-coated samples were done with a model that allowed *n* and *k* values to vary independently. Fig. 4 shows the fitted real parts *n* and imaginary parts *k* of the refractive index in both horizontal and vertical directions for the PEDOT:PSS and PEDOT:PSS/graphene samples. The results show clear anisotropy in all the cases, but the effect of graphene is only minor. Note: the displayed curves have been smoothed using a cubic function to remove random noise in the calculated data.

The fitted functions of the refractive indices reveal that PEDOT:PSS films that include graphene have a slightly different optical response (Fig. 4a and b), but the difference is not significant based on ellipsometry measurements. Spray coating, like spin coating, also produces highly anisotropic films, contrary to earlier assumptions [22]. Even though ellipsometry is not very reliable in the case of a thick and rough spray-coated sample, anisotropy in the films is clearly visible here (Fig. 4c, Fig. S9 in Supplementary material).

For very thin (spin-coated) samples the mean square error (MSE) of the ellipsometry fits is 1.7 (Fig. 4a) and 1.4 (Fig. 4b), which is a good fit. For thick (spray-coated) samples the MSE is higher, of the order 20. In both cases the general shape and trend of the resulting material parameters are reasonably stable.

3.5. Simulations

To compare ellipsometric measurements with reflectometry, the reflection spectra were simulated using Comsol Multiphysics 5.0, a commercial implementation of the finite-element method. The developed model calculates the reflectance of an infinite plane wave incident on the air/film/glass interface. The model was reduced to a 2D geometry to speed up the calculation.

The simulation domain was 0.1 μm by 6.5 μm and contained 644 mesh elements. 12 h of calculation time was used to generate the data in Fig. 5 on a cluster using 48 Intel Xeon X5650 processors. The resolution of the images in Fig. 5 is 201 × 131 points (wavelength and angle, respectively). The anisotropic refractive indices needed for the simulations were obtained from spectroscopic ellipsometry measurements.

The results were verified in the case of *s*-polarized light by comparing them to isotropic simulations performed with the transfer matrix method that we implemented with Matlab. This is possible because the *s*-polarized incident light only experiences the refractive index component parallel to the film.

Uniaxial anisotropy can be seen as shifting of the thin-film interference fringes. At *p*-polarization the effective refractive index is higher because the perpendicular direction component of the refractive index affects this polarization. This results in the decrease of distance between the fringes at a certain incidence angle compared to *s*-polarization, and the movement of specific maxima and minima to longer wavelengths [30]. The change in refractive index as a function of wavelength can be seen in the curvature of the interference fringes.

For spray-coated samples the simulations (Fig. 5) match measurements (Fig. 3) reasonably well in terms of locations of the

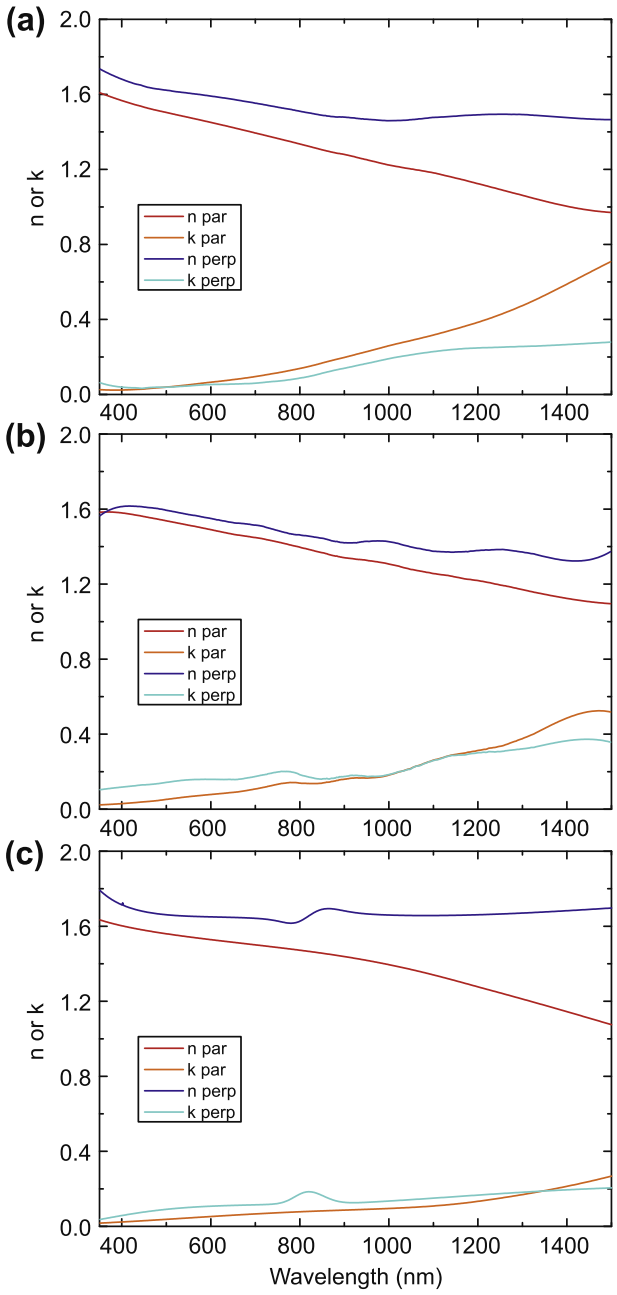

Fig. 4. Refractive indices *n* and extinction coefficients *k* for both parallel and perpendicular directions of thin films acquired from ellipsometry fits. (a) Spin-coated PEDOT:PSS (combined result from samples A-S1 and A-S2). (b) Spin-coated PEDOT:PSS/graphene (only B-S1). (c) Spray-coated PEDOT:PSS/graphene, sonicated for 90 min (combined result from six samples, C-1 to C-6).

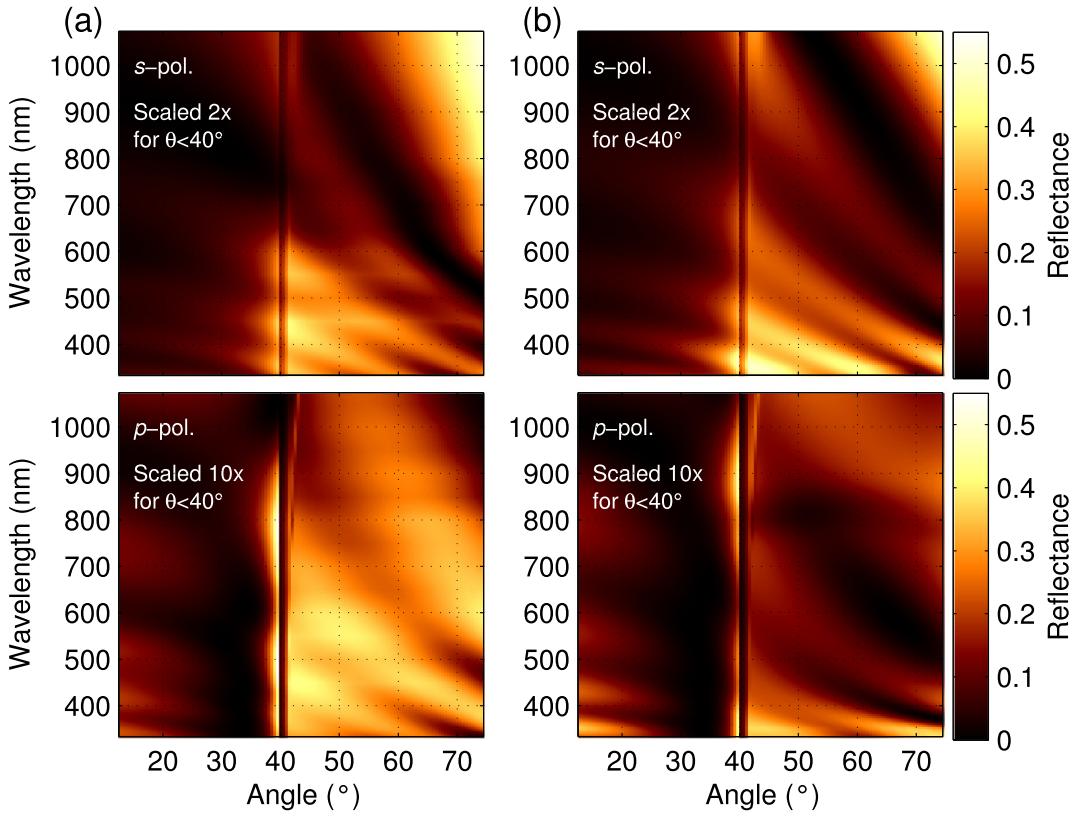

Fig. 5. Reflection spectra in total internal reflection conditions, simulated from ellipsometry data. (a) PEDOT:PSS, 500 nm thick, refractive index from spin-coated samples [22]. (b) 560 nm thick PEDOT:PSS/graphene, uses data from Fig. 4c.

interference resonances. Inconsistencies are mostly due to the roughness and relatively high absorbance of the thin films, which produce difficulties in getting reliable ellipsometry data. This reveals the power of reflective measurements in this case.

4. Conclusions

Using variable-angle total internal reflection spectroscopy, we have found that spray-coated films of PEDOT:PSS on glass have a high degree of optical anisotropy at longer wavelengths in the infrared region. For spin-coated thin PEDOT:PSS films the anisotropic structure has been previously thought to have been caused by the spin-coating process, which would align the PSS-rich regions of high conductivity along the film plane [22]. Our measurements show that an alternative mechanism produces anisotropy in spray-coated films of all measured thicknesses. Previous anisotropy measurements with ellipsometry have only been done on sub-200 nm films, while our TIR measurements show clear anisotropic features in interference up to thickness of 2.5 μm. The addition of graphene to PEDOT:PSS greatly increases the conductivity of the films, but the optical anisotropy shows only minor enhancement on the thick films. The refractive index functions do not show significant differences between measured inks with and without graphene. TIR absorbance measurements show a clear advantage over ellipsometry in assessing thin film anisotropy in cases where the film is thick or uneven. Optically and electrically anisotropic graphene/PEDOT:PSS films have a wide range of applications in electronics, photonics and optoelectronics.

Acknowledgments

Funding from the Academy of Finland is gratefully acknowledged (Projects 135193, 218182, 263868, 263526, 283011, 138146). We thank Niko-Ville Hakkola for help in the reflection measurements. T.I. thanks the Finnish National Doctoral Programme in Nanoscience and the Vilho, Yrjö and Kalle Väisälä Fund of the Finnish Academy of Sciences and Letters for financial support.

Appendix A. Supplementary data

Supplementary data associated with this article can be found, in the online version, at http://dx.doi.org/10.1016/j.orgel.2015.06.037.

References

[1] A.K. Geim, K.S. Novoselov, The rise of graphene, Nat. Mater. 6 (2007) 183–191.
[2] K.S. Novoselov, V.I. Fal, L. Colombo, P.R. Gellert, M.G. Schwab, K. Kim, et al., A roadmap for graphene, Nature 490 (2012) 192–200.
[3] J. Robertson, Growth of nanotubes for electronics, Mater. Today 10 (2007) 36–43.
[4] S. Park, M. Vosguerichian, Z. Bao, A review of fabrication and applications of carbon nanotube film-based flexible electronics, Nanoscale 5 (2013) 1727–1752.
[5] P. Avouris, Z. Chen, V. Perebeinos, Carbon-based electronics, Nat. Nanotechnol. 2 (2007) 605–615.
[6] F. Bonaccorso, Z. Sun, T. Hasan, A.C. Ferrari, Graphene photonics and optoelectronics, Nat. Photonics 4 (2010) 611–622.
[7] P. Avouris, M. Freitag, V. Perebeinos, Carbon-nanotube photonics and optoelectronics, Nat. Photonics 2 (2008) 341–350.
[8] D.R. Paul, L.M. Robeson, Polymer nanotechnology: nanocomposites, Polymer 49 (2008) 3187–3204.
[9] C. Lee, X. Wei, J.W. Kysar, J. Hone, Measurement of the elastic properties and intrinsic strength of monolayer graphene, Science 321 (2008) 385–388.
[10] M.F.L. De Volder, S.H. Tawfick, R.H. Baughman, A.J. Hart, Carbon nanotubes: present and future commercial applications, Science 339 (2013) 535–539.
[11] A.N. Grigorenko, M. Polini, K.S. Novoselov, Graphene plasmonics, Nat. Photonics 6 (2012) 749–758.
[12] T. Isoniemi, A. Johansson, J.J. Toppari, H. Kunttu, Collective optical resonances in networks of metallic carbon nanotubes, Carbon 63 (2013) 581–585.

[13] S.R. Forrest, The path to ubiquitous and low-cost organic electronic appliances on plastic, Nature 428 (2004) 911–918.
[14] K. Hecker, S. Breitung, OE-A Roadmap for Organic and Printed Electronics: White Paper, fifth ed., Organic Electronics Association (OE-A), VDMA Verlag GmbH, 2013.
[15] Towards Green Electronics in Europe, The Strategic Research Agenda (SRA) for the Organic and Large Area Electronics (OLAE), Published on the OPERA website on September 18, 2009.
[16] H.-J. Choi, S.-M. Jung, J.-M. Seo, D.W. Chang, L. Dai, J.-B. Baek, Graphene for energy conversion and storage in fuel cells and supercapacitors, Nano Energy 1 (2012) 534–551.
[17] S. Lehtimäki, S. Tuukkanen, J. Pörhönen, P. Moilanen, J. Virtanen, M. Honkanen, D. Lupo, Low-cost, solution processable carbon nanotube supercapacitors and their characterization, Appl. Phys. A 117 (2014) 1329–1334.
[18] A. Elschner, S. Kirchmeyer, W. Lovenich, U. Merker, K. Reuter, PEDOT: Principles and Applications of an Intrinsically Conductive Polymer, CRC Press, 2010.
[19] S. Timpanaro, M. Kemerink, F.J. Touwslager, M.M. De Kok, S. Schrader, Morphology and conductivity of PEDOT/PSS films studied by scanning–tunneling microscopy, Chem. Phys. Lett. 394 (2004) 339–343.
[20] T. Hiate, N. Miyauchi, Q. Liu, R. Ishikawa, K. Ueno, H. Shirai, Real-time measurement of optical anisotropy during film growth using a chemical mist deposition of poly(3,4-ethylenedioxythiophene):poly(styrenesulfonate), J. Appl. Phys. 115 (2014) 123514.
[21] T. Ino, T. Hiate, T. Fukuda, K. Ueno, H. Shirai, Real-time ellipsometric characterization of the initial growth stage of poly(3,4-ethylenedioxythiophene): poly(styrene sulfonate) films by electrospray deposition using n,n-dimethylformamide solvent solution, J. Non-Cryst. Solids 358 (2012) 2520–2524.
[22] L.A.A. Pettersson, S. Ghosh, O. Inganäs, Optical anisotropy in thin films of poly(3,4-ethylenedioxythiophene)–poly(4-styrenesulfonate), Org. Electron. 3 (2002) 143–148.
[23] Q. Liu, T. Imamura, T. Hiate, I. Khatri, Z. Tang, R. Ishikawa, K. Ueno, H. Shirai, Optical anisotropy in solvent-modified poly(3,4-ethylenedioxythiophene): poly(styrenesulfonic acid) and its effect on the photovoltaic performance of crystalline silicon/organic heterojunction solar cells, Appl. Phys. Lett. 102 (2013) 243902.
[24] Z. Sun, T. Hasan, F. Torrisi, D. Popa, G. Privitera, F. Wang, F. Bonaccorso, D.M. Basko, A.C. Ferrari, Graphene mode-locked ultrafast laser, ACS Nano 4 (2010) 803–810.
[25] W. Hong, Y. Xu, G. Lu, C. Li, G. Shi, Transparent graphene/PEDOT–PSS composite films as counter electrodes of dye-sensitized solar cells, Electrochem. Commun. 10 (2008) 1555–1558.
[26] D. Yoo, J. Kim, J.H. Kim, Direct synthesis of highly conductive poly(3,4-ethylenedioxythiophene):poly(4-styrenesulfonate)(PEDOT:PSS)/graphene composites and their applications in energy harvesting systems, Nano Res. 7 (2014) 717–730.
[27] S. Tuukkanen, M. Hoikkanen, M. Poikelispää, M. Honkanen, T. Vuorinen, M. Kakkonen, J. Vuorinen, D. Lupo, Stretching of solution processed carbon nanotube and graphene nanocomposite films on rubber substrates, Synth. Met. 191 (2014) 28–35.
[28] S. Tuukkanen, T. Julin, V. Rantanen, M. Zakrzewski, P. Moilanen, K.E. Lilja, S. Rajala, Solution-processible electrode materials for a heat-sensitive piezoelectric thin-film sensor, Synth. Met. 162 (2012) 1987–1995.
[29] T. Vuorinen, M. Zakrzewski, S. Rajala, D. Lupo, J. Vanhala, K. Palovuori, S. Tuukkanen, Printable, transparent, and flexible touch panels working in sunlight and moist environments, Adv. Funct. Mater. 24 (2014) 6340–6347.
[30] G.I. Surdutovich, J. Kolenda, J.F. Fragalli, L. Misoguti, R. Vitlina, V. Baranauskas, An interference method for the determination of thin film anisotropy, Thin Solid Films 279 (1996) 119–123.
[31] P. Weightman, D.S. Martin, R.J. Cole, T. Farrell, Reflection anisotropy spectroscopy, Rep. Prog. Phys. 68 (2005) 1251.
[32] Y. Xu, Y. Wang, J. Liang, Y. Huang, Y. Ma, X. Wan, Y. Chen, A hybrid material of graphene and poly(3,4-ethyldioxythiophene) with high conductivity, flexibility, and transparency, Nano Res. 2 (2009) 343–348.
[33] L.A.A. Pettersson, F. Carlsson, O. Inganäs, H. Arwin, Spectroscopic ellipsometry studies of the optical properties of doped poly(3,4-ethylenedioxythiophene): an anisotropic metal, Thin Solid Films 313 (1998) 356–361.